UNIVERSITY OF CALIFORNIA
Los Angeles

Multiscale and Patient-Specific Cardiovascular Modeling

A dissertation submitted in partial satisfaction
of the requirements for the degree
Doctor of Philosophy in Mechanical Engineering

by

Daniel Canuto

2019

ABSTRACT OF THE DISSERTATION

Multiscale and Patient-Specific Cardiovascular Modeling

by

Daniel Canuto
Doctor of Philosophy in Mechanical Engineering
University of California, Los Angeles, 2019
Professor Jeffrey D. Eldredge, Chair

Despite continuing advances in computational power, full-body models of the human cardiovascular system remain a costly task. Two principal reasons for this cost are the total overall length of the vascular network (spanning $\mathcal{O}(10^8)$ m) and the broad range of length scales (from 10^{-2} to 10^{-6} m) involved. Multiscale modeling can be employed to overcome these issues; specifically, subsystems of higher spatial dimension representing domains of interest can be coupled at their boundaries to lower-dimensional subsystems that mimic relevant inflow/outflow conditions. Though this scheme can increase computational efficiency, the inherent reduction in spatial dimension results in parameterizations that can be difficult to optimize in patient-specific contexts. This work is divided into two parts: in the first segment, a closed-loop multiscale model of the entire cardiovascular system is developed and integrated with a feedback control model for blood pressure regulation. It is tested against clinical data for cohorts of healthy subjects, and its predictive utility is demonstrated in a simulation of acute hemorrhage from the upper leg. After validating the multiscale/reduced-order approach, a parameter optimization technique based on the ensemble Kalman filter (EnKF) is constructed. By assimilating patients' clinical measurements, this method is shown to successfully tune parameters in two models: a zero-dimensional model of the pulmonary circulation, and a multiscale 0D-1D model of the lower leg.

The dissertation of Daniel Canuto is approved.

Kunihiko Taira

Xiaolin Zhong

Joseph M. Teran

Jeffrey D. Eldredge, Committee Chair

University of California, Los Angeles

2019

TABLE OF CONTENTS

LIST OF FIGURES

LIST OF TABLES

ACKNOWLEDGMENTS

I'm pretty exhausted, so I'm sure this list won't be exhaustive, but here goes. To Mom, for always telling me I would do great things. To Dad, for exhorting me to be a leader, not a follower. To Stephen, for being my jelly preserver since the day I was born. To Julie, for telling me that I'm amazing on days when I feel quite the opposite. To all my friends back east, for keeping me humble and sane. To Sam, for introducing a bewildered undergrad to the weird, wonderful world of research. And finally, to Jeff, for asking the right questions and nudging me in the right directions. This work would never have been possible without y'all's advice and encouragement, and I am deeply grateful.

CHAPTER 1

Introduction

1.1 Background

In terms of its fluid dynamics, the human cardiovascular system is immensely complex. The flow is pulsatile, transitions between laminar and turbulent [Ku97], involves fluid-structure interactions [TOK06], and has characteristic length scales spanning several orders of magnitude [TD09]. The relevant anatomy is no simpler: the heart is a four-chambered, electrochemical pump [TD09], delivering blood to a network of vessels whose total length is $\mathcal{O}(10^8)$ meters [LE04]. Moreover, both the heart and the vasculature can be regulated by local [LCG03] and global [Kor71] control, incorporating sensors for pressure [Dan98], blood volume [AHM76], lung inflation [AT84], and chemical concentration [Dam94]. As such, a complete description of the cardiovascular system is well beyond the scope of the present work. Instead, this chapter outlines only the anatomical and physiological features whose modeling is attempted, followed by a brief history of relevant modeling work from the literature. With this context in mind, the chapter closes with the objectives of this work.

1.1.1 The cardiovascular system

1.1.1.1 Heart

The heart is the cornerstone of the cardiovascular system, its contractions creating the pressure difference required to transport blood through the body. Fig. 1.1 shows a cross-sectional schematic of the heart and its major connections [Pie06]. The ventricles' primary function is to send blood from the heart: the right ventricle pumps deoxygenated blood

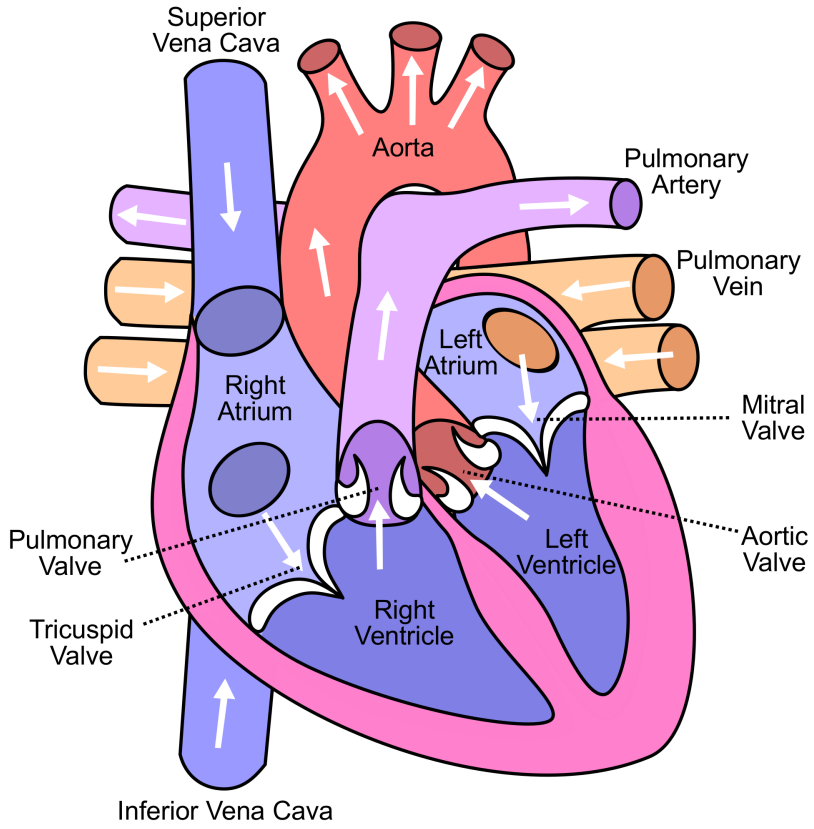

Figure 1.1: Cross-sectional schematic of the human heart [Pie06].

towards the lungs through the pulmonary artery (the pulmonary circulation), while the left ventricle pumps oxygenated blood to the remainder of the body through the aorta (the systemic circulation). By contrast, the atria are the reception sites for incoming blood: the right atrium receives deoxygenated blood from the systemic circulation, whereas the left atrium receives oxygenated blood from the pulmonary circulation.

Outward flow from the left and right ventricles is mediated by valves (the aortic and pulmonary valves, respectively), as is flow from the atria to the ventricles (through the mitral and tricuspid valves). These valves have a leaflet shape that permits opening only under a pressure difference that produces flow in the antegrade direction, as indicated by the arrows in Fig. 1.1. Furthermore, flow across the valves is subject to several important phenomena, including non-instantaneous valve motion (i.e., flow through a variable area), fluid inertia, and the development of vortical structures [Goh07, MDP12].

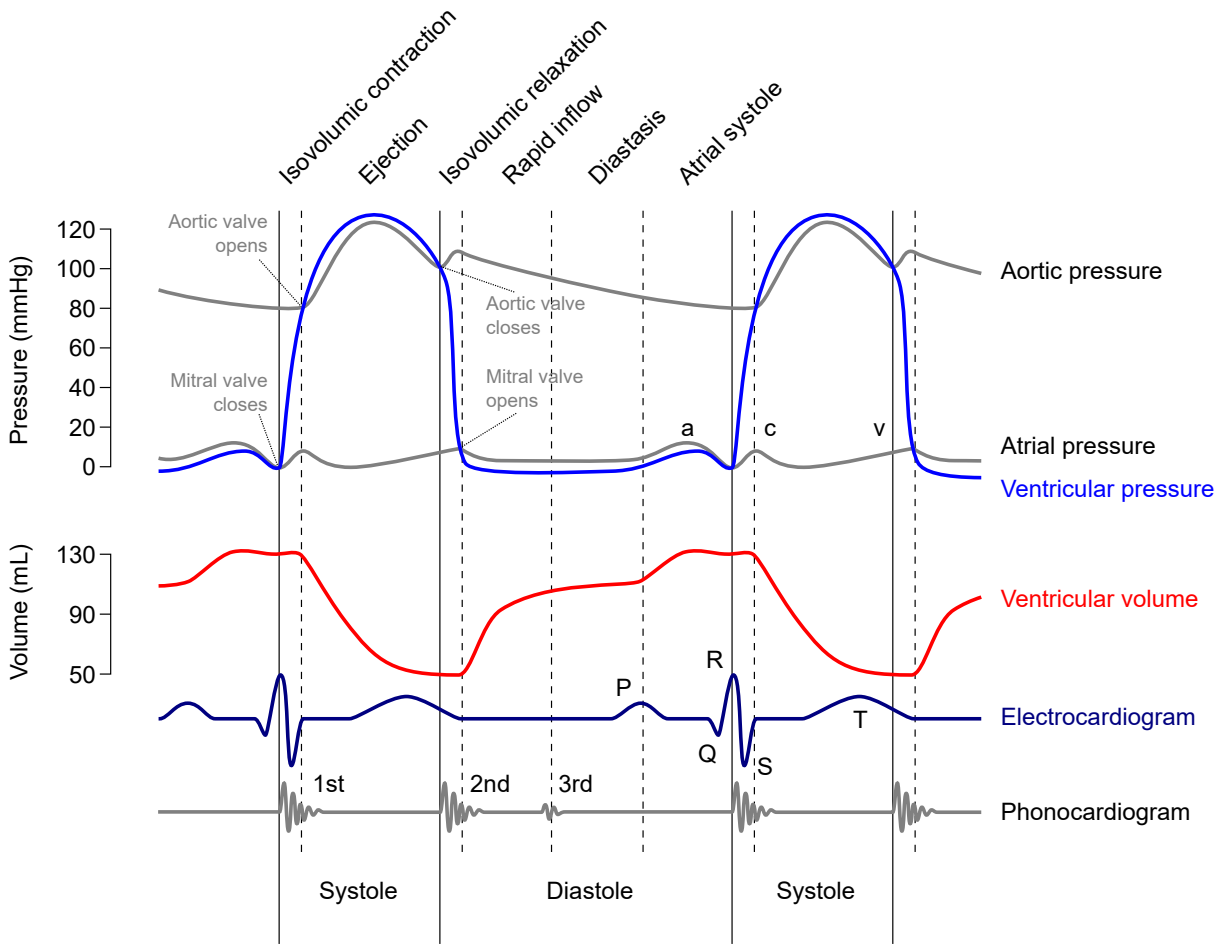

Figure 1.2: A Wiggers diagram, illustrating the phases of the cardiac cycle for the left heart (reproduced from Wikimedia Commons under the GNU Free Documentation License).

The opening and closing of the cardiac valves, and hence the flow of blood through the body, happens as a consequence of the rhythmic contraction and relaxation of the heart's muscular tissue (the *myocardium*). This process is the cardiac cycle, and is commonly visualized by a collection of plots known as the "Wiggers diagram," as reproduced in Fig. 1.2. Referring to the diagram, the first portion of the cycle is called systole, and is characterized by flow from the ventricles into the vasculature. In early systole, the ventricular myocardium recieves an electrical signal and depolarizes (the so-called "QRS complex" labeled on the electrocardiogram), causing a muscular contraction that rapidly raises the pressure of the blood within the ventricle. Once ventricular pressure exceeds aortic pressure, the aortic valve opens, allowing blood to eject into the aorta and be distributed through the systemic circulation.

As the ventricle empties and relaxes, its internal pressure falls, eventually dropping below aortic pressure and leading to the closure of the aortic valve. At the same time, the ventricle electrically repolarizes to prepare for the next cycle, as shown by the "T wave" on the electrocardiogram. As this repolarization ends, the heart begins its diastolic phase, in whcih the ventricles are refilled for the next cycle. This phase begins with a short period of ventricular relaxation at constant volume, as both the aortic and mitral valves are closed. Upon complete ventricular relaxation, atrial pressure exceeds ventricular pressure, leading to the opening of the mitral valve and an initially rapid refilling of the ventricle. However, as the ventricle fills, its pressure rises, leading to a reduction in its filling rate known as diastasis. To achieve complete refilling, the atrium depolarizes and contracts, resulting in the "P wave" on the electrocardiogram, the return of the ventricle to its initial volume, and the completion of the cycle. As a closing remark, note that despite this discussion's focus on the left heart, the right heart undergoes a qualitatively identical cycle at a lower pressure: normal mean pulmonary artery pressure is less than 20 mmHg in healthy adults [DMG87], whereas a typical value for mean aortic pressure is 83 mmHg [TD09].

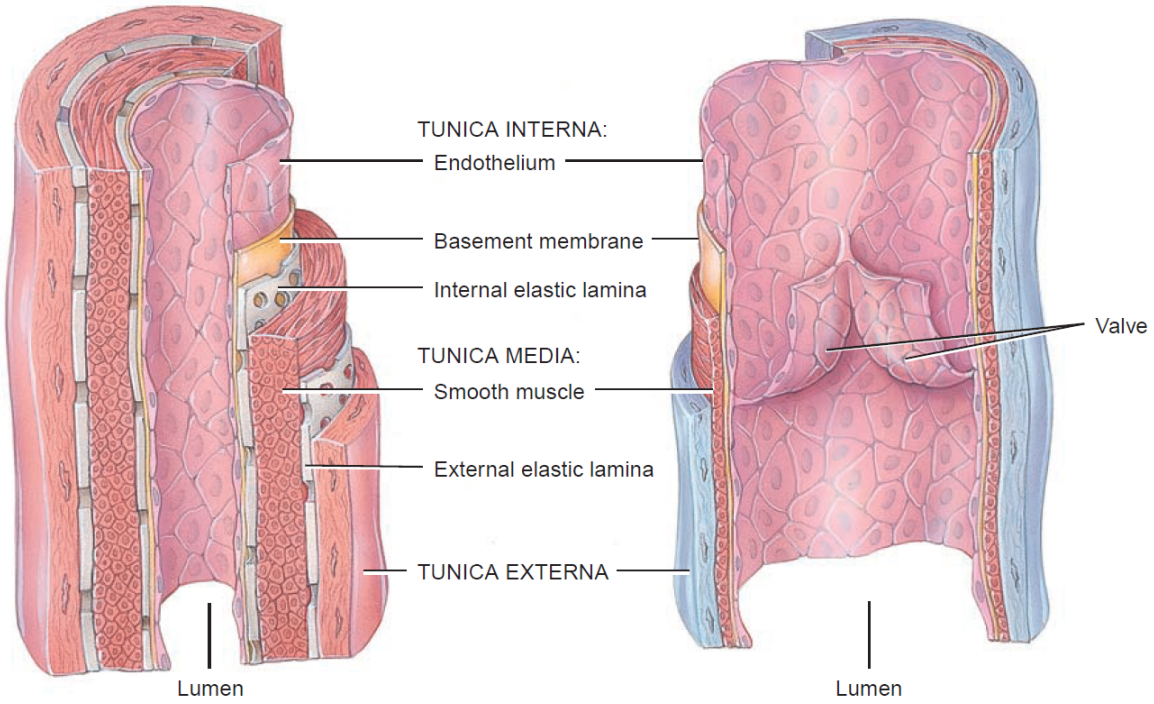

(a) Artery (b) Vein

Figure 1.3: Comparison of blood vessel structure for (a) arteries and (b) veins [TD09].

1.1.1.2 Blood vessels

Blood vessels are the transport network of the cardiovascular system, and can be roughly divided into five parts: arteries, arterioles, capillaries, venules, and veins. Arteries carry blood away from the heart, gradually branching and narrowing into arterioles as they approach target organs. The arterioles then branch into capillaries, whose thin walls allow for material exchange between blood and the surrounding tissues. Finally, the capillaries merge into small veins, or venules, which in turn merge into the larger veins that return blood to the heart.

Despite large differences in their interior (*lumen*) diameter, blood vessels share a general structure consisting of three layers (*tunica*), as shown in Fig. 1.3. From a modeling perspective, the following features of each tunica merit consideration [TD09]:

- Tunica intima: The collagen fibers found in this layer contribute to a vessel's tensile strength and flexibility, and the endothelium can locally regulate blood flow through chemical secretions that affect the contractile state of overlying smooth muscle cells.

Also, valves composed of endothelial cells in the veins prevent retrograde flow (e.g., due to gravity).

- Tunica media: The elastic fibers in this layer allow vessels to flex and recoil in accord with pressure changes, and the contractile state of its smooth muscle cells are a primary determinant of lumen diameter.

- Tunica externa: In addition to elastic fibers, this layer also contains nerves that allow for regulatory action via the central nervous system.

Variations in the specific stucture and relative thicknesses of these three layers (or the absence of one or more layers) are the source of important functional differences between types of blood vessels. As sketched in Fig. 1.3, arteries have a much thicker vessel wall compared to veins of similar overall diameter, principally due to a more extensive tunica media. This additional smooth muscle allows arteries to withstand the higher pressures found in precapillary portions of circulatory routes. On the other hand, capillaries possess only a tunica intima, and consequently have very thin vessel walls to permit efficient exchange between blood and external tissues.

Besides differences between arteries, veins, and capillaries, there are also inter-arterial structural shifts according to size and distance from the heart. In the large arteries nearest to the heart, the tunica media has a higher concentration of elastic fibers; this property allows them to first expand and hold blood during systole, then recoil and drive blood towards the smaller arteries during diastole. For this ability to store and release blood, these arteries are categorized as "compliance" (or "capacitance") vessels. In the smaller arteries, and especially the arterioles, the tunica media is dominated by smooth muscle fibers, meaning that these vessels can greatly stiffen or relax in response to regulatory stimuli. In the arterioles, these changes in vascular muscle tone translate to alterations in vessel lumen diameter, allowing strong mediation of opposition to flow. For this reason, the arterioles are often called "resistance" vessels. These notions of vascular compliance and resistance are useful in modeling contexts, as they provide intuitive parameterizations for cardiovascular elements that are not spatially resolved (see Sec. 1.2.1).

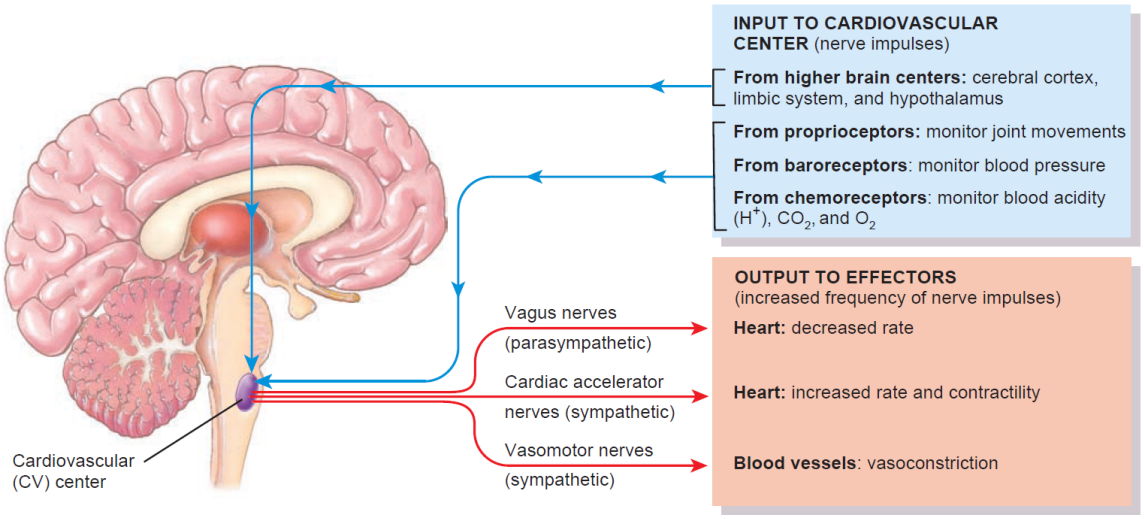

Figure 1.4: Summary of the input-output profile of the cardiovascular center [TD09].

1.1.2 Cardiovascular control

1.1.2.1 Neural control

The cardiovascular system is equipped with an array of control mechanisms whose unifying goal is to maintain adequate blood flow in all tissues. The neurally-driven portion of these mechanisms is coordinated by a subsection of the autonomic (i.e., unconscious) nervous system located in the "cardiovascular center" of the brainstem (*medulla oblongata*) [TD09].

The cardiovascular center receives and sends a variety of signals, as depicted in Fig. 1.4. Inputs from the cerebral cortex and limbic system are typically part of a response to emotional stimuli or external threats, while hypothalamic inputs are usually due to changes in temperature. This work focuses on cardiovascular response to disease and injury, so these inputs are not considered here. Since joint movement is negligible in such responses, proprioceptor input is also ignored. Finally, this work assumes that chemical concentrations in the blood remain constant, and chemoreceptor input can therefore be discarded.

Under the restrictions outlined above, the only relevant regulatory input for neural control comes from the baroreceptors. This simplified input profile is justified in cases of short-term homeostasis (on the order of minutes), as the baroreceptors are thought to be the main source of blood pressure control on such timescales [Dan98]. The baroreceptors are located

on both the aortic arch downstream of the aortic valve and on the carotid sinuses, which are small widenings of the internal carotid arteries leading into the brain. Functionally, they are mechanical-electrical pressure transducers: blood pressure first causes them to stretch in tandem with the vessel wall, followed by a conversion of this deformation into a firing rate of the neurons connected to the receptor sites. This firing rate is the first part of a negative feedback loop known as the "baroreflex": if the firing rate deviates from a homeostatic value, the cardiovascular center sends out signals to the heart and blood vessels (the "effector" organs in Fig. 1.4) to restore normal blood pressure.

As shown in Fig. 1.4, the cardiovascular center sends signals to the body through two pathways, known generally as sympathetic and parasympathetic nerves. These types of nerves are not specific to the cardiovascular center, emerging additionally from other medullary centers to provide input to (i.e., innervate) a variety of tissues besides those directly involved in the cardiovascular system (e.g., skeletal muscle or the digestive system). However, the two classes can be broadly distinguished by response type: sympathetic stimulation is usually excitatory (e.g., the "fight-or-flight" response), whereas parasympathetic stimulation is mainly inhibitory (e.g., "rest-and-digest"). As might be expected by these opposing responses, sympathetic and parasympathetic activity occur in a reciprocal fashion (i.e., increased activity in one system diminishes activity in the other) [Kor71].

In the cardiovascular system, only the heart receives both sympathetic and parasympathetic stimulation. Sympathetic nerves extend into the electrical conduction system of the heart, as well as the ventricular myocardium; as such, they can increase both heart rate (known as a "chronotropic" effect) and the force of ventricular contraction (known as an "inotropic" effect). Taken together, these effects tend to increase the amount of blood pumped out by the heart (usually called "cardiac output"), and hence increase blood pressure. By contrast, parasympathetic nerves are connected only to the heart's electrical conduction system, and can therefore only influence the heart rate. Under resting conditions, the parasympathetic system dominates: the uncontrolled rhythm of the heart's sino-atrial node (the so-called "pacemaker" of the heart) is roughly 100 beats per minute, so parasympathetic inhibition is required to achieve a normal resting rate around 75 beats per minute

[TD09]. This inhibition becomes stronger with increasing blood pressure, as a lower heart rate translates to reduced cardiac output, and thus a reduction in blood pressure.

Unlike the heart, the systemic vasculature is not innervated by the parasympathetic nervous system. Instead, sympathetic fibers are embedded in the tunica externa of both arteries and veins, mediating the tone of smooth muscle cells in the underlying tunica media. Stimulation through these fibers increases vascular muscle tone, which produces different effects on the arterial and venous halves of the circulation. Owing to their more muscular structure (see Sec. 1.1.1.2), innervated arteries (and especially arterioles) can significantly decrease their lumen diameter, resulting in an increase in systemic vascular resistance (SVR) to flow. Veins have a more compliant structure, leading them to store blood under resting conditions (this so-called "venous reservoir" contains around half of resting blood volume [Gan75, Guy91]). Thus, their constriction does not result in a significant increase in vascular resistance, but instead pushes blood out of the venous reservoir and into the systemic circulation. This mobilized venous blood increases blood pressure once it reaches the arterial side of the circulation, as its return to the veins is slowed by the heightened arterial resistance.

1.1.2.2 Hormonal and local control

Centralized regulation of the cardiovascular system by the autonomic nervous system is supplemented by hormones, which are signaling molecules that travel through the circulatory system to reach target organs. In the context of the cardiovascular system, there are several hormones that serve a regulatory purpose. For instance, epinephrine (adrenaline) and norepinephrine (noradrenaline) are released from the adrenal glands above the kidneys in response to sympathetic stimulation, causing an increase in heart rate and cardiac contractility, as well as vasoconstriction in the skin and abdominal organs and vasodilation in skeletal muscle. This type of differentiated vasomotor action is critical to the redirection of blood flow to muscles during exercise. The other principal regulatory hormones are angiotensin II, aldosterone, vasopressin, and atrial natriuretic peptide. However, because these additional hormones act globally in order to restore normal blood pressure [TD09], their effects can be

lumped into a model for the baroreflex.

In addition to hormonal control, capillary beds are capable of independent local changes to vessel lumen diameter, known as "autoregulation". These changes occur so that tissues can automatically adjust blood flow according to current metabolic demand. For instance, increased oxygen requirements during physical activity causes a release of vasodilatory chemicals in the vasculature of the heart and skeletal muscles [TD09]. Autoregulatory mechanisms are also responsible for the maintainance of adequate cerebral blood flow over a wide range of blood pressures [LCG03, DM08], and is therefore of primary importance when systemic blood pressure falls (e.g., in cases of hemorrhage).

1.2 Previous modeling efforts

Based on the discussion above, it is evident that any closed-loop cardiovascular model (i.e., in which blood completes a closed circuit) must include models for the 1) heart, 2) arteries/arterioles, 3) capillaries, and 4) venules/veins. In addition, if dynamic responses to disease or injury are desired, then the cardiovascular model must be coupled to models for regulatory mechanisms. Of course, in developing such models, tradeoffs between model fidelity and computational speed must be considered. The following section is a brief literature review, summarizing the tradeoffs made by other studies that inform the current work.

1.2.1 Zero-dimensional (lumped parameter) modeling

The simplest models for the cardiovascular system are zero-dimensional, compressing the characteristics of the heart or a group of blood vessels into three parameter types, known as "lumped parameters". These parameters are 1) resistance to capture opposition to flow, 2) compliance/capacitance (or its inverse, known as elastance) to capture vessel distensibility, and 3) inductance to capture blood inertia. Mathematically, these models produce flows according to fluid analogs of linear circuit laws (i.e., Ohm's law and Kirchoff's current/voltage laws), with pressure instead of voltage and volumetric blood flow replacing current.

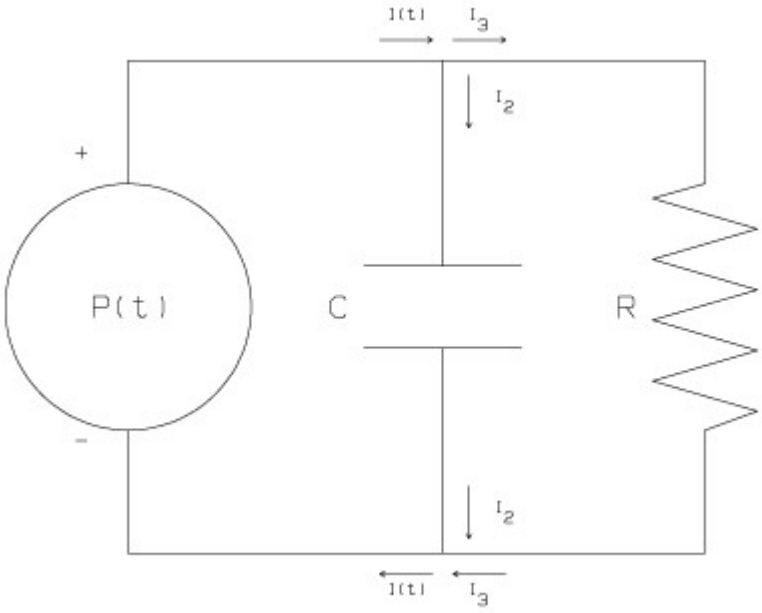

Figure 1.5: Frank's [Fra99] two-element Windkessel (diagram from [Ker17]).

As an example, the earliest model of this type was the two-element arterial Windkessel, developed by Frank [Fra99] and displayed in Fig. 1.5. As shown in the figure, it includes a time-varying pressure source to represent the heart, a capacitor to model elastic nature of the large systemic arteries, and a resistor to capture the effect of the small arteries and arterioles. Summing current at the upper node yields the arterial pressure, here assumed to be equal to pressure in the heart:

$$I(t) = \frac{P(t)}{R} + C\frac{dP}{dt}. \tag{1.1}$$

During diastole, when the heart is decoupled from the arteries by the closure of the aortic valve, $I(t) = 0$ and Eq. (1.1) can be solved directly for arterial pressure:

$$P(t) = P(t_d)e^{-(t-t_d)/RC}, \tag{1.2}$$

where t_d is the time for the start of diastole. Despite the minimal nature of this model, properly tuned values for R and C can produce relatively good agreement with experimental measurements of aortic pressure during diastole [WLW09].

Additions to the two-element Windkessel model have since been designed to incorporate aortic valve resistance and the inertia of blood in the systemic arteries; a thorough historical overview of these improvements can be found in Westerhof et al. [WLW09]. While these modifications allow the behavior of the Windkessel to better match aortic pressure measurements over the entire cardiac cycle, their spatial abstraction renders them insufficient for providing local detail. In particular, these models cannot capture the wave transport produced by elastic vessel wall motion [Moe77, Kor78], nor can they independently provide regional distributions of blood flow and pressure. Nonetheless, they are attractive for their computational simplicity, and hence often find use as outflow boundary conditions for higher-dimensional models, as further discussed in Sec. 1.2.2.

1.2.2 Higher-dimensional and multiscale modeling

To capture the wave motion omitted by lumped-parameter models, one-dimensional (or "distributed") models represent arterial segments by equations for viscous pulsatile flow in an elastic tube. The solution to these equations for a single artery was first developed in linearized form by Womersley [Wom57], who used Fourier series to obtain solutions in the frequency domain. As computing power improved, this work was extended to the systemic arterial tree to give localized vascular behavior in subsequent studies [WBD69, RJS74, Avo80, WP04]. A significant drawback to these frequency-domain approaches is their assumption of a periodic solution. This assumption is not justifiable when transient phenomena (e.g., those produced by regulatory mechanisms) occur on timescales close to that of a cardiac cycle, as is the case with baroreflex-mediated changes to heart rate and cardiac contractility [Dan98].

One-dimensional solutions in the time domain have also been developed based on both quasilinear [SFP03, Ala06] and nonlinear [SA72, ZM86, SYR92, DNP03, VT04, FLT06, RMP09] mass and momentum conservation averaged over vessel cross sections. Such solutions necessarily involve numerical solution of systems of partial differential equations, and are thus more computationally expensive than frequency domain approaches, which produce algebraic relations between both pressures in different regions and pressure and flow rate at a

fixed location. However, time domain formulations do not require a periodic solution, making them more amenable to coupling with regulatory models. Time-domain numerical solutions to three-dimensional flows through patient-specific geometries also exist [TF09, BTF12], but the present work focuses on reduced-order modeling, so this type of fully-resolved modeling will not be further discussed.

Even in the limited context of one-dimensional models, the finer level of detail prohibits global usage; it would not be feasible to discretize the complete $\mathcal{O}(10^8)$ meters of systemic vasculature [LE04], and even if it were, flow in capillary beds cannot be modeled through continuum techniques, as the lumen diameter becomes comparable to blood cell size [TD09]. An efficient approach in this case is to employ multiscale modeling, in which higher-dimensional subsystems representing domains of interest are coupled to lower-dimensional subsystems at inflow and/or outflow boundaries. In one common architecture, the major systemic arteries are treated as a one-dimensional network, and are coupled to lumped-parameter models of the microcirculation, systemic veins, and left ventricle [FLT06, RMP09, SYR92]. This subclass of models is open-loop, meaning that no consideration is given to the return of blood to the heart. More complex extensions exist, including one-dimensional venous networks [MT14], coupling to three-dimensional models of specific arteries [QV03, KVF09, LBB11], and closed-loop models of heterogeneous dimensionality [DNP03, OOT05, Goh07, LTH09a, LTH09b, BTF12, MVF13].

1.2.3 Regulatory control modeling

1.2.3.1 Baroreflex modeling

As discussed in Sec. 1.1.2, the sole neural regulatory mechanism relevant to this work is the baroreflex, which can be split into three pieces for modeling purposes (see Fig. 1.4):

- The baroreceptors, for which the firing rate of nerve impulses sent to the cardiovascular center are a function of arterial pressure (the "afferent" part)

- The cardiovascular center, which converts baroreceptor impulses into sympathetic and parasympathetic nerve impulses
- The heart and vasculature, which change their behavior according to sympathetic and parasympathetic stimulation (the "efferent" part)

Separate modeling of these parts has been extensively conducted over the past half century (as reviewed by Danielsen [Dan98]), and is necessary for understanding the dynamics of nerve impulses in response to different stimuli. Modeling can also be accomplished more simply by abstraction of the afferent firing rate [Dan98, BKS07]. This reduced implementation is a two-step process: arterial pressure is converted directly into sympathetic/parasympathetic activity, which in turn modulates lumped-parameter descriptions of the heart and vasculature. This simplified model is attractive for this study, as it retains the influence of the baroreflex on cardiovascular dynamics with minimal extraneous detail.

1.2.3.2 Autoregulatory modeling

With respect to cardiovascular autoregulation, a substantial share of modeling work in recent years has focused on cerebral processes, as these localized processes are necessary to hold cerebral blood flow constant under changing systemic blood pressure. This characteristic is of particular interest to this work, as it counteracts the baroreflex; e.g., the baroreflex induces global vasoconstriction when the baroreceptors detect low blood pressure, which requires an opposing cerebral vasodilation to avoid reduced brain tissue perfusion. A model of this type is therefore needed for accurate prediction of cerebrovascular responses to disease and injury.

As noted in the review by David and Moore [DM08], cerebral autoregulatory modeling can be broadly split into two categories: physiologically-based models that attempt to mathematically describe autoregulatory processes, and empirical models that simply attempt to fit experimental measurements of cerebral blood pressure and flow rate. The former approach has the twin benefits of allowing for a better understanding of the underlying physiology, and also being more readily applicable to lumped-parameter vascular models (i.e., the autoregulatory model can follow the baroreflex framework, driving changes in cerebral

resistance/compliance). For these reasons, the physiological approach will be pursued in this work.

Akin to their cardiovascular counterparts, mathematical descriptions of cerebral autoregulation have been developed at varying levels of complexity. Banaji et al. [BTD05] provide an example at the most resolved end of the spectrum, directly modeling processes from the scale of ion transport up to the scale of the entire cerebral vasculature (the latter of which is represented in lumped parameter form). Though elucidating physiological mechanisms at such small scales can aid in understanding cellular mechanics, it is less crucial for studying systemic cardiovascular responses. In these cases, cerebral autoregulation can be modeled with less complexity by allowing changes in cerebral resistance and/or compliance to be functions of deviations in cerebral pressure or blood flow from their reference values [UD91]. This type of modeling is advantageous for the present study because it allows for a direct, natural interaction between the cerebral vasculature's fluid dynamics and its local control mechanisms. Furthermore, it can be extended in a straightforward way to include chemically-mediated responses by making the reference values functions of arterial carbon dioxide concentration [LCG03].

1.3 Objectives

Despite the extensive body of work available on cardiovascular models subject to regulatory mechanisms, most involving injury response do so at the compartmental level. This spatial abstraction leads to insufficient spatial resolution to capture wave dynamics and fluid dynamical data at the level of the major arteries. By contrast, a model possessing these characteristics would allow for realistic simulation of the differentiated responses across the body to localized cardiovascular injuries. Furthermore, owing to the difficulty of parameter tuning, cardiovascular models tend to be validated against expected ranges for cohorts of similar patients; matching models to individual patient data is a relatively new and unexplored venue [TF09]. The present work is an attempt to fill these twin voids, and therefore has the following objectives:

1. Develop a closed-loop model of the cardiovascular system with sufficient spatial resolution to provide organ-level fluid dynamical data (i.e., pressure and flow rate in the major arteries)

2. Couple the cardiovascular model to models of the baroreflex to allow for accurate representation of dynamic responses to disease and injury

3. Leverage techniques from data assimilation [Eve03] to reduce computational cost and enable patient-specific modeling

Chapters 2 and 3 focus on the first two objectives by detailing the implementation and results for a full-body multiscale cardiovascular model with feedback control. Chapters 4 and 5 then address the final objective through construction and testing of a framework for patient-specific modeling that generalizes across cardiovascular models. Finally, Chapter 6 concludes with a summary of accomplished goals and possible future directions.

CHAPTER 2

Construction of a Full-Scale Cardiovascular Model

As currently implemented, the overall model in this study couples zero-dimensional submodels of the heart, pulmonary vasculature, peripheral vasculature, and systemic veins with a one-dimensional submodel of the systemic arteries. The zero-dimensional submodels are in turn modulated by a baroreflex model. A high-level description of the connections between models is given in Fig. 2.1, followed by a complete connectivity diagram of the one-dimensional network in Fig. 5.6. In this chapter, each submodel is described, and the approach to 0D-1D coupling is outlined. Unless otherwise noted, numerical values for all model parameters are reported at the end of the chapter.

2.1 Systemic arterial submodel

2.1.1 Basic model of a single artery

One-dimensional modeling of the major arteries essentially follows Sherwin et al. [SFP03], but the main portions of their argument are reproduced here for clarity. Mass and momentum conservation statements are derived from first principles using the control volume shown in Fig. 2.3. In this control volume, quantities of interest are assumed to vary only in the axial (x) direction, so the three dependent variables are cross-sectional area $A = A(x,t)$, $u = u(x,t)$ (or equivalently volumetric flow rate $Q = Au$), and pressure $P = P(x,t)$. The flow is also assumed to be incompressible and Newtonian (i.e., ρ and μ are constants).

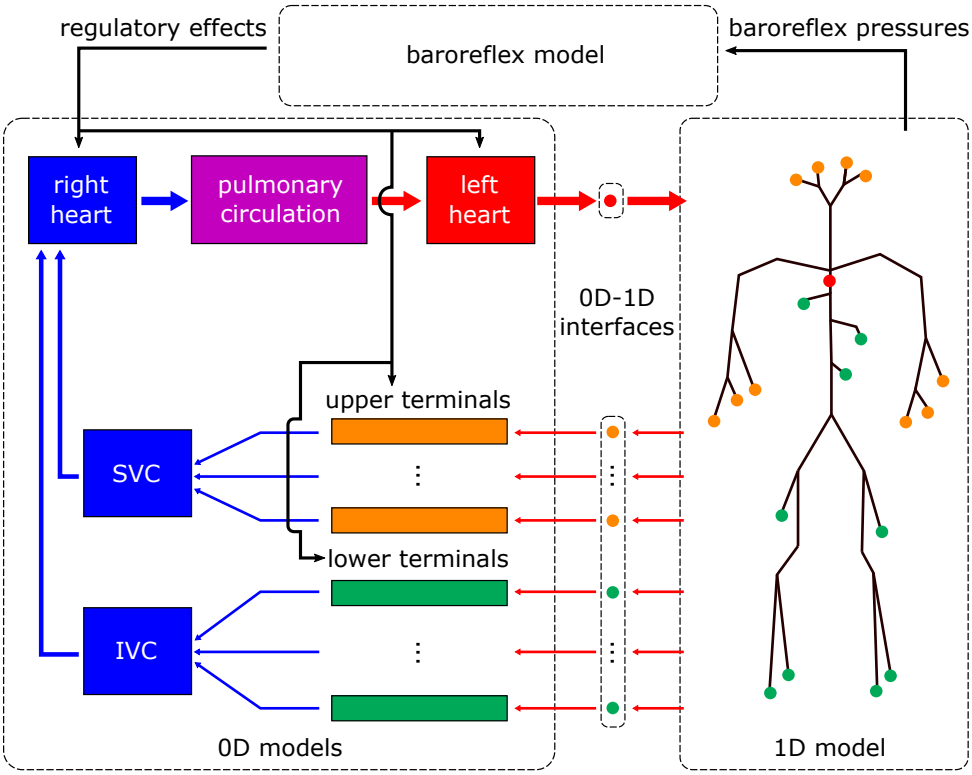

Figure 2.1: A high-level view of the closed-loop model architecture.

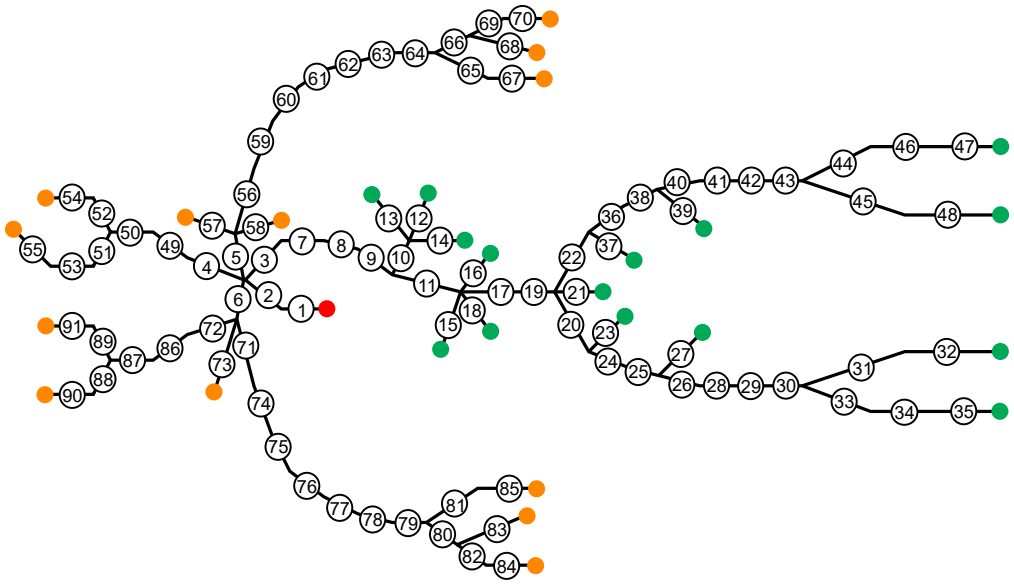

Figure 2.2: Connectivity diagram of complete one-dimensional arterial network. Artery ID numbers match tables found at the end of the chapter, while terminal annotations follow Fig. 2.1.

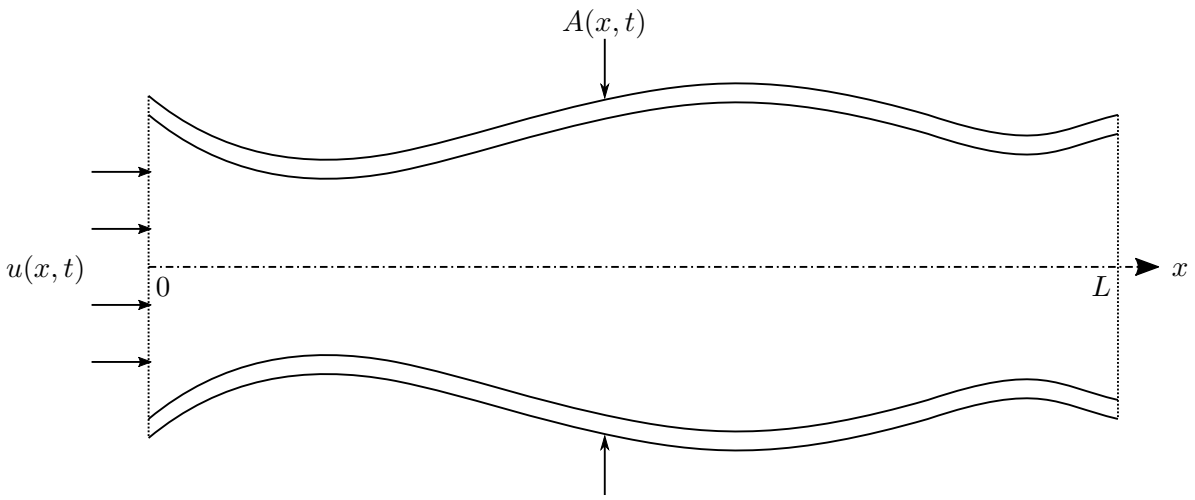

Figure 2.3: One-dimensional control volume representation of a single artery (adapted from [SFP03]). Note the domain boundaries: $x \in [0, L]$.

2.1.1.1 Mass conservation

In general, Reynolds' transport theorem applied to mass conservation yields

$$0 = \frac{\partial}{\partial t} \int_{\mathrm{CV}} \rho \, dV + \int_{\mathrm{CS}} \rho \left(\vec{v} \cdot \vec{n} \right) dA, \tag{2.1}$$

where CV and CS respectively denote the control volume and its surface, $V = \int_0^L A \, dx$ is the volume, and $\vec{n}$ is the outward unit normal. Assuming artery length to be constant in time, Eq. (2.1) simplifies to

$$0 = \rho \int_0^L \left(\frac{\partial A}{\partial t} + \frac{\partial \left(Au \right)}{\partial x} \right) dx, \tag{2.2}$$

where the second term in the integrand has been condensed according to the second fundamental theorem of calculus:

$$(\rho A u)_L - (\rho A u)_0 = \int_0^L \frac{\partial \left(Au \right)}{\partial x} dx. \tag{2.3}$$

Finally, since the domain size is arbitrary, Eq. (2.2) requires that the integrand be zero, leading to the statement of area-averaged differential mass conservation used in this study:

$$\frac{\partial A}{\partial t} + \frac{\partial (Au)}{\partial x} = 0. \tag{2.4}$$

2.1.1.2 Momentum conservation

Momentum conservation again begins with Reynolds' transport theorem, this time leading to a balance between forces and momentum fluxes in the axial direction:

$$F_x = \frac{\partial}{\partial t} \int_0^L \rho A u \, dx + \int_{A(L,t)} \rho u^2 \, dA - \int_{A(0,t)} \rho u^2 \, dA \tag{2.5}$$

The left-hand side is modeled as the sum of pressure forces at the ends of the segment, integrated sidewall pressure force (projected into the axial direction), and an integrated friction force per unit length f:

$$F_x = (PA)_0 - (PA)_L + \int_0^L \left(P \frac{\partial A}{\partial x} + f \right) dx. \tag{2.6}$$

The momentum fluxes on the right-hand side of Eq. (2.5) can be integrated directly due to the assumption of uniform flow at a fixed cross-section:

$$\int_{A(L,t)} \rho u^2 \, dA - \int_{A(0,t)} \rho u^2 \, dA = (\rho u^2 A)_L - (\rho u^2 A)_0. \tag{2.7}$$

This momentum flux difference, along with the first two terms on the right-hand side of Eq. (2.6), can be written in integral form akin to Eq. (2.3):

$$(\rho u^2 A)_L - (\rho u^2 A)_0 = \rho \int_0^L \frac{\partial (u^2 A)}{\partial x} \, dx, \quad (PA)_0 - (PA)_L = -\int_0^L \frac{\partial (PA)}{\partial x} \, dx. \tag{2.8}$$

Assuming arterial length to be independent of time, Eqs. (2.1) through (2.8) can be combined under a single integral:

$$\int_0^L \left[\frac{1}{\rho} \left(-\frac{\partial (PA)}{\partial x} + P \frac{\partial A}{\partial x} + f \right) - \left(\frac{\partial (uA)}{\partial t} + \frac{\partial (u^2 A)}{\partial x} \right) \right] dx = 0. \tag{2.9}$$

The second group in the integrand is simplified through expansion and application of Eq. (2.4):

$$\frac{\partial\left(uA\right)}{\partial t}+\frac{\partial\left(u^{2}A\right)}{\partial x}=A\left[\frac{\partial u}{\partial t}+\frac{\partial}{\partial x}\left(\frac{u^{2}}{2}\right)\right]+u\cancelto{0}{\left(\frac{\partial A}{\partial t}+\frac{\partial\left(Au\right)}{\partial x}\right)}. \tag{2.10}$$

Now, since the integral in Eq. (2.9) must hold for an arbitrary control volume, the integrand must be zero. Combining this conclusion with the result in Eq. (2.10) leads to the following expression for differential momentum conservation in the axial direction:

$$\frac{\partial u}{\partial t}+\frac{\partial}{\partial x}\left(\frac{u^{2}}{2}\right)=-\frac{1}{\rho}\frac{\partial P}{\partial x}+\frac{f}{\rho A}, \tag{2.11}$$

where the pressure terms have been condensed through the product rule.

2.1.1.3 A constitutive relation, frictional modeling, and the complete system

To form a closed system for the unknowns A, u, and P, a starting point is to supplement equations (2.4) and (2.11) with a constitutive relation between force perpendicular to the vessel wall (i.e., pressure) and wall deformation (i.e., area). A common assumption is linear elastic deformation [SFP03, Ala06, FLT06, LTH09a], from which Laplace's law yields

$$P=\beta(\sqrt{A}-\sqrt{A_{0}}). \tag{2.12}$$

In Eq. (2.12), β is a stiffness parameter relating the artery's geometric and mechanical properties:

$$\beta=\frac{\sqrt{\pi}hE}{\left(1-\nu^{2}\right)A_{0}}, \tag{2.13}$$

where h is wall thickness, E is Young's modulus, A_0 is the lumen cross-sectional area at zero transmural pressure, and ν is Poisson's ratio (wall incompressibility is assumed in this study, so $\nu=0.5$). Lastly, a linear damping model for f is adopted from Alastruey [Ala06] by assuming a nearly flat velocity profile (shown *in vivo* to be valid in the large arteries [STL69]):

$$f = -22\mu\pi u. \tag{2.14}$$

Finally, Eqs. (2.4) and (2.11) can be combined with Eqs. (2.12) through (2.14) to form a complete system of equations in A and u:

$$\begin{gathered}\frac{\partial \mathbf{U}}{\partial t} + \frac{\partial \mathbf{F}(\mathbf{U})}{\partial x} = \mathbf{S}, \\ \mathbf{U} = \begin{bmatrix} A \\ u \end{bmatrix}, \quad \mathbf{F}(\mathbf{U}) = \begin{bmatrix} Au \\ \beta\sqrt{A}/\rho + u^2/2 \end{bmatrix}, \quad \mathbf{S} = \begin{bmatrix} 0 \\ -22\pi\nu u/A \end{bmatrix},\end{gathered} \tag{2.15}$$

2.1.1.4 Characteristic form

The system given by Eqs. (2.15) can be placed into so-called "characteristic form" by first writing it in non-conservative form [SFP03, Ala06]:

$$\begin{gathered}\frac{\partial \mathbf{U}}{\partial t} + \mathbf{H}(\mathbf{U})\frac{\partial \mathbf{U}}{\partial x} = \mathbf{S}, \\ \mathbf{H}(\mathbf{U}) = \begin{bmatrix} u & A \\ \beta/2\rho\sqrt{A} & u \end{bmatrix}.\end{gathered} \tag{2.16}$$

The left eigenvectors $\mathbf{L}$ and associated matrix of eigenvalues $\mathbf{\Lambda}$ of $\mathbf{H}(\mathbf{U})$ (i.e., such that $\mathbf{LH} = \mathbf{\Lambda L}$) are

$$\mathbf{L} = \begin{bmatrix} c/A & 1 \\ -c/A & 1 \end{bmatrix}, \quad \mathbf{\Lambda} = \begin{bmatrix} u + c & 0 \\ 0 & u - c \end{bmatrix}. \tag{2.17}$$

Premultiplying Eq. (2.16) by $\mathbf{L}$ and defining a change of variables $\partial \mathbf{W}/\partial \mathbf{U} = \mathbf{L}$ yields the characteristic system

$$\frac{\partial \mathbf{W}}{\partial t} + \mathbf{\Lambda}\frac{\partial \mathbf{W}}{\partial x} = \mathbf{LS},$$

$$\mathbf{W} = \begin{bmatrix} W_1 \\ \\ W_2 \end{bmatrix} = \begin{bmatrix} u + 4\sqrt{\frac{\beta}{2\rho}}(A^{1/4} - A_0^{1/4}) \\ u - 4\sqrt{\frac{\beta}{2\rho}}(A^{1/4} - A_0^{1/4}) \end{bmatrix} = \begin{bmatrix} u + 4(c - c_0) \\ \\ u - 4(c - c_0) \end{bmatrix}, \tag{2.18}$$

where $W_{1,2}$ are the characteristic variables (or Riemann invariants). Note that the expressions for W_1 and W_2 in Eqs. (2.18) can be combined to express area and average velocity as

$$\begin{aligned} A &= \left(\frac{2\rho}{\beta}\right)^2 \left(\frac{W_1 - W_2}{8} + c_o\right)^4, \\ u &= \frac{W_1 + W_2}{2}. \end{aligned} \tag{2.19}$$

The relations (2.19) are important in the schemes for the 0D-1D boundaries as well as the interior boundaries of the 1D network (i.e., at branching points).

2.1.2 Arterial numerical solution

2.1.2.1 Discretization of a single artery

To spatially discretize the system of equations (2.15), each arterial branch is split into eleven uniformly-spaced nodes (i.e., for branch i with length $L^{(i)}$, $\Delta x^{(i)} = L^{(i)}/10$). Local results from grid refinement using 51 nodes per branch are presented for the longest artery in Fig. 2.4. It was also confirmed that the global behavior of the model (as quantified in Table 3.2) varied by less than 1% across all measured parameters under refinement. For time discretization, the CFL was fixed at 0.5, and Δt was chosen to satisfy this constraint according to the following minimization:

$$\Delta t = \min_i \left(\frac{\mathrm{CFL}\Delta x^{(i)}}{c_0^{(i)}}\right), \tag{2.20}$$

where c_0 is the pulse wave velocity at zero transmural pressure:

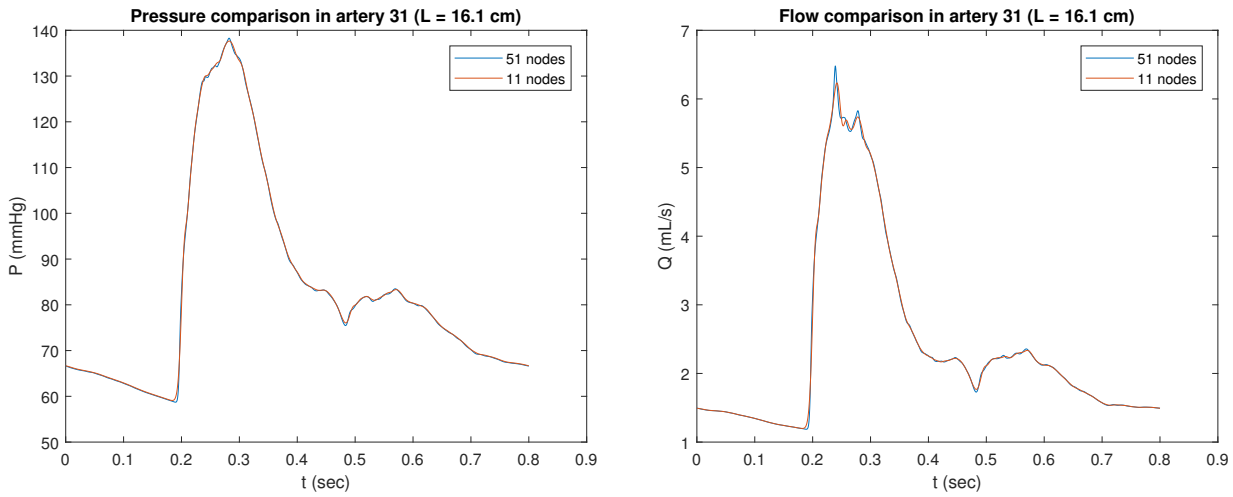

Figure 2.4: Selected localized results from a grid refinement study in the one-dimensional arterial network.

$$c_0 = \sqrt{\frac{\beta}{2\rho}} A_0^{1/4}. \tag{2.21}$$

With the above discretization, each artery's interior nodes are advanced in time using a 3rd-order TVD Runge-Kutta/CWENO method [SO88, NKS17] applied to Eqs. (2.15).

2.1.2.2 Interior boundaries (arterial branching)

The systemic arteries constitute a branching network in which a parent vessel divides into two or more daughter vessels. Fig. 2.5 illustrates the model for these divisions. At such a junction, continuity of mass flow and total pressure $P_t = P + \frac{1}{2}\rho(Q/A)^2$ are imposed [FLT06]. For a parent vessel of index p with children $c_1, c_2, \ldots, c_m$, doing so yields

$$\begin{aligned} Q_p^{(n+1)} &= Q_{c_1}^{(n+1)} + Q_{c_2}^{(n+1)} + \ldots + Q_{c_m}^{(n+1)} \\ P_{t,p}^{(n+1)} &= P_{t,c_1}^{(n+1)} = P_{t,c_2}^{(n+1)} = \ldots = P_{t,c_m}^{(n+1)}, \end{aligned} \tag{2.22}$$

where n denotes the current time step.

The nonlinear algebraic system (2.22) has $m+1$ equations in $2(m+1)$ unknowns (the

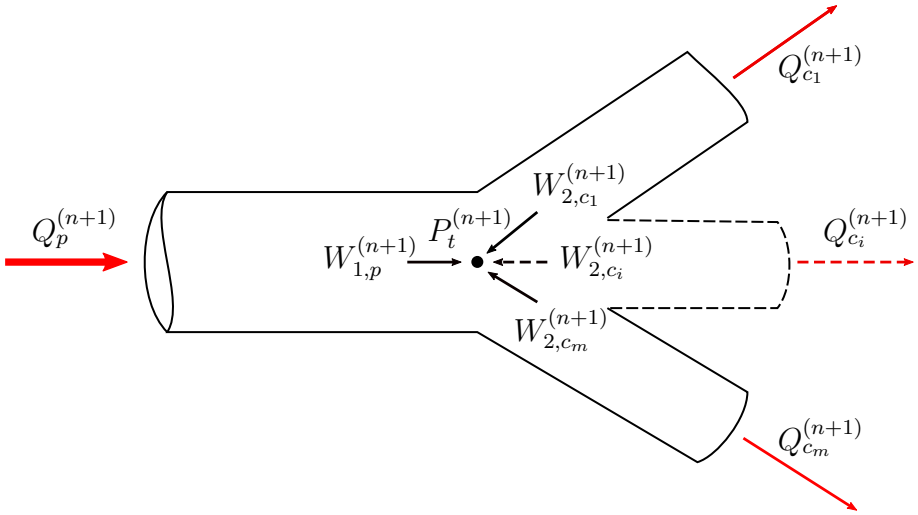

Figure 2.5: Schematic of an arterial splitting node. The index i ranges from 1 to m, the number of children at the split, while the index n denotes the current time step. In the spatial discretization, the parent's most distal node coincides with the most proximal node of each child.

flow rate/area pairs for each vessel). For closure, the characteristic variables $W_{1,2}$ presented in Eqs. (2.18) are employed. These characteristic variables travel with velocities

$$\lambda_{1,2} = \frac{Q}{A} \pm \sqrt{\frac{\beta}{2\rho}} A^{1/4} = u \pm c. \tag{2.23}$$

Under physiological conditions, $u \ll c$, so $W_{1,2}$ will always travel forwards and backwards, respectively. As such, W_1 can be extrapolated forward from the interior of the parent artery, and W_2 backwards from each of the children. Concretely, assuming the parent artery to have a length L_p gives

$$\begin{aligned} W_{1,p}^{(n+1)}(x = L_p) &= W_1^{(n)}(x = L_p - \lambda_1^{(n)}\Delta t) - 22\pi\nu \frac{u^{(n)}(x = L_p - \lambda_1^{(n)}\Delta t)}{A^{(n)}(x = L_p - \lambda_1^{(n)}\Delta t)} \\ W_{2,c}^{(n+1)}(x = 0) &= W_2^{(n)}(x = -\lambda_2^{(n)}\Delta t) - 22\pi\nu \frac{u_c^{(n)}(x = -\lambda_2^{(n)}\Delta t)}{A_c^{(n)}(x = -\lambda_2^{(n)}\Delta t)}, \end{aligned} \tag{2.24}$$

where $W_{1,2}^{(n)}$ are calculated by interpolating between the last two nodes of the parent and the

first two nodes of each child. Equations (2.22) and (2.24) form a closed nonlinear algebraic system in $2(m+1)$ unknowns, and are solved iteratively using Newton's method.

2.2 Cardiac submodel

The heart model implemented in this study belongs to a class of lumped-parameter models known as "elastance" models, first proposed by Suga et al. [SSS73] and commonly used in other works [Dan98, OD03, OOT05, FLT06, Goh07, KVF09, LTH09b, LTH09a, RMP09, MDP12, BTF12, MT14]. In the following description, the subscript v represents either ventricle, while the subscript a represents either atrium. Also, for some equations it is necessary to define a time within a heart period $\hat{t} = \mathrm{mod}(t, t_h)$, where $t_h = 1/f_0$ is the heart period. In this model, the left and right ventricles are represented as pressure-volume relationships of the form

$$P_v = E_v(\hat{t})(V_v - V_{v,un}), \tag{2.25}$$

where V_v is ventricular volume, $V_{v,un}$ is a modeling parameter representing volume at zero diastolic pressure (sometimes called unstressed volume), and $E_v(\hat{t})$ is a time-varying elastance intended to model ventricular pumping. Given a minimum diastolic elastance $E_{\min}$ and maximum systolic elastance $E_{\max}$, it is defined using the 'two-Hill' function [SMW96, MDP12]

$$E_v(\hat{t}) = k\left(\frac{g_1}{1+g_1}\right)\left(\frac{1}{1+g_2}\right) + E_{\min}, \tag{2.26}$$

where g_1 and g_2 describe each 'hill'

$$g_1 = \left(\frac{\hat{t}}{\tau_1}\right)^{m_1}, \quad g_2 = \left(\frac{\hat{t}}{\tau_2}\right)^{m_2}, \tag{2.27}$$

and k scales their product:

$$k = \frac{E_{\max} - E_{\min}}{\max\left[\left(\frac{g_1}{1+g_1}\right)\left(\frac{1}{1+g_2}\right)\right]}. \tag{2.28}$$

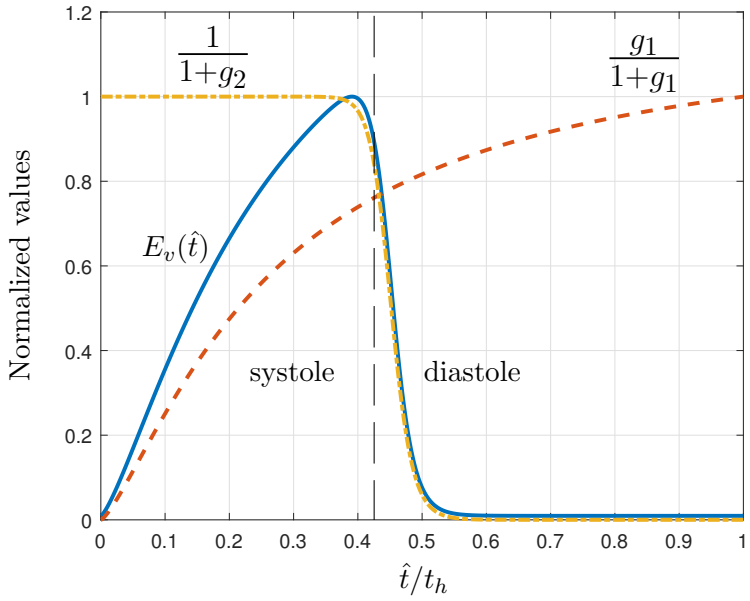

Figure 2.6: A typical ventricular elastance curve from the 'two-Hill' function alongside its component Hill functions. Each curve has been normalized by its maximum value. The vertical dashed line demarcates the systolic and diastolic phases.

A typical elastance curve and constituent Hill functions are shown in Fig. 2.6, illustrating the gradual rise in elastance (and hence ventricular pressure) during systole, followed by a sharp fall in both quantities during early diastole.

Atrial pressures are described using the same form as Eq. (2.25), except that elastance is taken as a constant (i.e., the atria are modeled as passive elastic chambers). More complex compartmental models accounting for atrial contraction are available [BTF12, LTH09a, LTH09b], but their effects on systemic arterial hemodynamics are negligible: atrial systole occurs within ventricular diastole, during which the left ventricle and systemic arteries are decoupled. Since this study is concerned with local hemodynamics only in the systemic circulation, this modeling aspect is omitted for computational simplicity.

To determine the time evolution of ventricular volume, conservation of mass for an incompressible fluid is applied:

$$\frac{dV_v}{dt} = Q_a - Q_v, \tag{2.29}$$

where Q_a and Q_v denote atrial and ventricular flow rates, respectively. Note that these flow rates can be nonzero only when the appropriate heart valves are open. To model atrioventricular valve closure, atrial flow rates are set to zero when P_v exceeds P_a. For the right ventricle only, the pulmonary valve is closed once Q_v becomes negative (aortic valve modeling is discussed in Sec. 2.5.1). Atrial volumes are determined in a fashion similar to Eq. (2.29):

$$\frac{dV_a}{dt} = Q_{ve} - Q_a, \tag{2.30}$$

where Q_{ve} indicates the rate of venous return. For the right atrium, this return is determined from the peripheral vascular model as the sum of the flows through lumped-parameter compartments representing the inferior and superior vena cavae. By contrast, the left atrium's venous return is taken as the flow rate through the second venous compartment of the pulmonary vascular model. Atrioventricular flow rates are determined by the following evolution equation:

$$\frac{dQ_a}{dt} = \frac{1}{L_a}(P_a - P_v) - \frac{R_a}{L_a}Q_a, \tag{2.31}$$

where L_a represents inductance and R_a is atrial resistance.

For the right ventricle only, the flow rate advances in time as

$$\frac{dQ_{rv}}{dt} = \frac{1}{L_{rv}}(P_{rv} - P_e), \tag{2.32}$$

where L_v is the inductance and P_e is the pulmonary arterial pressure into which the right ventricle ejects:

$$P_e = R_e Q_{rv} + P_1, \tag{2.33}$$

where R_e is the pulmonary artery's resistance and P_1 is the pressure in the most proximal compartment of the pulmonary circulation. Note that the flow rate out of the left ventricle is not determined in a manner analogous to Eq. (2.32) when the aortic valve is opened.

Rather, it is determined by coupling to the systemic 1D model, as described in Sec. 2.5.1. Finally, all time evolutions described in this section are discretized using the forward Euler method.

2.3 Pulmonary submodel

The pulmonary circulation is subdivided into five lumped-parameter compartments characterized by linear circuit elements, following the work of Danielsen [Dan98]. In the following description, subscripts ranging from 1 to 5 indicate movement from the large arteries to the large veins. In all five compartments, volume changes according to conservation of mass:

$$\begin{aligned} \frac{dV_1}{dt} &= Q_v - Q_1, \\ \frac{dV_i}{dt} &= Q_{i-1} - Q_i \quad i = 2, \ldots, 5. \end{aligned} \tag{2.34}$$

In the first and fifth compartments, an inductance is included to model the inertia of blood within the large arteries and veins. As such, the flow rate in these sections are given by

$$\frac{dQ_i}{dt} = \frac{1}{L_i}(P_i - P_{i+1}) - \frac{R_i}{L_i}Q_i. \quad i = 1, 5, \tag{2.35}$$

where R_i is compartmental resistance and L_i is inductance. The middle compartments contain only a resistance (i.e., viscous effects are assumed to dominate inertial effects, as is the case in small vessels and capillaries [TD09]), resulting in simple algebraic relations for the flow rate:

$$Q_i = \frac{P_i - P_{i+1}}{R_i}, \quad i = 2, 3, 4. \tag{2.36}$$

Finally, each compartment is assumed to deform passively, resulting in the following relationships for pressure:

$$P_i = \frac{1}{C_i}(V_i - V_{i,un}), \quad i = 1, \ldots, 5, \tag{2.37}$$

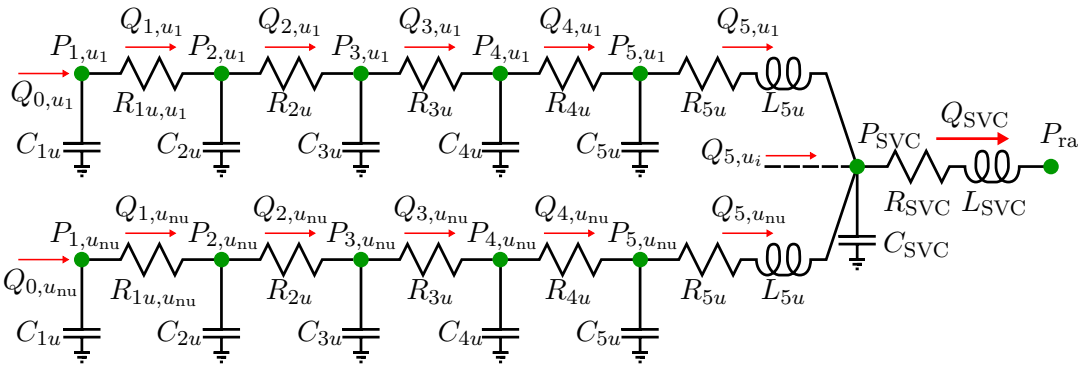

Figure 2.7: Schematic of the compartments representing the upper peripheral circulation and superior vena cava. The second subscript u indicates an upper terminal artery, with the associated index i running from 1 to the number of upper body terminal arteries nu. The lower compartments and inferior vena cava have an identical structure. The left-hand terminals are connected to 1D arterial domains, while the right-hand terminal is connected to the right atrium.

where the last terms in each equation represent unstressed volumes, and each parameter C_i denotes the compliance of that compartment. As with the cardiac submodel, equations are discretized using the forward Euler method where necessary.

2.4 Peripheral submodel

To save computational effort, the 1D network only explicitly models 91 of the largest arteries in the systemic vasculature. However, it is still necessary to account for the hemodynamic effects of the smaller arteries, arterioles, capillary beds, and venous network. To do so, all terminal arteries (i.e., arteries that do not branch into explicitly represented daughter vessels) are coupled to zero-dimensional models similar to those used for the pulmonary circulation. In total, each terminal artery is associated with five terminal compartments, as illustrated in Fig. 2.7. Each compartment's volume is determined by conservation of mass, similarly to Eq. (2.34), with the most proximal incoming flow rate determined by iterative coupling to the 1D model (see Sec. 2.5.2). Compartmental pressures relate to volume through capacitance as in Eq. (2.37), and flow rates in the four most proximal

compartments relate to pressure differences analogously to Eq. (2.36). The most distal compartment includes an inductance for the large veins, so its flow rate changes akin to Eq. (2.35). These distal compartments then connect to appropriate vena caval compartments (e.g., upper body terminal compartments connect to the superior vena caval compartments), whose pressures and flow rates are calculated following Eqs. (2.37) and (2.35).

2.5 0D-1D coupling

To couple the 1D model of the major arteries to the compartmental models for the remaining cardiovascular system, an iterative approach based on the work of Liang et al. [LTH09a] is employed. This method makes use of Eqs. (2.19), which show that $W_{1,2}$ completely specify A and u at a node, and the fact that $W_{1,2}$ can be extrapolated from interior nodes of the 1D domain by following characteristic lines [SFP03, Ala06, LTH09a].

2.5.1 Proximal coupling

At the proximal boundary of the 1D network, in the event that the aortic valve is closed (i.e., during diastole), it is necessary to enforce $Q_{lv} = 0$. From Eqs. (2.19), this condition requires $W_1 = -W_2$, leading to the following time advancement scheme:

1. Update W_2 at the boundary by extrapolating from interior nodes:

$$W_{2,\mathrm{ao}}^{(n+1)}(x=0) = W_{2,\mathrm{ao}}^{(n)}(x=-\lambda_2^{(n)}\Delta t) - 22\pi\nu\frac{u_{\mathrm{ao}}^{(n)}(x=-\lambda_2^{(n)}\Delta t)}{A_{\mathrm{ao}}^{(n)}(x=-\lambda_2^{(n)}\Delta t)}. \tag{2.38}$$

2. Set W_1 so that $Q_{lv} = 0$:

$$W_{1,\mathrm{ao}}^{(n+1)}(x=0) = -W_{2,\mathrm{ao}}^{(n+1)}(x=0). \tag{2.39}$$

3. Update A at the proximal boundary according to Eqs. (2.19):

$$A_{\mathrm{ao}}^{(n+1)}(x=0) = \left(\frac{2\rho}{\beta_{\mathrm{ao}}}\right)^2\left(\frac{W_{1,\mathrm{ao}}^{(n+1)}(x=0) - W_{2,\mathrm{ao}}^{(n+1)}(x=0)}{8} + c_{0,\mathrm{ao}}\right)^4 \tag{2.40}$$

4. Finally, update the left ventricular state using a forward Euler discretization of Eq. (2.29) (noting $Q_{lv} = 0$ during diastole):

$$\begin{aligned} V_{lv}^{(n+1)} &= V_{lv}^{(n)} + \Delta t Q_{la}^{(n)}, \\ P_{lv}^{(n+1)} &= E_{lv}^{(n+1)}(V_{lv}^{(n+1)} - V_{lv,un}). \end{aligned} \tag{2.41}$$

Note that this process allows decoupling of the left ventricle from the aorta during diastole (i.e., no ventricular outflow) while still allowing for wave reflections from the proximal boundary within the 1D domain [FLT06].

In contrast to the closed valve condition outlined above, the open valve condition fully couples the left ventricle and systemic arteries. To do so, a variant of the aortic valve model proposed by Mynard et al. [MDP12] is employed. In this model, the pressure drop across the valve accounts for viscous, inertial, and 'Bernoulli' losses:

$$P_{lv} - P_{\text{ao}} = BQ_{lv}|Q_{lv}| + L\frac{dQ_{lv}}{dt} + RQ_{lv}, \tag{2.42}$$

where B and L depend on the effective orifice area A_{eff}:

$$B = \frac{\rho}{2A_{\text{eff}}^2}, \quad L = \frac{\rho l_{\text{eff}}}{A_{\text{eff}}}, \tag{2.43}$$

and l_{eff} is a constant characteristic length scale for flow across the valve. A_{eff} varies with time according to a valve state index ζ, $0 \leq \zeta \leq 1$:

$$A_{\text{eff}} = A_{\text{ann}}\zeta(t), \tag{2.44}$$

where A_{ann} is the maximum transvalvular area and ζ changes according to its current state and the transvalvular pressure difference $\Delta P = P_{lv} - P_{\text{ao}}$:

$$\begin{aligned} \frac{d\zeta}{dt} &= (1-\zeta)K_{\text{vo}}\Delta P, \quad \Delta P > 0 \\ \frac{d\zeta}{dt} &= \zeta K_{\text{vc}}\Delta P, \quad \Delta P < 0. \end{aligned} \tag{2.45}$$

In Eq. (2.45), K_{vo} and K_{vc} are rate constants for valve opening and closing, respectively. A backward Euler discretization of Eqs. (2.42) and (2.45), along with a similar discretization of Eq. (2.29), the constitutive relations in Eqs. (2.12) and (2.25), and the characteristic relations in Eq. (2.19) are solved simultaneously using Newton-Raphson iteration and the extrapolated interior characteristic from Eq. (2.38). Coupling in this manner allows for wave interactions between the left ventricle and the systemic arterial network [FLT06].

2.5.2 Distal coupling

At the distal end of the 1D network, terminal arteries are coupled to the most proximal 0D compartment outlined in Sec. 2.4. To do so, the process is very similar to the open valve conditions for the proximal 1D boundary, except that the characteristic variable leaving the 1D domain is W_1, rather than W_2. In this case, an algebraic system is formed from the characteristic relations given in Eq. (2.19), the constitutive relations in Eqs. (2.37) and (2.12), and a semi-implicit discretization of mass conservation:

$$V_1^{(n+1)} = V_1^n + \Delta t(Q_{\text{1D}}^{(n+1)} - Q_1^n) \tag{2.46}$$

This algebraic system is solved at each distal coupling point using the Newton-Raphson method and W_1 extrapolated from the 1D domain in a manner analogous to Eq. (2.24).

2.6 Baroreflex submodel

To simulate regulation by the central nervous system in the 0D models, a modified version of the model developed by Danielsen [Dan98] and extended by Blanco et al. [BTF12] is implemented. First, an average pressure over all the baroreflex sites is defined as an activation signal:

$$\bar{P}_{\text{baro}} = \frac{1}{3t_h}\left(\int_0^{t_h} P_{aa}(x=0)\,dt + \int_0^{t_h} P_{lc}(x=0)\,dt + \int_0^{t_h} P_{rc}(x=0)\,dt\right), \tag{2.47}$$

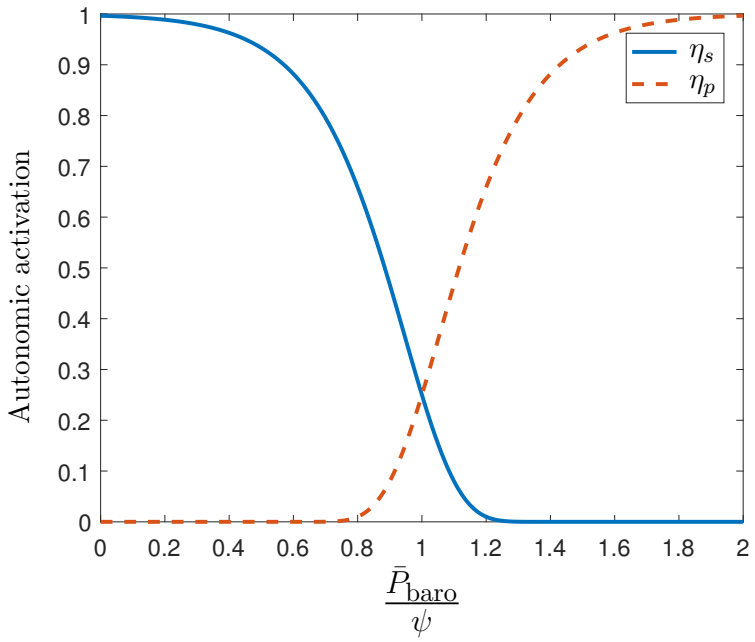

Figure 2.8: Illustration of autonomic activation functions. Asymmetry about target baroreceptor pressure follows [Kor71].

where the subscripts aa, lc, and rc denote the aortic arch, the left carotid, and the right carotid. By using pressure as the afferent signal in this manner, afferent nerve impulse dynamics are omitted for simplicity. The sympathetic and parasympathetic tones are then described as asymmetric sigmoidal functions of the baroreflex pressure $\bar{P}_{\text{baro}}$:

$$\begin{aligned} \eta_s &= \exp\left\{-a_\eta \exp\left[b_\eta\left(\frac{\bar{P}_{\text{baro}}}{\psi}-1\right)\right]\right\}, \\ \eta_p &= \exp\left\{-a_\eta \exp\left[-b_\eta\left(\frac{\bar{P}_{\text{baro}}}{\psi}-1\right)\right]\right\}. \end{aligned} \tag{2.48}$$

In Eq. (2.48), the constant ψ is the target mean pressure at the baroreceptors, a_η characterizes the firing rate at this pressure ($\bar{P}_{\text{baro}} = \psi$), and b_η characterizes sigmoidal steepness. This approach is based on experimental observations by Korner [Kor71], and is illustrated in Fig. 2.8. Importantly, the asymmetry about the target point allows a higher maximum heart rate while still preserving physiological levels of extreme bradycardia (i.e., low heart rates). These extrema, as well as the extrema for all other controlled parameters, are displayed in Table 2.1.

Table 2.1: Ranges of baroreflex-controlled parameters, normalized by parameter values at basal autonomic activation.

Parameter	Minimum	Maximum
$E_{\max,lv}/E_{\max,lv,0}$	0.8	1.6
$\mathrm{HR}/\mathrm{HR}_0$	0.25	2.4
R/R_0	0.6	2.2
C/C_0	0.7	1.1
$V_{un}/V_{un,0}$	0.85	1.05

Using the autonomic activations, controlled parameters are modulated with first-order ordinary differential equations. Since the heart is innervated by both the sympathetic and parasympathetic systems, changes to the heart rate ($\mathrm{HR} = 60 f_0$) are modeled using a linear combination of both tones:

$$\frac{d\mathrm{HR}}{dt} = \frac{1}{\tau_H}(-\mathrm{HR}(t) + \alpha_H \eta_s - \beta_H \eta_p + \gamma_H), \tag{2.49}$$

where τ_H is a time constant representing the delay between baroreceptor inputs and full effector organ activation; a complete listing of the time constants for all autonomic effectors is found in Table 2.2. To simulate alterations to cardiac contractility, the maximum elastance changes according to

$$\frac{dE_{\max}}{dt} = \frac{1}{\tau_E}(-E_{\max}(t) + \alpha_E \eta_s + \gamma_E). \tag{2.50}$$

From this equation, it can be seen that parasympathetic action on cardiac contractility is neglected. This assumption is based on the observations of Suga et al. [SSS73].

Since the veins are innervated by sympathetic nerves, and the work of Shoukas and Brunner [SB80] showed a variation in venous contractility with pressure in the carotid sinus, the compliance and unstressed volume in the distal peripheral and vena caval compartments change accordingly:

Table 2.2: Time constants for autonomic effector organs.

Time constant	Value (s)
τ_H	2
τ_E	2
τ_C	20
τ_V	20
τ_R	6

$$\frac{dC_i}{dt} = \frac{1}{\tau_C}(-C_i(t) - \alpha_C \eta_s + \gamma_C), \quad i = 4, 5, \mathrm{VC}, \tag{2.51}$$

$$\frac{dV_{un,i}}{dt} = \frac{1}{\tau_V}(-V_{un,i}(t) - \alpha_V \eta_s + \gamma_V), \quad i = 4, 5, \mathrm{VC}, \tag{2.52}$$

where inspection of Eqs. (2.51) and (2.52) shows that increased sympathetic activity tends to increase venous contractility (since η_s falls with increasing $\bar{P}_{\mathrm{baro}}$). Constriction or dilation of peripheral arteries occurs in a similar fashion, using

$$\frac{dR_i}{dt} = \frac{1}{\tau_R}(-R_i(t) + \alpha_R \eta_s + \gamma_R), \quad i = 2, 3. \tag{2.53}$$

The behavior modeled by Eq. (2.53) follows clinical observations [Gre86, SB80] that increasing $\bar{P}_{\mathrm{baro}}$ tends to reduce peripheral resistance. Also, the resistance in the first peripheral compartment R_1 is not regulated: it is fixed to the characteristic impedance $Z_0 = \rho c_0$ of the associated terminal artery in order to avoid non-physiological wave reflections [VT04]. Finally, although Eqs. (2.49) through (2.53) allow continuous parameter variation, only the peripheral quantities change in this manner. For the heart rate and maximum ventricular elastance, the calculated changes are applied only at the start of each cardiac cycle.

2.7 Tabulated parameter values by submodel

Table 2.3: Parameters for the one-dimensional arterial network.

Artery	ID	E (MPa)	A_0 (cm^2)	h (cm)	L (cm)
Ascending aorta	1	0.4	6.61	0.16	4.00
Aortic arch 1	2	0.4	3.94	0.13	2.00
Aortic arch 2	3	0.4	3.60	0.13	3.90
Left common carotid 1	4	0.4	0.43	0.06	8.90
Left Subclavian artery 1	5	0.4	0.55	0.07	3.40
Brachiocephalic artery	6	0.4	1.21	0.09	3.40
Thoracic aorta 1	7	0.4	3.14	0.12	5.20
Thoracic aorta 2	8	0.4	1.37	0.12	5.20
Thoracic aorta 3	9	0.4	1.37	0.12	5.20
Coeliac artery	10	0.4	0.48	0.06	1.00
Abdominal aorta 1	11	0.4	1.17	0.11	5.30
Splenic artery	12	0.4	0.25	0.05	6.30
Gastric artery	13	0.4	0.10	0.05	7.10
Hepatic artery	14	0.4	0.15	0.05	6.60
Superior mesenteric	15	0.4	0.58	0.07	5.90
Left Renal artery	16	0.4	0.21	0.05	3.20
Abdominal aorta 2	17	0.4	1.02	0.08	5.30
Right Renal artery	18	0.4	0.21	0.05	3.20
Abdominal aorta 3	19	0.4	1.02	0.08	5.30
Right Common iliac	20	0.4	0.85	0.08	5.80
Inferior mesenteric	21	0.4	0.08	0.04	5.00
Left Common iliac	22	0.4	0.85	0.08	5.80
Right Internal iliac	23	1.6	0.13	0.04	5.00
Right External iliac 1	24	0.4	0.26	0.06	8.30
Right External iliac 2	25	0.4	0.23	0.05	6.10
Right Femoral artery 1	26	0.8	0.18	0.05	12.70

Right Profundis artery	27	1.6	0.17	0.05	12.60
Right Femoral artery 2	28	0.8	0.18	0.05	12.70
Right Popliteal artery 1	29	0.8	0.13	0.05	9.40
Right Popliteal artery 2	30	0.4	0.13	0.05	9.40
Right Posteriortibial artery 1	31	1.6	0.10	0.05	16.10
Right Anteriortibial artery 1	32	1.6	0.05	0.04	2.50
Right Posteriortibial artery 2	33	1.6	0.10	0.05	16.10
Right Anteriortibial artery 2	34	1.6	0.03	0.02	15.00
Right Anteriortibial artery 3	35	1.6	0.03	0.02	15.00
Left External iliac 1	36	0.4	0.26	0.06	8.30
Left Internal iliac	37	1.6	0.13	0.04	5.00
Left External iliac 2	38	0.4	0.23	0.05	6.10
Left Profundis artery	39	1.6	0.17	0.05	12.60
Left Femoral artery 1	40	0.8	0.18	0.05	12.70
Left Femoral artery 2	41	0.8	0.18	0.05	12.70
Left Popliteal artery 1	42	0.8	0.13	0.05	9.40
Left Popliteal artery 2	43	0.4	0.13	0.05	9.40
Left Anteriortibial artery 1	44	1.6	0.05	0.04	2.50
Left Posteriortibial artery 1	45	1.6	0.10	0.05	16.10
Left Anteriortibial artery 2	46	1.6	0.03	0.02	15.00
Left Anteriortibial artery 3	47	1.6	0.03	0.02	15.00
Left Posteriortibial artery 2	48	1.6	0.10	0.05	16.10
Left common carotid 2	49	0.4	0.43	0.06	8.90
Left common carotid 3	50	0.4	0.43	0.06	3.10
Left Internal carotid 1	51	0.8	0.10	0.05	5.90
Left External carotid	52	0.8	0.07	0.04	11.80
Left Internal carotid 2	53	0.8	0.05	0.04	5.90
Left Cerebral artery	54	1.6	0.02	0.03	5.90
Left Internal carotid 3	55	1.6	0.02	0.03	5.90

Left Subclavian artery 2	56	0.4	0.50	0.07	6.80
Left Vertebral artery	57	0.8	0.11	0.05	14.80
Intercostal arteries	58	0.4	0.07	0.04	8.00
Left Axillary artery 1	59	0.4	0.41	0.06	6.10
Left Axillary artery 2	60	0.4	0.30	0.06	5.60
Left Brachial artery 1	61	0.4	0.25	0.06	6.30
Left Brachial artery 2	62	0.4	0.21	0.05	6.30
Left Brachial artery 3	63	0.4	0.20	0.05	6.30
Left Brachial artery 4	64	0.4	0.18	0.05	4.60
Left Radial artery 1	65	0.8	0.08	0.04	11.70
Left Ulnar artery 1	66	0.8	0.14	0.05	6.70
Left Radial artery 2	67	0.8	0.08	0.04	11.70
Left Interossea artery	68	1.6	0.03	0.03	7.90
Left Ulnar artery 2	69	0.8	0.11	0.05	8.50
Left Ulnar artery 3	70	0.8	0.11	0.05	8.50
Right Subclavian artery	71	0.4	0.50	0.07	6.80
Right common carotid 1	72	0.4	0.43	0.06	8.90
Right Vertebral artery	73	0.8	0.11	0.05	14.80
Right Axillary artery 1	74	0.4	0.41	0.06	6.10
Right Axillary artery 2	75	0.4	0.30	0.06	5.60
Right Brachial artery 1	76	0.4	0.25	0.06	6.30
Right Brachial artery 2	77	0.4	0.21	0.05	6.30
Right Brachial artery 3	78	0.4	0.20	0.05	6.30
Right Brachial artery 4	79	0.4	0.18	0.05	4.60
Right Ulnar artery 1	80	0.8	0.14	0.05	6.70
Right Radial artery 1	81	0.8	0.08	0.04	11.70
Right Ulnar artery 2	82	0.8	0.11	0.05	8.50
Right Interossea artery	83	1.6	0.08	0.03	7.90
Right Ulnar artery 3	84	0.8	0.11	0.05	8.50

Right Radial artery 2	85	0.8	0.08	0.04	11.70
Right common carotid 2	86	0.4	0.43	0.06	8.90
Right Internal carotid 1	87	0.8	0.10	0.05	5.90
Right External carotid	88	0.8	0.07	0.04	11.80
Right Internal carotid 2	89	0.8	0.05	0.04	5.90
Right Cerebral artery	90	1.6	0.02	0.03	5.90
Right Internal carotid 3	91	1.6	0.02	0.03	5.90

Table 2.4: Parameters for the cardiac/pulmonary submodel. Note that $E_{\text{lv,max}}$ and $E_{\text{rv,max}}$ are nominal values subject to change in the event of autoregulation.

Parameter	Value	Units
$V_{lv,un}$	10	mL
$V_{rv,un}$	10	mL
$V_{la,un}$	10	mL
$V_{ra,un}$	10	mL
$E_{\text{lv,min}}$	0.0283	mmHg/mL
$E_{\text{rv,min}}$	0.0283	mmHg/mL
$E_{\text{lv,max}}$	3	mmHg/mL
$E_{\text{rv,max}}$	0.4	mmHg/mL
E_{la}	0.130	mmHg/mL
E_{ra}	0.160	mmHg/mL
m_1	1.32	—
m_2	27.4	—
τ_1	$0.269t_h$	s
τ_2	$0.452t_h$	s
L_{la}	3×10^{-5}	mmHg·s^2/mL
L_{ra}	5×10^{-5}	mmHg·s^2/mL
R_{la}	3.6×10^{-3}	mmHg·s/mL
R_{ra}	4.85×10^{-3}	mmHg·s/mL

L_{rv}	2.16×10^{-4}	mmHg·s^2/mL
R_e	0.025	mmHg·s/mL
R_1	0.023	mmHg·s/mL
R_2	0.030	mmHg·s/mL
R_3	0.021	mmHg·s/mL
$R_{1,ve}$	0.010	mmHg·s/mL
$R_{2,ve}$	0.010	mmHg·s/mL
L_1	5×10^{-5}	mmHg·s^2/mL
$L_{2,ve}$	5×10^{-5}	mmHg·s^2/mL
C_1	2.222	mL/mmHg
C_2	1.481	mL/mmHg
C_3	1.778	mL/mmHg
$C_{1,ve}$	13.0	mL/mmHg
$C_{2,ve}$	74.0	mL/mmHg
$V_{1,un}$	50	mL
$V_{2,un}$	30	mL
$V_{3,un}$	53	mL
$V_{1,ve,un}$	75	mL
$V_{2,ve,un}$	75	mL

Table 2.5: Parameters for 0D terminal compartments and vena cavae. Unless otherwise noted, upper and lower terminal compartments share values.

Parameter	Value	Units
R_1	2.249	mmHg·s/mL
R_2	8.400	mmHg·s/mL
R_3	5.880	mmHg·s/mL
R_4	0.084	mmHg·s/mL
R_5	0.023	mmHg·s/mL
R_{svc}	0.030	mmHg·s/mL

R_{ivc}	0.013	mmHg·s/mL
$L_{5,\text{upper}}$	1.000×10^{-4}	mmHg·s^2/mL
$L_{5,\text{lower}}$	5.714×10^{-5}	mmHg·s^2/mL
L_{svc}	1.583×10^{-4}	mmHg·s^2/mL
L_{ivc}	6.786×10^{-5}	mmHg·s^2/mL
C_1	3.571×10^{-4}	mL/mmHg
C_2	0.059	mL/mmHg
C_3	0.065	mL/mmHg
C_4	0.473	mL/mmHg
C_5	2.507	mL/mmHg
C_{svc}	0.924	mL/mmHg
C_{ivc}	2.771	mL/mmHg
$V_{1,un}$	13.21	mL
$V_{2,un}$	13.21	mL
$V_{3,un}$	14.32	mL
$V_{4,un}$	21.29	mL
$V_{5,un}$	62.29	mL
$V_{svc,un}$	96.90	mL
$V_{ivc,un}$	96.90	mL

Table 2.6: Parameters for liver compartments.

Parameter	Value	Units
R_1	0.004	mmHg·s/mL
R_2	0.005	mmHg·s/mL
R_3	0.005	mmHg·s/mL
R_4	0.004	mmHg·s/mL
$L_{5,\text{upper}}$	5.00×10^{-5}	mmHg·s^2/mL
C_1	3.00	mL/mmHg
C_2	10.0	mL/mmHg

C_3	15.0	mL/mmHg
C_4	45.0	mL/mmHg
$V_{1,un}$	50.0	mL
$V_{2,un}$	30.0	mL
$V_{3,un}$	53.0	mL
$V_{4,un}$	75.0	mL

Table 2.7: Parameters for baroreflex submodel.

Parameter	Value	Units
a_η	ln(0.25)	—
b_η	6	—
ψ	95	mmHg
α_H	2.1563	1/s
$\alpha_{E\mathrm{lv}}$	1.60	mmHg/mL
$\alpha_{E\mathrm{rv}}$	0.288	mmHg/mL
α_{R2}	13.44	mmHg·s/mL
α_{R3}	9.41	mmHg·s/mL
α_{C4}	0.189	mL/mmHg
α_{C5}	1.003	mL/mmHg
α_{V4}	4.257	mL
α_{V5}	12.459	mL
β_H	0.5313	1/s
γ_H	0.8438	1/s
$\gamma_{E\mathrm{lv}}$	1.6	mmHg/mL
$\gamma_{E\mathrm{rv}}$	0.288	mmHg/mL
γ_{R2}	5.040	mmHg·s/mL
γ_{R3}	3.528	mmHg·s/mL
γ_{C4}	0.520	mL/mmHg
γ_{C5}	2.757	mL/mmHg

γ_{V4}	22.35	mL
γ_{V5}	65.41	mL

CHAPTER 3

Full-Scale Model Results and Analysis

3.1 Validation under resting conditions

As validation, selected results from the periodic steady state under resting conditions (i.e., with basal levels of autonomic activation) are presented. Table 3.1 compares regional blood flow predicted by the model to experimental data. This comparison shows that the 1D model is able to accurately capture the localized distribution of cardiac output. Fig. 3.1 displays the spatial and temporal evolution of the pressure waveform as it leaves the heart and travels into the left leg. The amplitude of the pressure wave first decreases, then increases with distance from the heart, as measured by the widening gap between systolic and diastolic pressures. The increase in systolic pressure corresponds to the gradual narrowing of the aorta as it descends the abdomen, with the peak occuring near the aortic bifurcation. This behavior can be attributed to an increase in reflectivity (or, equivalently, in vascular resistance [WP04]). Owing to this increased reflectivity, a spatial steepening of the dicrotic notch (the sudden jump in pressure coincident with the closure of the aortic valve) is also observed. Both of these trends are well-established in the literature [APP08, Avo80, BTF12, FLT06, Goh07, LTH09a, LTH09b, MT14, SFP03, SYR92, WP04]. As a final note, intermittent spatial discontinuities in pressure occur because stagnation pressure, rather than static pressure, is conserved at arterial junctions.

Fig. 3.2 illustrates changes in the flow rate waveform along the same path taken in Fig. 3.1, with experimental averages from Reymond et al. [RMP09] provided for comparison. The predicted flows roughly match the measured data in magnitude, though a small discrepancy exists in phase. Still, as expected from arterial branching, both overall blood volume

Table 3.1: Comparison of predicted regional blood flow with experimental data.

Parameter (units)	Value (mean ± SE)
Cerebral (mL/s)	9.1 (10.3 ± 2.1 [OSK96])
Upper limb (mL/min)	413 (350 ± 40 [VS02])
Lower limb (mL/min)	425 (440 ± 23 [SDM01])

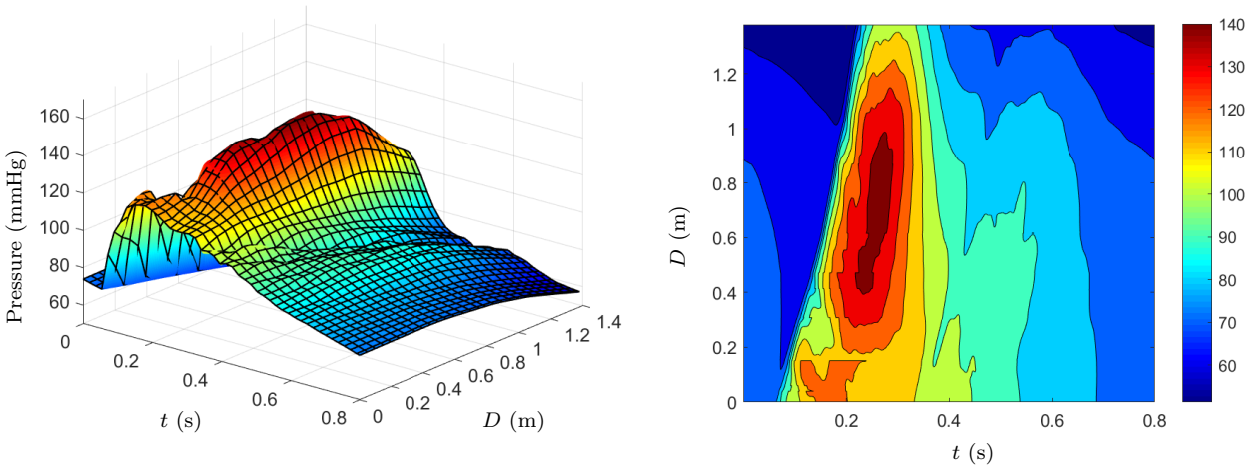

Figure 3.1: Spatio-temporal evolution of the pressure waveform traveling from the aortic root ($D = 0$ cm) to the left anteriortibial artery under resting conditions.

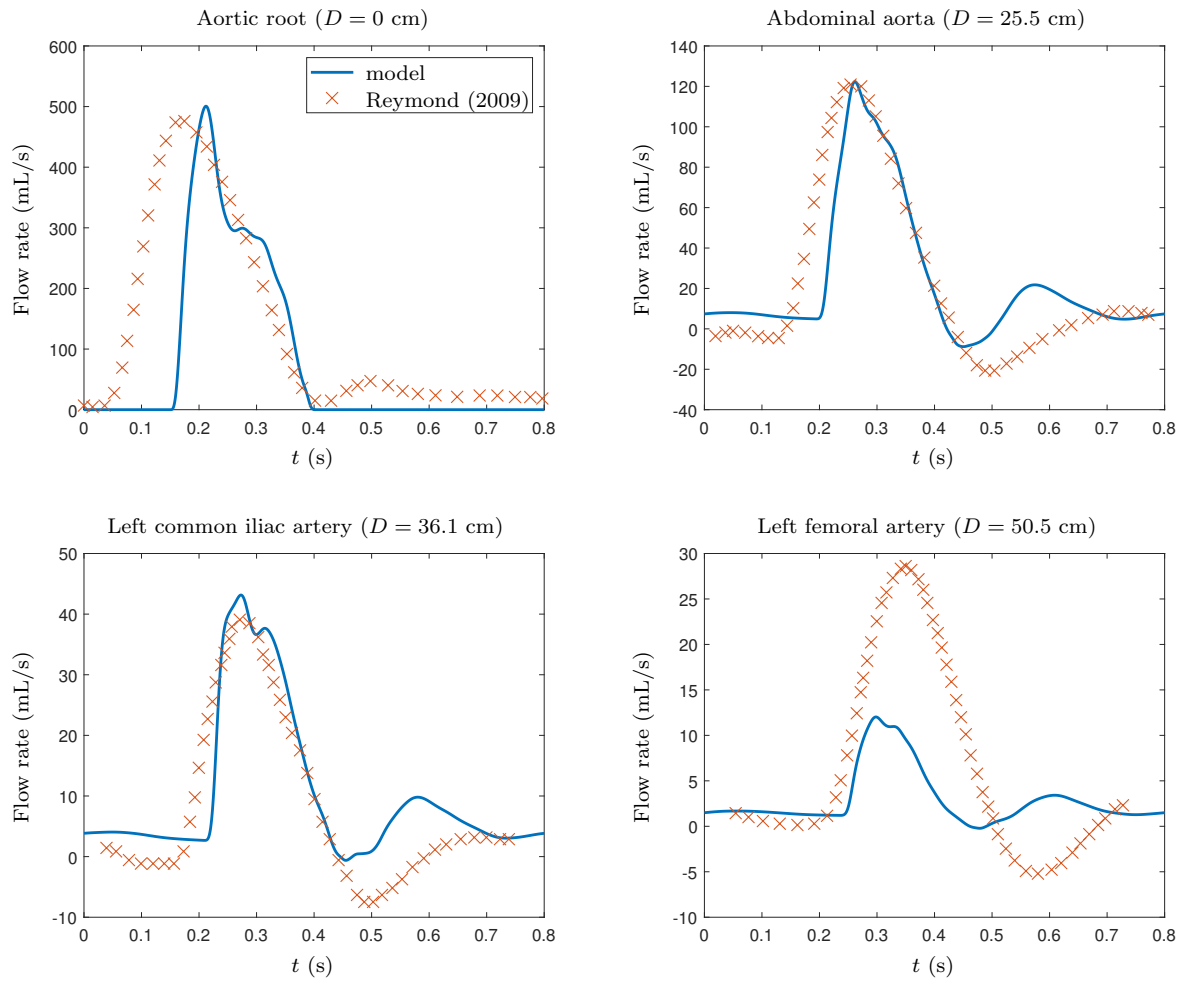

Figure 3.2: Flow rate measured under resting conditions at varying distances D from the aortic root.

transport and peak flow rate decrease towards the periphery. Also, as observed in both the pressure waveform and literature data [Avo80, BTF12, LTH09a, LTH09b, MT14, VT04], a spatial increase in reflectivity is evidenced by the emergence of retrograde and secondary antegrade flow waves.

To investigate the model's global character, there are several worthwhile clinical parameters of interest that involve the dynamics of the entire cardiovascular system. For instance, both maximum (systolic) and minimum (diastolic) blood pressure are often cited as primary indicators of overall cardiovascular health. Additionally, the interaction between ventricles and vasculature is implicit in end-diastolic and end-systolic ventricular volumes (EDV and

ESV, respectively): EDV measures venous return, while the difference the two (known as "stroke volume," SV = EDV − ESV quantifies the heart's ability to pump blood against the resistance posed by the vasculature. Ejection fraction (EF) is a non-dimensional measure of the latter, defined as the percent of end-diastolic ventricular blood volume sent into the circulatory systems:

$$\mathrm{EF} = \frac{\mathrm{EDV} - \mathrm{ESV}}{\mathrm{EDV}} \times 100\% = \frac{\mathrm{SV}}{\mathrm{EDV}} \times 100\%. \tag{3.1}$$

To give a sense of the heart's ability to deliver blood adequately over time, stroke volume is usually multiplied by heart rate (HR) to produce a quantity called "cardiac output":

$$\mathrm{CO} = \mathrm{SV} \times \mathrm{HR} \tag{3.2}$$

Knowing cardiac output, overall systemic vascular resistance (SVR) is computed in a fluid-dynamical analogy to Ohm's law between the endpoints of the systemic vasculature:

$$\mathrm{SVR} = \frac{\bar{P}_{ao} - \bar{P}_{ra}}{\mathrm{CO}}, \tag{3.3}$$

where $\bar{P}_{ao}$ and $\bar{P}_{ra}$ are average aortic and right atrial pressure over a single cardiac cycle. Finally, the pressure pulse wave velocity (PWV) can be used as a measure of arterial wall stiffness (e.g., patients with atherosclerosis often exhibit abnormally high PWV [YTT02]). For each of the parameters discussed above, the predicted value from the model is reported alongside *in vivo* comparisons in Table 3.2. All parameters fall within normal ranges except right ventricular end-diastolic volume, which is marginally hypovolemic (~3% lower than the experimentally-reported minimum).

3.2 Response to global sympathetic stimulation

In healthy subjects, global sympathetic stimulation is rare, as the sympathetic nervous system is known to activate effector organs differentially based on input stimuli [BGC84, Dam94,

Table 3.2: Clinical parameters of interest under resting conditions with empirically-measured ranges. SBP: systolic blood pressure; DBP: diastolic blood pressure; LV/RV EDV/RSV: left/right ventricular end-diastolic/end-systolic volume; LV/RV EF: left/right ventricular ejection fraction; HR: heart rate; CO: cardiac output; SVR: systemic vascular resistance; PWV: pulse wave velocity. *PWV estimated by following the foot of the pressure pulse from the aortic inlet to the outlet of the left posterior tibial artery.

Parameter (units)	Value (range)
SBP (mmHg)	122 (114 - 132 [CAH09])
DBP (mmHg)	71 (67 - 81 [CAH09])
LV EDV (mL)	116 (115 - 219 [CAH09])
LV ESV (mL)	49 (32 - 96 [CAH09])
LV EF (%)	58 (51 - 81 [CAH09])
RV EDV (mL)	124 (127 - 227 [MPK06])
RV ESV (mL)	55 (38 - 98 [MPK06])
RV EF (%)	53 (48 - 74 [MPK06])
HR (bpm)	75 (50 - 100 [OOC86])
CO (L/min)	5.1 (4.0 - 9.0 [RGB84])
SVR (MPa·s/m^3)	146 (70 - 160 [KCG08])
PWV (cm/s)	1170* (1100 - 1500 [YTT02])

FRH11, GJP95, GTA82, JM92, MFH10, Mor01]. However, chronically heightened levels of sympathetic nervous activity, possibly through a feedback loop of neurotransmitter imbalances [BAP01, BHP69, YML84] and over-active renin-angiontensin and/or sympathoadrenal systems [Man03], leads to 'neurogenic' hypertension. To model this pathological state, the cardiovascular system was subjected to varying levels of sustained, concurrent sympathetic stimulation and parasympathetic inhibition (i.e., the values of n_s and n_p in Eq. (2.48) were set according to a constant, arbitrary pressure, rather than the baroreflex pressure).

The effects of this stimulation on various hemodynamic parameters are displayed in Fig. 3.3. According to established physiological guidelines [CBB03], the systolic and diastolic limits for hypertension not constituting a medical emergency are 179 and 109 mmHg, respectively. As seen in the figure, these limits correspond to a sympathetic activation of roughly 0.6; this boundary is demarcated by the dashed lines on each plot. Increased sympathetic activity results not only in the aforementioned hypertension, but also in tachycardia (elevated heart rate), as expected from other baroreflex modeling efforts [Dan98, BTF12]. However, the asymmetric activation function developed in this study permits a higher maximum heart rate, reaching approximately 180 beats per minute. Though this test was intended to model hypertension, this maximum is in line with experimental observations during maximal exercise in healthy subjects [HES70, CST87].

Interestingly, Fig. 3.3 also shows that cardiac output exhibits nonlinearity in its response to autonomic activity. Prior to the limit for hypertensive emergencies, cardiac output increases, indicating that the induced tachycardia and positive inotropy (as measured by increasing maximum ventricular elastance) overcomes the reduction in stroke volume produced by a combination of shorter systolic duration and increased systemic vascular resistance. Indeed, the increase in elastance supports experimental observations of cardiac hypertrophy (abnormal muscle growth) and wall thickening in response to the augmented afterload (i.e., SVR) exhibited by hypertensive subjects [MH03]. Furthermore, as displayed in Table 3.3, the observed elevations in cardiac output and systemic vascular resistance exhibit close agreement with experimental measurements of patients with hypertension induced by pheochromocytoma (a tumor in the adrenal glands that secretes high levels of

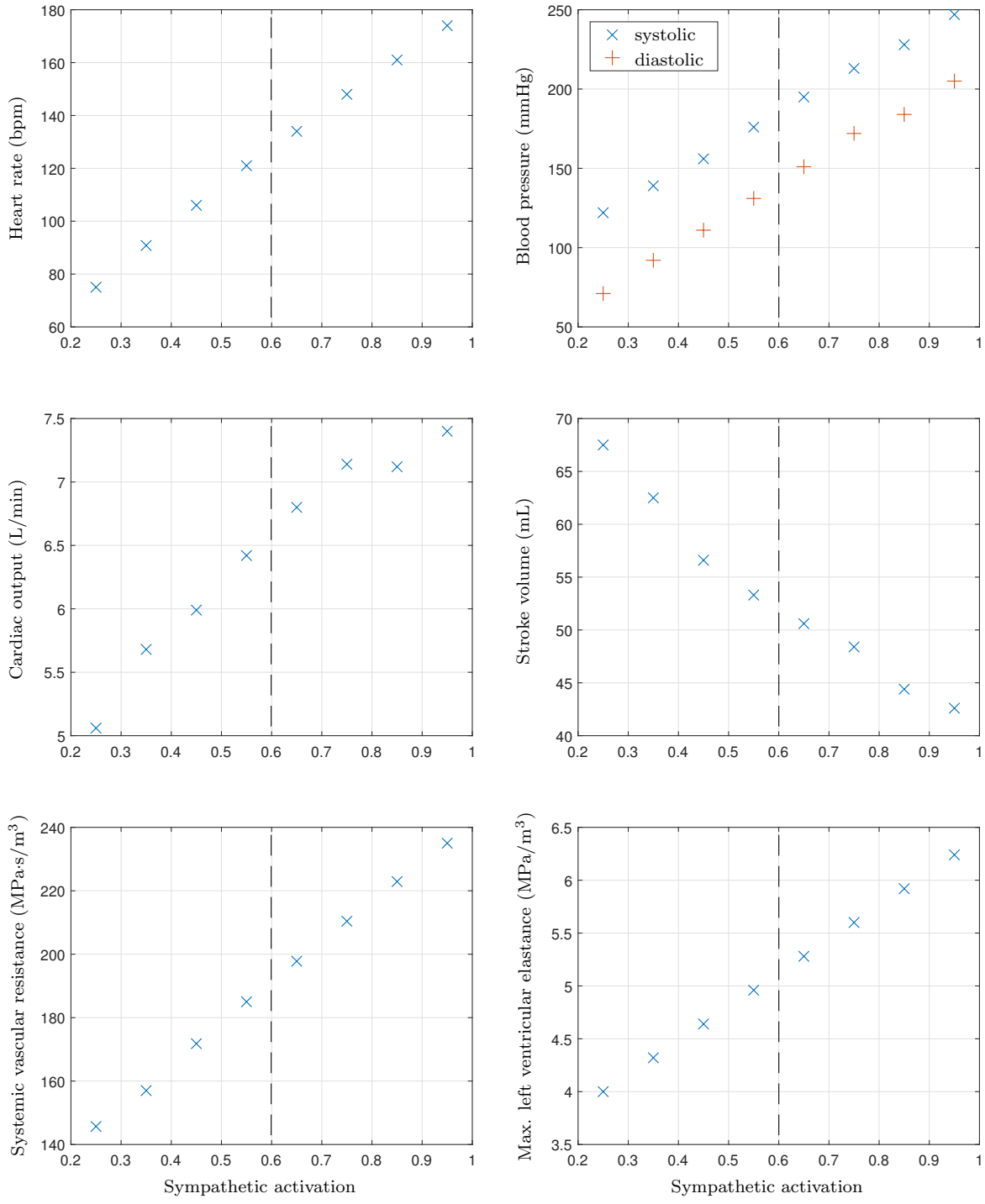

Figure 3.3: Global clinical parameters of interest at equilibria achieved under varying levels of sympathetic stimulation/parasympathetic inhibition. Dashed line represents limit for non-emergency hypertension (systolic BP $\leq$ 179 mmHg, diastolic BP $\leq$ 109 mmHg).

Table 3.3: Comparison of global clinical parameters under sympathetic stimulation/parasympathetic inhibition against literature data from patients with pheochromocytoma (matched by mean arterial pressure at 134 mmHg).

Parameter (units)	Current study	Frohlich (1969) [FTD69]
CO (L/min)	6.16	6.18
SVR (MPa·s/m^3)	177	179
HR	112	76
SV	55.3	82.7

norepinephrine) [FTD69]. Table 3.3 also shows some discrepancy in heart rate and stroke volume; this difference occurs because the baroreflex model is intended to capture short-term control mechanisms, and hence does not include the long-term baroreceptor resetting [Dan98] that would occur in chronic hypertension.

Moving towards maximal levels of sympathetic activity, cardiac output reaches a plateau, while both blood pressure and systemic vascular resistance continue to increase. This finding is in agreement with an experimental study on the pressor response to reduced carotid baroreceptor input [CAA00], as it concluded that this response is mediated by peripheral vasoconstriction, rather than augmented cardiac output. It is also worth noting that the highest level of sympathetic stimulation exhibits a small uptick in cardiac output, which can be explained by observing that stroke volume is also beginning to plateau, whereas heart rate is still increasing linearly. This trend is in line with experimental work [MDR82] showing that the decline in stroke volume slows with increasing heart rate.

Focusing on local hemodynamic alterations, Fig. 3.4 shows pressure waves in the aorta, limbs, and head under varying levels of stimulation. As stimulation increases, we observe a global delay in the beginning of the pressure pulse relative to the heart period, as well as a narrowing of the pressure pulse. Both of these changes are consistent with the increased vascular resistance noted in Fig. 3.3, as the left ventricle must achieve a higher pressure to initiate ejection. In contrast to these global similarities, we see that the upper limbs and head

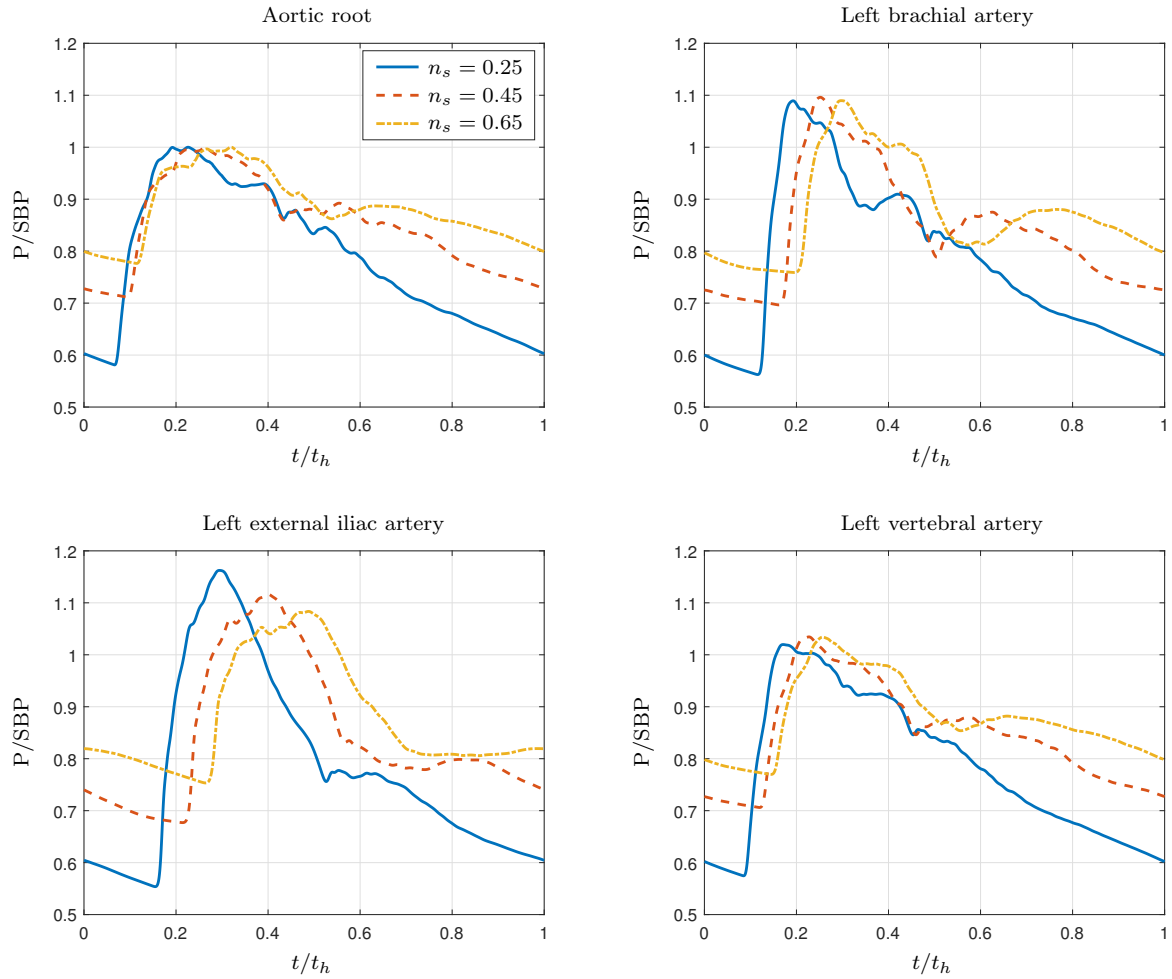

Figure 3.4: Pressure measured across the 1D network at varying levels of sympathetic stimulation/parasympathetic inhibition (note $n_s = 0.25$ is the baseline case).

maintain their relative maximum pressure under stimulation, whereas the maximum pressure falls in the lower limbs. This phenomenon could be a consequence of wave interference: owing to the increased time delay for the pressure pulse in the legs, the valley observed after the primary pressure pulse in the upper extremities might instead interfere destructively with the pulse in the lower extremities. Such localized alterations to arterial waves are not observable in lumped-parameter models of the systemic circulation, thus illustrating an advantage of one-dimensional arterial network models in studying cardiovascular control mechanisms.

3.3 Response to 10% acute hemorrhage

To simulate a severe hemorrhage, the junction between the left femoral artery and its children were replaced with zero-pressure (i.e., non-reflective) outflow boundary conditions. After 10% total blood volume loss (roughly 500 mL), tourniquet application around the upper thigh was modeled by reducing the reference area A_0 to 1% of its baseline value and doubling the stiffness parameter β in both the upper femoral and profundis arteries. These parameter changes occurred over a ten-second period, and the system was then allowed to reach a new equilibrium state.

Sympathetic activity during the hemorrhagic episode is displayed alongside autonomic effector activity and baroreceptor pressure in Fig. 3.5. The evolutions displayed succinctly illustrate the interplay between the baroreceptors and effector organs, as well as the dynamics produced by the organs' varying time delays. Initially, the acute volume loss and associated fall in baroreceptor pressure results in rapid sympathetic excitation, promoting vasoconstriction, positive inotropy, and tachycardia. The first valley observed in baroreceptor pressure indicates that the relatively faster responses of peripheral resistance and ventricular elastance adequately compensate for blood loss for a short time. However, over a longer time horizon, the slower response of the venous reservoir causes a net depletion of blood from the arterial vasculature, and baroreceptor pressure falls until the tourniquet is applied. Shortly after application begins, minimum pressure and maximum sympathetic activation occur simultaneously as a consequence of the algebraic relation between the two

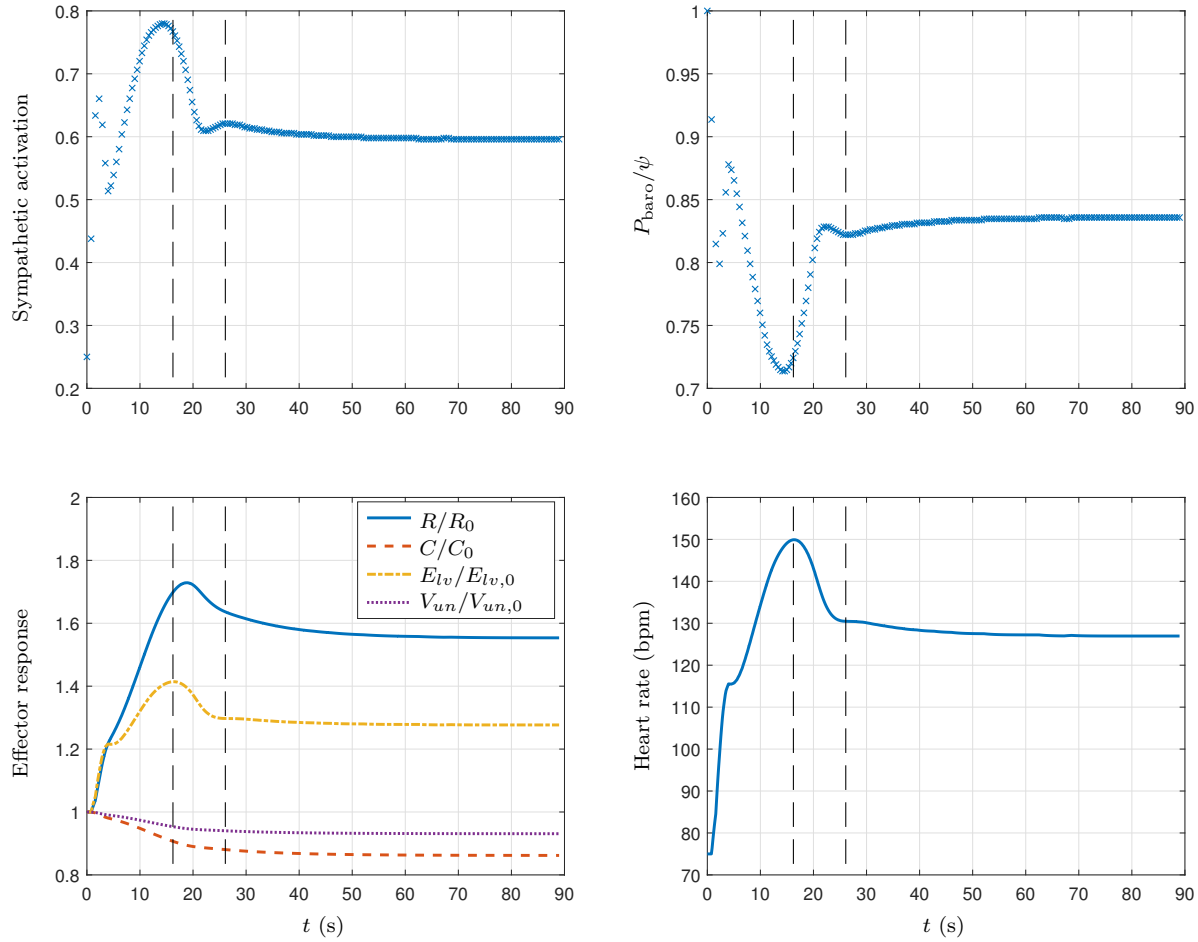

Figure 3.5: Sympathetic activation, baroreceptor pressure, and effector organ responses during acute 10% hemorrhage. Pressure and effector responses (excluding heart rate) normalized by basal values. Region between dashed lines indicates period of tourniquet application.

(see Eq. (2.48)). As application continues, ventricular elastance, peripheral resistance, and heart rate peak and decline in order of increasing effector time delay (see Table 2.2). At the end of application, the venous reservoir stabilizes; this stabilization, coupled with continued decreases in cardiac action and systemic vascular resistance, results in a final lowering of the baroreceptor pressure to its new equilibrium value.

During hemorrhage, an especially important action of the baroreflex is to mobilize blood from the venous reservoir to ensure adequate perfusion of vital organs. Fig. 3.6 shows this action directly, as blood volume shifts from the systemic veins and into the systemic capillary beds. Moreover, the use of a one-dimensional network allows for observation of the impact of tourniquet application on regional blood distribution, as the increased resistance imposed by the tourniquet moves blood contralaterally and superiorly away from the injury site.

Besides shifting blood volume, the baroreflex maintains perfusion through augmented arterial pressure and cardiac performance. These actions are displayed in Fig. 3.7, which contrasts aortic pressure and cardiac pressure-volume loops obtained from the hemorrhagic episode with and without an intact baroreflex. While the aortic pressure record shows that the tourniquet is able to stabilize arterial pressure without the baroreflex, the absence of heightened vasomotor tone leads to severe hypotension. As observed in other studies [Dan98, BTF12], the baroreflex is seen to prevent appreciable change in diastolic blood pressure between the healthy equilibrium (71 mmHg) and that achieved after hemorrhage. Regarding the area contained in the pressure-volume loops, both hemorrhage cases show a markedly decreased mechanical work per beat compared to the healthy case. Interestingly, the denervated case does not show a significant decrease in its work regime relative to the intact case, whereas the augmented systolic pressure in the intact case is countered by shorter systolic duration and impaired diastolic refilling, the latter of which is known to occur with elevated heart rates [TA90]. However, owing to the aforementioned tachycardia, cardiac output is significantly higher in the intact case (2.96 L/min versus 2.26 L/min).

As validation of the baroreflex model developed in this work for cardiovascular response to hemorrhage, Table 3.4 compares clinical parameters obtained in the new equilibrium state after hemorrhage against previous numerical work [BTF12] and experimental studies of hem-

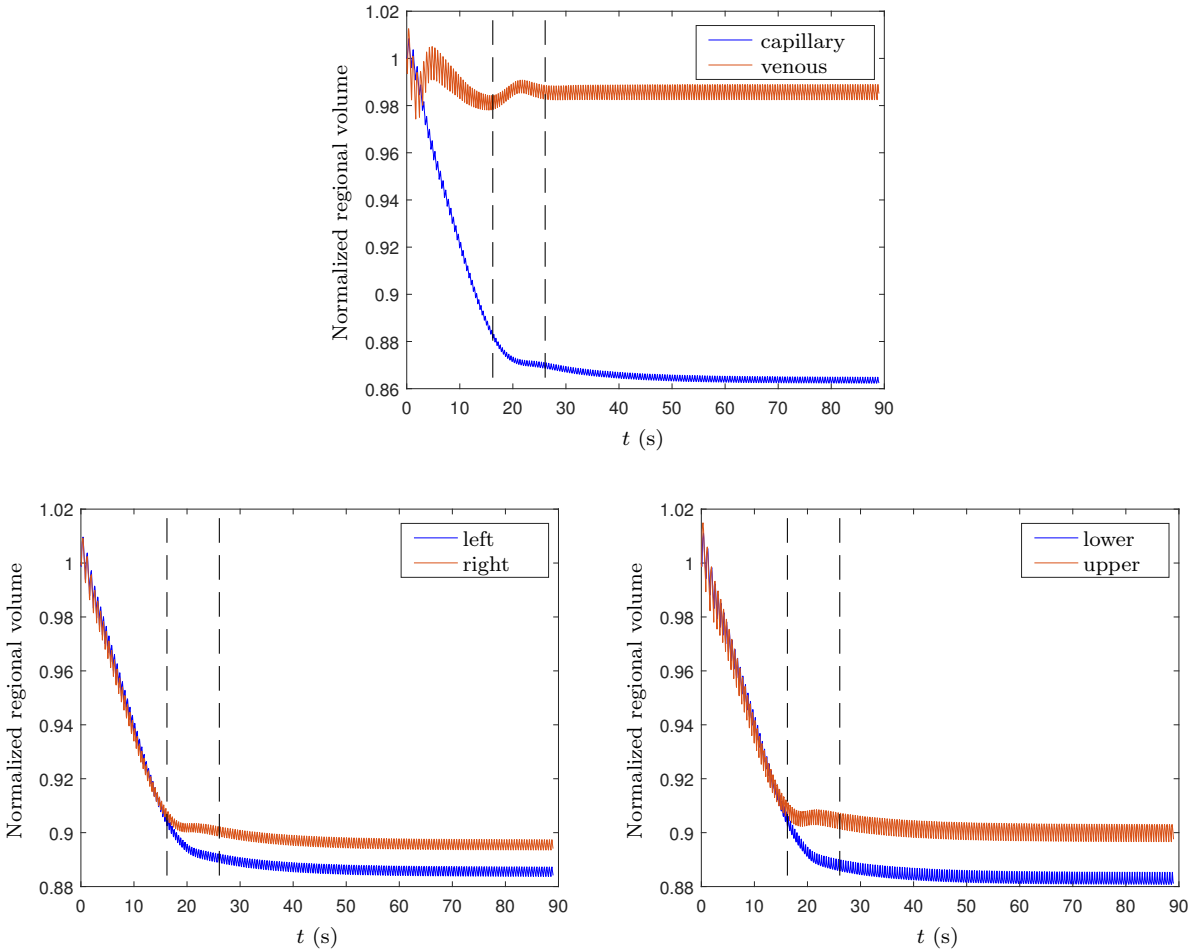

Figure 3.6: Shift in blood distribution during an acute 10% hemorrhage. Volumes normalized by volume at end-diastole just before hemorrhage (i.e., the healthy condition). Region between dashed lines indicates period of tourniquet application.

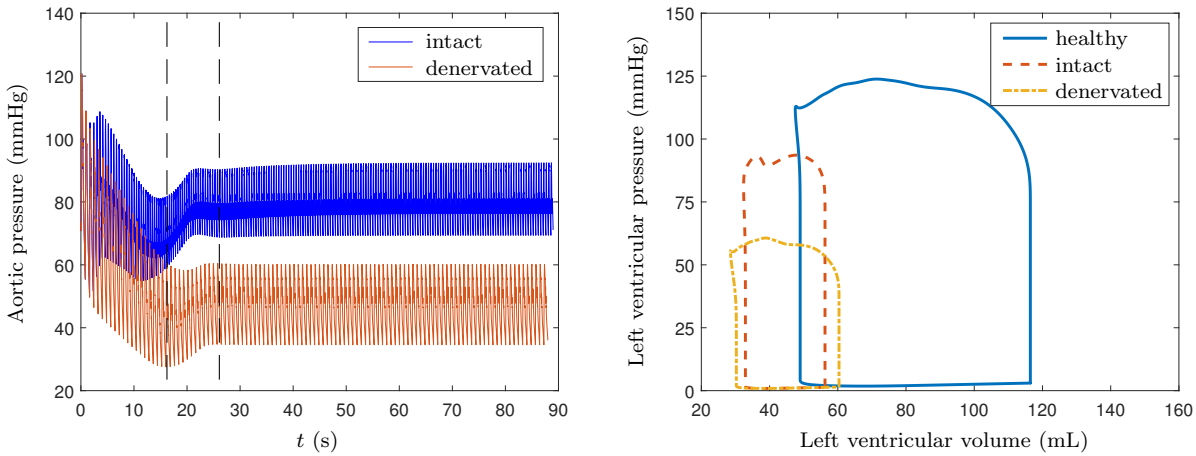

Figure 3.7: Comparison of aortic pressure and equilibrium cardiac pressure-volume loops with and without intact baroreflex during 10% hemorrhage. Region between dashed lines indicates period of tourniquet application.

orrhage in sheep [FRH11] and dogs [KSS70]. The predicted changes in mean arterial pressure and left ventricular pressure closely match the experimental work, while heart rate, cardiac output, and vascular resistance/conductance fall only slightly outside of the experimental range of variation.

3.4 Parameter Sensitivity Analysis

3.4.1 The Latin-Hypercube/one-at-a-time method

In the previous section, it was demonstrated that the full-scale cardiovascular model's parameters could be tuned to produce reasonable results for a generic cohort of patients. However, performing this tuning required end-user expertise and a significant time investment. While an automated parameter tuning framework would therefore be useful, it is unlikely that such a method would be able to accurately tune all of the parameters for this model: there are several hundred parameters, but only roughly ten clinical measurements that could be taken to serve as constraints, leading to a severely underdetermined estimation problem. Furthermore, it is probable that certain parameters exert greater influence on both localized

Table 3.4: Percentage changes (relative to healthy value) during hemorrhage compared against numerical [BTF12] and experimental [FRH11, KSS70] data from the literature.

Parameter	Blanco et al. [BTF12]	Frithiof et al. [FRH11]	Kumada et al. [KSS70]	Current study
MAP	—	-14 ± 2	-12 ± 2	-12
HR	$+30$	$+56 \pm 6$	$+53 \pm 15$	$+69$
CO	-20	-34 ± 2	-32 ± 3	-41
LVP	-18	-23 ± 7	—	-24
SVR	—	—	$+32 \pm 8$	$+46$
SVC	—	-19 ± 6	—	-31

measurements and on global model character, and should thus be prioritized in an estimation procedure.

To address the issues outlined above, the full-scale model can be further examined through a process known as "sensitivity analysis." Generically, this process requires a vector of relevant measurements $\boldsymbol{y}$ and a vector of parameters $\boldsymbol{\theta}$. Given some baseline for these two vectors, we then change $\boldsymbol{\theta}$ slightly, observe the resulting displacement in $\boldsymbol{y}$, and use the differences to numerically approximate the sensitivity Jacobian $\frac{d\boldsymbol{y}}{d\boldsymbol{\theta}}$. If this Jacobian is appropriately normalized, we can then compare its elements to determine the parameters towards which our measurements are most sensitive (larger magnitudes indicating larger sensitivity).

While this approach is conceptually straightforward, there is no guarantee that the relationship between any particular pair of elements within $\boldsymbol{y}$ and $\boldsymbol{\theta}$ is linear. As such, our sampling point for a baseline value of $\boldsymbol{\theta}$ can introduce unwanted bias into our sensitivity matrix: parameters that exhibit strong sensitivity in one region of parameter space might become weak in another region, and vice-versa. To make the distinction between parameters that are only "locally" sensitive (i.e., in one region of parameter space) and those that are "globally" sensitive (i.e., regardless of sampling point), we can employ a hybrid sampling method known as Latin Hypercube/one-at-a-time (LH-OAT) [vMG06]. This method begins

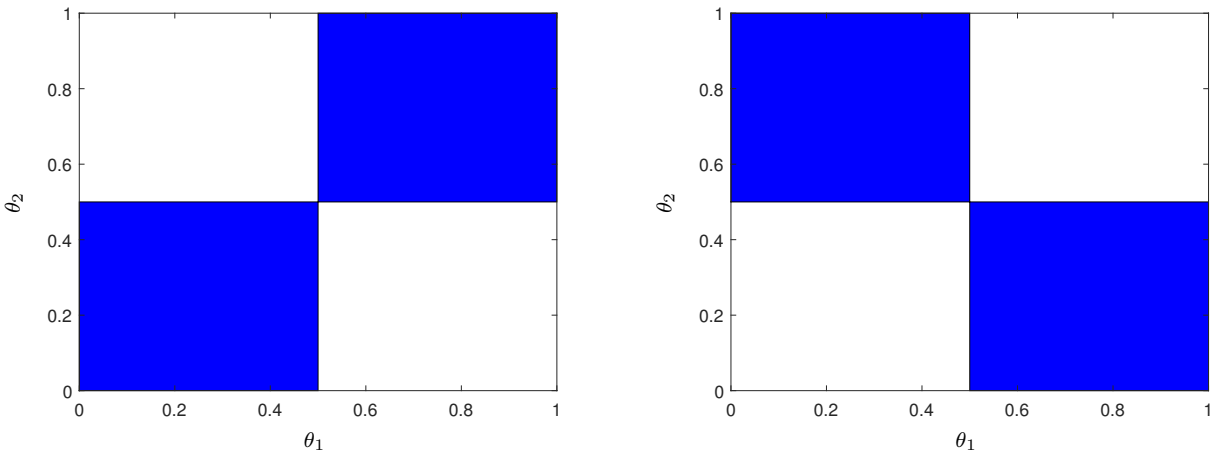

Figure 3.8: Example of valid Latin Hypercube sampling regions (in blue) for a 2D parameter space.

by dividing the parameter space into n equally-wide strata and taking n samples such that the "hyperrows" and "hypercolumns" extending from one sampling region do not intersect any others. As a simple example, if we had only two parameters that varied between 0 and 1, and if we divided each of these ranges into two strata, the only valid sampling regions we could choose are displayed in Fig. 3.8 as diagonal, blue areas. This submethod is known as Latin Hypercube sampling, and allows for efficient cover of the entire parameter space. For every i^{th} Latin Hypercube point, we then vary parameters one-at-a-time to construct $(\frac{d\boldsymbol{y}}{d\boldsymbol{\theta}})_i$. Once all of these senstivity Jacobians have been computed and normalized, we can analyze them to distinguish between locally and globally sensitive parameters: the former will have relatively large values for a limited subset of i, while the latter will be significant for all (or nearly all) n Jacobians.

3.4.2 LH-OAT analysis of the full-scale cardiovascular model

To apply the LH-OAT method to the full-scale cardiovascular model, the range for each parameter was broken into four strata, leading to four Latin Hypercube points. A simulation was first run to steady-state from each of these four points to serve as a baseline. Then, for each Latin Hypercube baseline sample, parameters were scaled randomly up or down by

5% in a one-at-a-time fashion, and a new simulation was run to steady-state. By comparing typical clinical measurements between the baseline point and each altered point, ($\frac{d\boldsymbol{y}}{d\boldsymbol{\theta}}$) was constructed for each Latin Hypercube sample.

The subplots in Fig. 3.9 break out the normalized sensitivity for the suite of clinical measurements considered in this study (i.e., each subplot graphically represents a row of $\frac{d\boldsymbol{y}}{d\boldsymbol{\theta}}$ for all Latin Hypercube points). For completeness, the scaling indices are tabulated with their descriptions in Table 3.5. From these plots, the following indices exhibit high sensitivity across all measurements and sample points: 11, 15, 16, 24, and 40. In order, these indices correspond to C_5 and $V_{un,4,5}$ for the systemic circulation, C_4 for the liver, and $C_{v,2}$ for the pulmonary circulation. In other words, this analysis suggests that the compliance of the large veins, together with the size of the systemic venous reservoir, possess an outsized impact on the overall character of the cardiovascular model. The model is therefore globally sensitive to these parameters, so their proper tuning should be prioritized in all cases.

Turning to local sensitivity, it is clear that for blood pressure and peak aortic flow, the first two scalings are important. These scalings correspond to β and A_0 for the major systemic arteries, so it is perhaps not surprising that they strongly affect pressure measurements: from Eq. (2.12), we see that arterial pressure is proportional to β and offset by A_0. Furthermore, the pressure-driven nature of blood flow explains the sensitivity of peak aortic flow to these parameters, since they effectively control the peak pressure of the major arteries (i.e., they serve as a 1D analog to compartmental compliance). Thus, in cases where accurate prediction of systemic pressure and peak flow is desirable, priority should be given to tuning arterial stiffness and/or unstressed lumen area.

Table 3.5: Listing of parameter scalings associated with indices in Fig. 3.9.

Index	Parameter
1	β
2	A_0
3	R_2, systemic
4	R_3, systemic

5	R_4, systemic
6	R_5, systemic
7	C_1, systemic
8	C_2, systemic
9	C_3, systemic
10	C_4, systemic
11	C_5, systemic
12	$V_{un,1}$, systemic
13	$V_{un,2}$, systemic
14	$V_{un,3}$, systemic
15	$V_{un,4}$, systemic
16	$V_{un,5}$, systemic
17	R_1, liver
18	R_2, liver
19	R_3, liver
20	R_4, liver
21	C_1, liver
22	C_2, liver
23	C_3, liver
24	C_4, liver
25	$V_{un,1}$, liver
26	$V_{un,2}$, liver
27	$V_{un,3}$, liver
28	$V_{un,4}$, liver
29	L_4, liver
30	R_p, lungs
31	$R_{a,1}$, lungs
32	$R_{a,2}$, lungs
33	$R_{a,3}$, lungs

34	$R_{v,1}$, lungs
35	$R_{v,2}$, lungs
36	$C_{a,1}$, lungs
37	$C_{a,2}$, lungs
38	$C_{a,3}$, lungs
39	$C_{v,1}$, lungs
40	$C_{v,2}$, lungs
41	$V_{un,1}$, lungs
42	$V_{un,2}$, lungs
43	$V_{un,3}$, lungs
44	$V_{un,4}$, lungs
45	$V_{un,5}$, lungs
46	L_a, lungs
47	L_v, lungs
48	lower/upper body flow split
49	venous resistance fraction
50	venous inductance fraction
51	venous capacitance fraction
52	venous V_un fraction
53	m_1, elastance function
54	m_2, elastance function
55	τ_1, elastance function
56	τ_2, elastance function
57	$E_{\max,lv}$, elastance function
58	$E_{\max,lv}$, elastance function
59	$V_{un,lv}$, heart
60	$V_{un,rv}$, heart
61	$V_{un,la}$, heart
62	R_{la}, heart

63	L_{la}, heart
64	E_{la}, heart
65	$V_{un,ra}$, heart
66	R_{ra}, heart
67	L_{ra}, heart
68	E_{ra}, heart
69	L_{rv}, heart
70	L_5, systemic

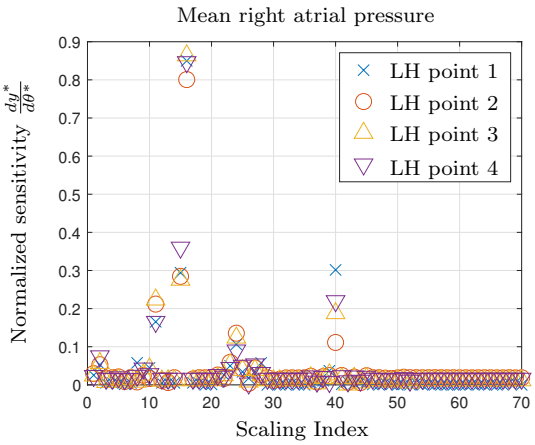
Mean right atrial pressure
LH point 1
LH point 2
LH point 3
LH point 4
Normalized sensitivity $\frac{dy^*}{d\theta^*}$
Scaling Index

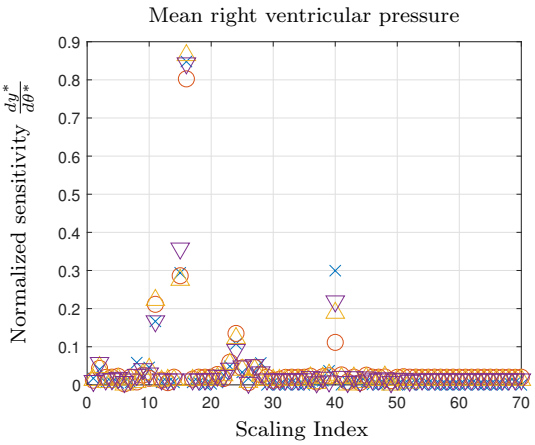
Mean right ventricular pressure
Normalized sensitivity $\frac{dy^*}{d\theta^*}$
Scaling Index

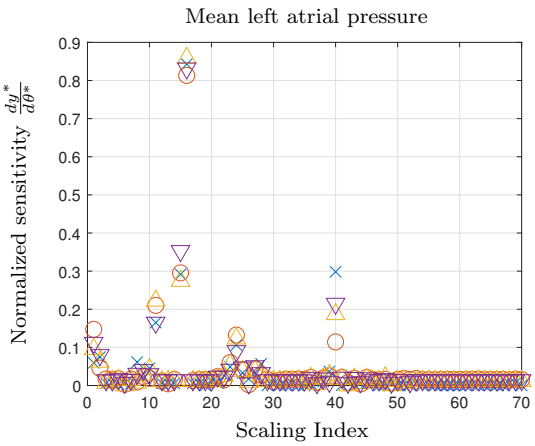
Mean left atrial pressure
Normalized sensitivity $\frac{dy^*}{d\theta^*}$
Scaling Index

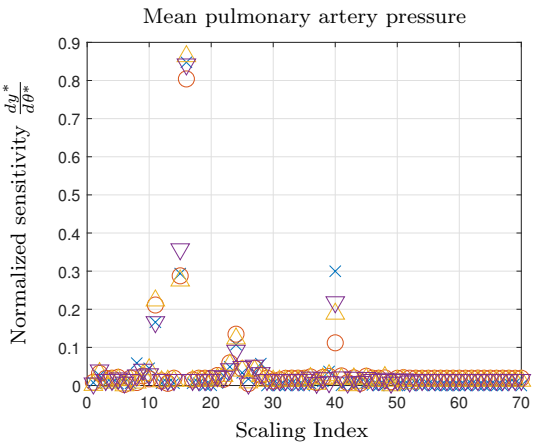
Mean pulmonary artery pressure
Normalized sensitivity $\frac{dy^*}{d\theta^*}$
Scaling Index

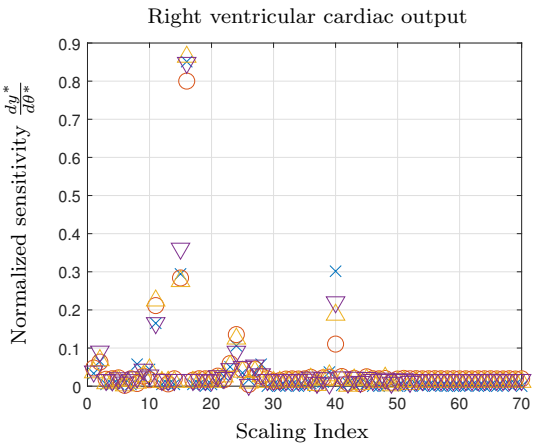
Right ventricular cardiac output
Normalized sensitivity $\frac{dy^*}{d\theta^*}$
Scaling Index

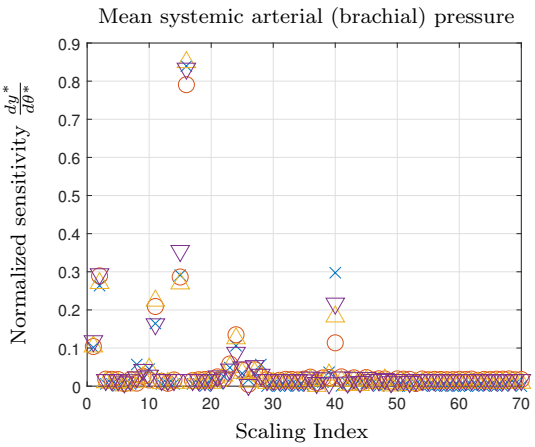
Mean systemic arterial (brachial) pressure
Normalized sensitivity $\frac{dy^*}{d\theta^*}$
Scaling Index

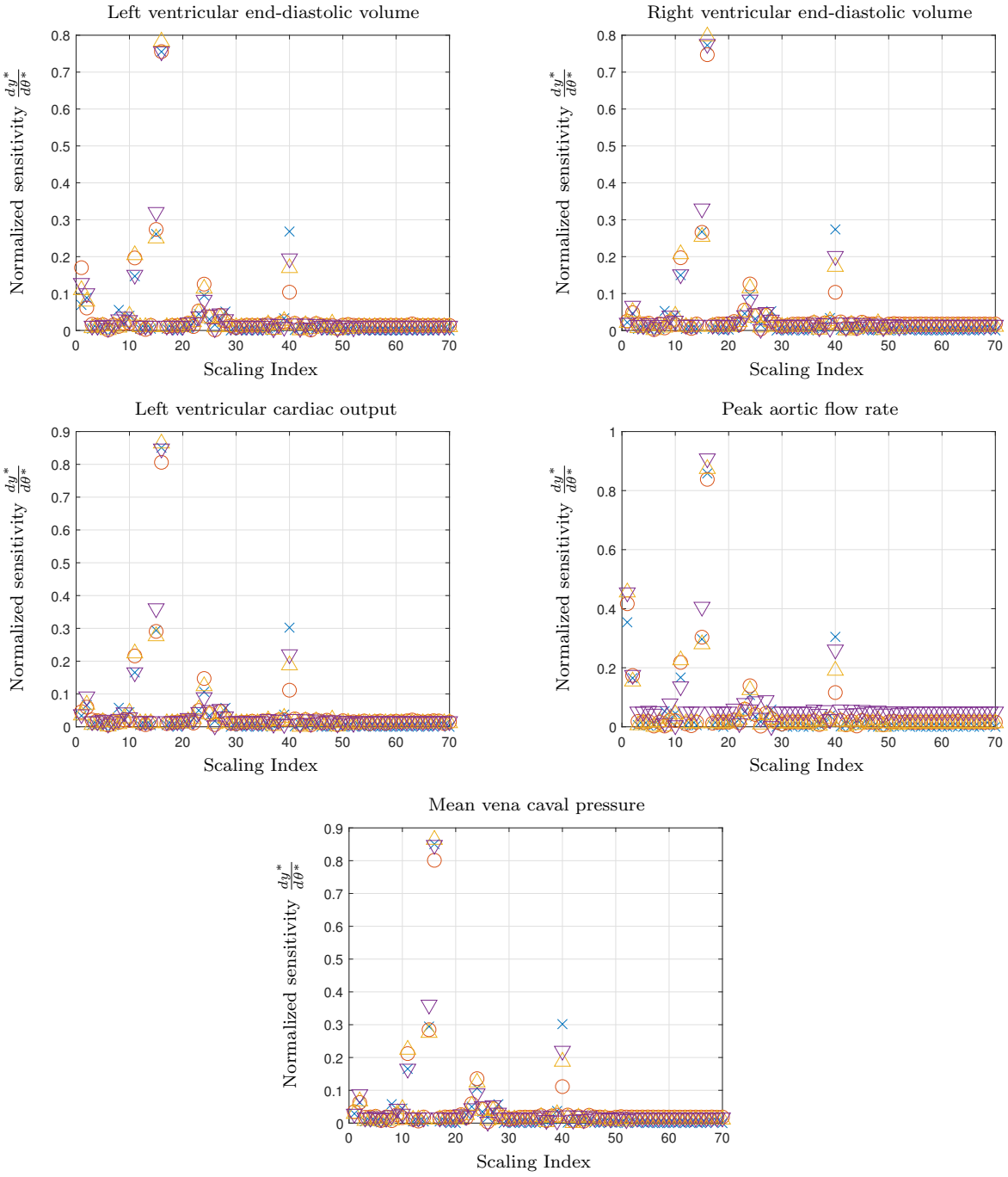

Figure 3.9: Normalized LH-OAT parameter sensitivities for various clinical measurement predictions. Scaling indices are linked to parameters tabulated in Table 3.5.

CHAPTER 4

Data Assimilation and Parameter Estimation

As seen from the previous chapter, a complete cardiovascular model requires dozens of model parameters. Furthermore, these parameters are related in a nonlinear fashion to both model predictions and one another. As such, adjustment of these parameters in an ad-hoc way is time-consuming and requires significant end-user expertise. To lower this hurdle, development of an algorithm for automated parameter estimation based on clinical data would be ideal. In this work, an ensemble Kalman Filter (EnKF) is developed for this purpose. In this chapter, a brief overview of Kalman filtering algorithms is given, followed by further details for particular filters and alterations to improve filter robustness. The chapter closes with a simple "toy" problem to demonstrate the effectiveness of the EnKF under decreasing measurement availability.

4.1 Overview of the Kalman filter framework

The ensemble Kalman filter (EnKF) was originally developed by Evensen [Eve03] to assimilate measurement data into high-dimensional, nonlinear meteorological models. However, it is only one instance of a larger framework for Kalman filtering algorithms [JUD95, TAC14]. To describe this framework, we begin with the governing equations for the *true* state and measurements of a discrete-time, possibly nonlinear dynamical system with *additive* noise:

$$\begin{aligned} \boldsymbol{x}_n &= M(\boldsymbol{x}_{n-1}) + \boldsymbol{w}_{n-1}, \\ \boldsymbol{y}_n &= h(\boldsymbol{x}_n) + \boldsymbol{v}_n. \end{aligned} \tag{4.1}$$

In Eq. (4.1), we never have access to the true state, nor do we know the exact noise

levels. Therefore, we will distinguish our *model* equations with a change in font to indicate multivariate random variables:

$$\begin{aligned} \boldsymbol{X}_n &= M(\boldsymbol{X}_{n-1}) + \boldsymbol{W}_{n-1}, \\ \boldsymbol{Y}_n &= h(\boldsymbol{X}_n) + \boldsymbol{V}_n. \end{aligned} \tag{4.2}$$

To proceed, we constrain the distributions of the initial state, process noise, and measurement noise to be Gaussian with independent covariances. Furthermore, we require the noise distributions to be zero mean. More concisely:

$$\begin{aligned} \boldsymbol{X}_0 &\sim \mathcal{N}(\hat{\boldsymbol{x}}_0, \mathbf{P}_0), \\ \boldsymbol{W}_n &\sim \mathcal{N}(0, \mathbf{W}_n), \\ \boldsymbol{V}_n &\sim \mathcal{N}(0, \mathbf{V}_n), \end{aligned} \tag{4.3}$$

where $\mathcal{N}(\mu, \mathbf{C})$ symbolizes a Gaussian distribution with mean μ and covariance matrix $\mathbf{C}$. Since the noise is assumed to be zero-mean, we can propogate the mean model state $\hat{\boldsymbol{x}}$ and its associated measurement $\hat{\boldsymbol{y}}$ forward in time using Eq. (4.2):

$$\begin{aligned} \hat{\boldsymbol{x}}_n^- &= M(\hat{\boldsymbol{x}}_{n-1}), \\ \hat{\boldsymbol{y}}_n &= h(\hat{\boldsymbol{x}}_n^-), \end{aligned} \tag{4.4}$$

where the "-" superscript indicates that the true measurement has not been incorporated into this prediction (often called the *forecast* step). At this point, we would like to improve our forecast using the true measurement. One intuitive way to do so is to use some linear combination of the difference between the model's predicted measurement $\hat{\boldsymbol{y}}_n$ and the true measurement $\boldsymbol{y}_n$ (usually called the *innovation*). Specifically, we would like to write:

$$\begin{aligned} \tilde{\boldsymbol{y}}_n &= \boldsymbol{y}_n - \hat{\boldsymbol{y}}_n, \\ \hat{\boldsymbol{x}}_n^+ &= \hat{\boldsymbol{x}}_n^- + \boldsymbol{K}_n \tilde{\boldsymbol{y}}_n, \end{aligned} \tag{4.5}$$

where $\boldsymbol{K}_n$ is the Kalman gain matrix and the "+" superscript denotes the assimilation of measurement data into the prediction (known as the *analysis* step). Instead of defining $\boldsymbol{K}_n$ arbitrarily, we can optimize it using the error in the state vector (note omission of the time step index for brevity):

$$\tilde{\boldsymbol{x}} = \boldsymbol{x} - \hat{\boldsymbol{x}}. \tag{4.6}$$

With the state error defined, we can write the error covariance matrix for the analysis step in terms of the Kalman gain, the innovation, and the forecast step:

$$\begin{aligned}
\tilde{\boldsymbol{x}}^+ &= \tilde{\boldsymbol{x}}^- - \boldsymbol{K}\tilde{\boldsymbol{y}}, \\
\mathbf{P}^+ &= E[\tilde{\boldsymbol{x}}^+\tilde{\boldsymbol{x}}^{+T}] \\
&= E[\tilde{\boldsymbol{x}}^-\tilde{\boldsymbol{x}}^{-T} - \tilde{\boldsymbol{x}}^-\tilde{\boldsymbol{y}}^T\boldsymbol{K}^T - \boldsymbol{K}\tilde{\boldsymbol{y}}\tilde{\boldsymbol{x}}^{-T} + \boldsymbol{K}\tilde{\boldsymbol{y}}\tilde{\boldsymbol{y}}^T\boldsymbol{K}^T] \\
&= \mathbf{P}^- - \mathrm{cov}(\tilde{\boldsymbol{x}}^-, \tilde{\boldsymbol{y}})\boldsymbol{K}^T - \boldsymbol{K}\mathrm{cov}(\tilde{\boldsymbol{y}}, \tilde{\boldsymbol{x}}^-) + \boldsymbol{K}\mathrm{cov}(\tilde{\boldsymbol{y}}, \tilde{\boldsymbol{y}})\boldsymbol{K}^T,
\end{aligned} \tag{4.7}$$

where $E[\cdot]$ is the expected value and $\mathrm{cov}(a, b)$ is the cross-covariance matrix of a and b. For convenience, we define $\mathbf{Q} \equiv \mathrm{cov}(\tilde{\boldsymbol{x}}^-, \tilde{\boldsymbol{y}})$ and $\mathbf{R} \equiv \mathrm{cov}(\tilde{\boldsymbol{y}}, \tilde{\boldsymbol{y}})$. Then, under the Gaussian assumption, we can obtain an expression for the Kalman gain by minimizing the trace of the analysis error with respect to $\boldsymbol{K}$ (i.e., by seeking to minimize the error in each state variable after analysis):

$$\begin{aligned}
\frac{\partial[\mathrm{tr}(\mathbf{P}^+)]}{\partial \boldsymbol{K}} &= 0 \\
-2\mathbf{Q} + 2\boldsymbol{K}\mathbf{R} &= 0 \\
\boldsymbol{K} &= \mathbf{Q}\mathbf{R}^{-1}.
\end{aligned} \tag{4.8}$$

Finally, we can also compute the analysis error covariance by combining the final lines of Eqs. (4.7) and (4.8):

$$\mathbf{P}^+ = \mathbf{P}^- - \boldsymbol{K}\mathbf{Q}. \tag{4.9}$$

To summarize, *all* Kalman filtering algorithms share the following steps:

1. Forecast (advance model in time):

$$\begin{aligned} \hat{\boldsymbol{x}}_n^- &= M(\hat{\boldsymbol{x}}_{n-1}), \\ \hat{\boldsymbol{y}}_n &= h(\hat{\boldsymbol{x}}_n^-). \end{aligned} \tag{4.10}$$

2. Compute the Kalman gain (determine strength of model correction):

$$\boldsymbol{K}_n = \mathbf{Q}_n {\mathbf{R}_n}^{-1}. \tag{4.11}$$

3. Analysis (correct model using measurement):

$$\begin{aligned} \hat{\boldsymbol{x}}_n^+ &= \hat{\boldsymbol{x}}_n^- + \boldsymbol{K}_n \tilde{\boldsymbol{y}}_n, \\ \mathbf{P}_n^+ &= \mathbf{P}_n^- - \boldsymbol{K}_n \mathbf{Q}_n. \end{aligned} \tag{4.12}$$

Within the steps above, the primary source of differentiation between Kalman methods is in the computation of the covariance/cross-covariance matrices $\mathbf{Q}_n$, $\mathbf{R}_n$, and $\mathbf{P}_n^-$. In the following two sections, we will see that the classical Kalman filter is able to compute these matrices analytically for linear systems. By contrast, to work with nonlinear systems, the EnKF will develop approximations by using the statistics of an ensemble of simulations.

4.2 The classical Kalman filter

To develop the framework in Sec. 4.1, we assumed:

1. Both process noise $\boldsymbol{w}$ and measurement noise $\boldsymbol{v}$ are additive.

2. The initial state distribution $\boldsymbol{X}_0$, process noise distribution $\boldsymbol{W}$, and measurement noise distribution $\boldsymbol{V}$ are Gaussian with independent covariances.

3. The process and measurement noise distributions have zero mean.

In the standard Kalman filter [Kal60], we additionally assume that the dynamics and measurement operator are both linear, so the forecast step given in Eq. (4.10) becomes:

$$\begin{aligned} \hat{\boldsymbol{x}}_n^- &= \boldsymbol{M}\hat{\boldsymbol{x}}_{n-1}^+, \\ \hat{\boldsymbol{y}}_n &= \boldsymbol{H}\hat{\boldsymbol{x}}_n^-. \end{aligned} \tag{4.13}$$

Next, by making frequent use of the independent covariances listed above, we compute the Kalman gain from Eq. (4.11):

$$\begin{aligned} \tilde{\boldsymbol{y}}_n &= \boldsymbol{y}_n - \hat{\boldsymbol{y}}_n = \boldsymbol{H}\boldsymbol{x}_n + \boldsymbol{v}_n - \boldsymbol{H}\hat{\boldsymbol{x}}_n = \boldsymbol{H}\tilde{\boldsymbol{x}}_n + \boldsymbol{v}_n, \\ \mathbf{Q}_n &= E[\tilde{\boldsymbol{x}}_n^- \tilde{\boldsymbol{y}}_n^T] = E[\tilde{\boldsymbol{x}}_n^- (\tilde{\boldsymbol{x}}_n^{-\mathbf{T}} \boldsymbol{H}^{\mathbf{T}} + \boldsymbol{v}_n^T)] = \mathrm{cov}(\tilde{\boldsymbol{x}}_n^-, \tilde{\boldsymbol{x}}_n^-) \\ &= \mathbf{P}_n^- \boldsymbol{H}^T, \\ \mathbf{R}_n &= E[\tilde{\boldsymbol{y}}_n \tilde{\boldsymbol{y}}_n^T] = \boldsymbol{H}\mathbf{P}_n^- \boldsymbol{H}^T + \mathbf{V}_n, \\ \mathbf{P}_n^- &\approx E[(\boldsymbol{X}_n - \hat{\boldsymbol{x}}_n^-)(\boldsymbol{X}_n - \hat{\boldsymbol{x}}_n^-)^T] \\ &= E[(\boldsymbol{M}\boldsymbol{X}_{n-1} + \boldsymbol{W}_n - \boldsymbol{M}\hat{\boldsymbol{x}}_{n-1}^+)(\boldsymbol{M}\boldsymbol{X}_{n-1} + \boldsymbol{W}_n - \boldsymbol{M}\hat{\boldsymbol{x}}_{n-1}^+)^T] \\ &= \boldsymbol{M}E[(\boldsymbol{X}_{n-1} - \hat{\boldsymbol{x}}_{n-1}^+)(\boldsymbol{X}_{n-1} - \hat{\boldsymbol{x}}_{n-1}^+)^T]\boldsymbol{M}^T + \mathbf{W}_n \\ &= \boldsymbol{M}\mathbf{P}_{n-1}^+ \boldsymbol{M}^T + \mathbf{W}_n, \\ \boldsymbol{K}_n &= \mathbf{Q}_n {\mathbf{R}_n}^{-1} = \mathbf{P}_n^- \boldsymbol{H}^T (\boldsymbol{H}\mathbf{P}_n^- \boldsymbol{H}^T + \mathbf{V}_n)^{-1}. \end{aligned} \tag{4.14}$$

Finally, the analysis step:

$$\begin{aligned} \hat{\boldsymbol{x}}_n^+ &= \hat{\boldsymbol{x}}_n^- + \boldsymbol{K}_n \tilde{\boldsymbol{y}}_n, \\ \mathbf{P}_n^+ &= \mathbf{P}_n^- - \boldsymbol{K}_n \mathbf{Q}_n = (\mathbf{I} - \boldsymbol{K}_n \boldsymbol{H})\mathbf{P}_n^-. \end{aligned} \tag{4.15}$$

Thus, we see that the classical Kalman filter is able to analytically evaluate all of the covariance and cross-covariance matrices necessary for its operation. However, there are some important points to observe about Eqs. (4.14) and (4.15), specifically with regard to the state covariance matrix $\mathbf{P}_n$. First, we assume that the forecast state covariance matrix $\mathbf{P}_n^-$ is an adequate approximation to the forecast error covariance (hence the approximation sign in the first line of $\mathbf{P}_n^-$'s development). Second, $\mathbf{P}_n^-$ is defined recursively from $\mathbf{P}_{n-1}^+$. For

these two reasons, the specification of the initial state covariance $\mathbf{P}_0$ plays a significant part in the initial performance of our model, though its role may diminish as data is assimilated through $\mathbf{P}_n^+$. Finally, while it is possible for $\mathbf{P}_{n-1}^+$ to approach zero at the analysis step, the following forecast step $\mathbf{P}_n^-$ is always bounded from below by the process noise covariance $\mathbf{W}_n$. As we will see in the next section, the state covariance in the EnKF does not inherently possess such a lower bound, and thus requires artificial *covariance inflation* for robustness.

4.3 The ensemble Kalman filter (EnKF)

4.3.1 Evensen's original method

In the case that the dynamics and measurement operator are nonlinear, then the matrices $\mathbf{P}_n^-$, $\mathbf{Q}_n$, and $\mathbf{R}_n$ can no longer be evaluated analytically. Instead, the ensemble Kalman filter (EnKF) makes approximations to these matrices by using statistics from an ensemble of L models. We begin with the usual forecast step for every i^{th} ensemble member:

$$\begin{aligned} \boldsymbol{x}_{i,n}^- &= M(\boldsymbol{x}_{i,n-1}^+), \\ \boldsymbol{y}_{i,n} &= h(\boldsymbol{x}_{i,n}^-), \end{aligned} \qquad \text{for } i = 1, 2, \ldots, L. \tag{4.16}$$

Following the ensemble forecast, we approximate the mean of the system state and measurement distributions using their ensemble means:

$$\begin{aligned} \hat{\boldsymbol{x}}_n^- \approx \bar{\boldsymbol{x}}_n^- &\equiv \frac{1}{L-1} \sum_{i=1}^{L} \boldsymbol{x}_{i,n}^-, \\ \hat{\boldsymbol{y}}_n \approx \bar{\boldsymbol{y}}_n &\equiv \frac{1}{L-1} \sum_{i=1}^{L} \boldsymbol{y}_{i,n}. \end{aligned} \tag{4.17}$$

The necessary covariance/cross-covariance matrices are approximated in a similar fashion:

$$\mathbf{P}_n^- = E[(\boldsymbol{X}_n - \boldsymbol{x}_n)(\boldsymbol{X}_n - \boldsymbol{x}_n)^T] \approx \frac{1}{L-1}\sum_{i=1}^{L}(\boldsymbol{x}_{i,n}^- - \bar{\boldsymbol{x}}_n^-)(\boldsymbol{x}_{i,n}^- - \bar{\boldsymbol{x}}_n^-)^T,$$

$$\mathbf{Q}_n = E[\tilde{\boldsymbol{x}}_n^- \tilde{\boldsymbol{y}}_n^T] \approx \frac{1}{L-1}\sum_{i=1}^{L}(\boldsymbol{x}_{i,n}^- - \bar{\boldsymbol{x}}_n)(\boldsymbol{y}_{i,n} - \bar{\boldsymbol{y}}_n)^T, \tag{4.18}$$

$$\mathbf{R}_n = E[\tilde{\boldsymbol{y}}_n \tilde{\boldsymbol{y}}_n^T] \approx \frac{1}{L-1}\sum_{i=1}^{L}(\boldsymbol{y}_{i,n} - \bar{\boldsymbol{y}}_n)(\boldsymbol{y}_{i,n} - \bar{\boldsymbol{y}}_n)^T + \mathbf{V}_n.$$

The Kalman gain is then computed normally, and is shared across all ensemble members:

$$\boldsymbol{K}_n = \mathbf{Q}_n {\mathbf{R}_n}^{-1}. \tag{4.19}$$

Finally, to avoid spurious correlations in the ensemble covariance [BLE98], noise is added to the innovation of each ensemble member during the analysis step:

$$\boldsymbol{x}_{i,n}^+ = \boldsymbol{x}_{i,n}^- + \boldsymbol{K}_n(\boldsymbol{y}_n + \boldsymbol{\epsilon}_i - \boldsymbol{y}_{i,n}) \qquad \text{for } i = 1, 2, \ldots, L, \tag{4.20}$$

where each perturbation $\boldsymbol{\epsilon}_i$ is taken from $\boldsymbol{V}_n$.

4.3.2 Covariance inflation

By comparing $\mathbf{P}_n^-$ in Eqs. (4.15) and (4.18), we see that only the former possesses a lower bound (due to the presence of $\mathbf{W}_n$). Thus, in the original EnKF formulation, it is possible for the state covariance to approach zero (i.e., $\boldsymbol{x}_{i,n} \to \bar{\boldsymbol{x}}_n$ for all i). This phenomenon is known as *covariance collapse* or *filter divergence* [WH12], and results in $\boldsymbol{K}_n$ going to zero, after which point all measurements are ignored. To avoid this behavior, it is necessary to artificially inflate the state covariance:

$$\boldsymbol{x}_{i,n} \leftarrow \boldsymbol{x}_{i,n} + \alpha_n(\boldsymbol{x}_{i,n} - \bar{\boldsymbol{x}}_n) + \boldsymbol{\beta}_{i,n}, \tag{4.21}$$

where α_n is a multiplicative inflation factor common to all ensemble members [AA99], and $\boldsymbol{\beta}_{i,n}$ is an additive inflation factor drawn for each ensemble member from a random distribution [MH00]. For high-dimensional systems, additive inflation is generally undesirable, as

it requires individual tuning for each element of the state vector. For multiplicative inflation, there are several different inflation techniques; the one employed in this work is the relaxation-to-prior-spread (RTPS) method developed by Whitaker and Hamill [WH12]. In this method, we first compute the standard deviation for the ensemble after forecast and analysis:

$$\begin{aligned} \boldsymbol{\sigma}_n^- &= \sqrt{\frac{1}{L-1}\sum_{i=1}^{L}(\boldsymbol{x}_{i,n}^- - \bar{\boldsymbol{x}}_n^-)}, \\ \boldsymbol{\sigma}_n^+ &= \sqrt{\frac{1}{L-1}\sum_{i=1}^{L}(\boldsymbol{x}_{i,n}^+ - \bar{\boldsymbol{x}}_n^+)}. \end{aligned} \tag{4.22}$$

We then use the normalized difference between the two standard deviations to drive each ensemble member away from the ensemble mean:

$$\boldsymbol{x}_{i,n}^+ - \bar{\boldsymbol{x}}_n^+ \leftarrow (\boldsymbol{x}_{i,n}^+ - \bar{\boldsymbol{x}}_n^+)\left(c\frac{\boldsymbol{\sigma}_n^- - \boldsymbol{\sigma}_n^+}{\boldsymbol{\sigma}_n^+} + 1\right) \qquad \text{for } i = 1, 2, \ldots, L, \tag{4.23}$$

where the constant c (typically between 0.5 and 1) controls the amount of relaxation. Note that for implementation, it is more convenient to rewrite the above equation as

$$\boldsymbol{x}_{i,n}^+ \leftarrow \boldsymbol{x}_{i,n}^+ + c\frac{\boldsymbol{\sigma}_n^- - \boldsymbol{\sigma}_n^+}{\boldsymbol{\sigma}_n^+}(\boldsymbol{x}_{i,n}^+ - \bar{\boldsymbol{x}}_n^+). \tag{4.24}$$

The RTPS scheme was chosen for this work because of its simplicity (it requires only one tunable parameter) and its robustness: numerical experiments from weather forecast models (i.e., chaotic systems) show stable model errors that are relatively insensitive to the value of the inflation parameter [WH12].

4.4 EnKF parameter estimation methods

4.4.1 Joint versus dual estimation

As discussed above, the EnKF uses observational data to correct the state (i.e., the dependent variables) of a dynamical system as forecasted by a model. However, the EnKF is also capable of *combined estimation*, in which it simultaneously tunes the state and parameters of a model. To estimate a vector of parameters $\boldsymbol{\theta}$, two filtering approaches have been developed in the literature. In the first, known as *joint estimation* [BR80], the state vector is augmented with the parameter vector:

$$\boldsymbol{x}_{i,n} \leftarrow [\boldsymbol{x}_{i,n} \quad \boldsymbol{\theta}_{i,n}] \quad \text{for } i = 1, 2, \ldots, L, \tag{4.25}$$

and a single filter is applied to this augmented vector. While the simplicity of this approach is attractive, it can also reduce stability of a dynamical system by increasing its degrees of freedom. As an alternative, the state and parameters can be filtered separately in a process known as *dual estimation* [WN97, MSG05]. To do so, we need an artificial dynamical model for the parameter vector (i.e., a way to perform a "parameter forecast"). A straightforward method is a random walk with kernel smoothing [Wes93, Liu00, MSG05]:

$$\boldsymbol{\theta}^{-}_{i,n} = \mathcal{N}(a\boldsymbol{\theta}^{+}_{i,n-1} + (1-a)\bar{\boldsymbol{\theta}}^{+}_{n-1}, (1-a^2)\mathbf{Z}^{+}_{n-1}), \tag{4.26}$$

where a is a constant close to 1 (usually between 0.97 and 0.995) and $\mathbf{Z}$ is the parameter covariance matrix. From Eq. (4.26), we see that keeping a near 1 results in a significant shrinkage of the effective variance used in the random walk. This variance reduction prevents uncertain parameters from becoming over-dispersed [Wes93], and instead allows the filtering process to gradually drive each parameter towards an optimal value.

In this work, a slightly different approach is taken from these previously established methods: we employ the kernel-smoothed random walk discussed above and allow the EnKF to filter the resulting parameter vector, but omit filtering of the dynamical state. The reasons for this omission are twofold: state filtering is not subject to physical constraints (e.g., mass

conservation), and we would like to study the degree to which a parametrically-optimized reduced-order model approximates individual patient measurements without artificial alterations to its state.

4.4.2 The complete parameter estimation procedure

Listed below are the complete set of steps used for parameter estimation through the EnKF. Note that $\boldsymbol{\theta}$ has been inserted into the list of arguments for the dynamics M and the measurement h to make their parameter dependence clear.

1. Generate perturbed measurements:

$$\boldsymbol{y}'_n = \boldsymbol{y}_n + \boldsymbol{\epsilon}_i, \quad \boldsymbol{\epsilon}_i \sim \mathcal{N}(0, \mathbf{V}_n) \quad \text{for } i = 1, 2, \ldots, L. \tag{4.27}$$

2. Parameter forecast step:

$$\begin{aligned} \mathbf{Z}^+_{n-1} &= \text{var}(\boldsymbol{\theta}^+_{n-1}), \\ \boldsymbol{\theta}^-_{i,n} &= \mathcal{N}(a\boldsymbol{\theta}^+_{i,n-1} + (1-a)\bar{\boldsymbol{\theta}}^+_{n-1}, (1-a^2)\mathbf{Z}^+_{n-1}) \quad \text{for } i = 1, 2, \ldots, L. \end{aligned} \tag{4.28}$$

3. State forecast with forecasted parameters:

$$\begin{aligned} \boldsymbol{x}^-_{i,n} &= M(\boldsymbol{x}^+_{i,n-1}, \boldsymbol{\theta}^-_{i,n}), \\ \boldsymbol{y}_{i,n} &= h(\boldsymbol{x}^-_{i,n}, \boldsymbol{\theta}^-_{i,n}), \end{aligned} \quad \text{for } i = 1, 2, \ldots, L. \tag{4.29}$$

4. Compute parameter Kalman gain:

$$\begin{aligned} \mathbf{Q}_{\theta,n} &= \frac{1}{L-1}\sum_{i=1}^{L}(\boldsymbol{\theta}^-_{i,n} - \bar{\boldsymbol{\theta}}_n)(\boldsymbol{y}_{i,n} - \bar{\boldsymbol{y}}_n)^T, \\ \mathbf{R}_{\theta,n} &= \frac{1}{L-1}\sum_{i=1}^{L}(\boldsymbol{y}_{i,n} - \bar{\boldsymbol{y}}_n)(\boldsymbol{y}_{i,n} - \bar{\boldsymbol{y}}_n)^T + \mathbf{V}_n, \\ \boldsymbol{K}_{\theta,n} &= \mathbf{Q}_{\theta,n}\mathbf{R}^{-1}_{\theta,n}. \end{aligned} \tag{4.30}$$

5. Parameter analysis step:

$$\boldsymbol{\theta}^+_{i,n} = \boldsymbol{\theta}^-_{i,n} + \boldsymbol{K}_{\theta,n}(\boldsymbol{y}'_n - \boldsymbol{y}_{i,n}) \quad \text{for } i = 1, 2, \ldots, L. \tag{4.31}$$

6. Parameter RTPS covariance inflation:

$$\begin{aligned}
\boldsymbol{\sigma}_{\theta,n}^{-} &= \sqrt{\frac{1}{L-1}\sum_{i=1}^{L}(\boldsymbol{\theta}_{i,n}^{-} - \bar{\boldsymbol{\theta}}_{n}^{-})}, \\
\boldsymbol{\sigma}_{\theta,n}^{+} &= \sqrt{\frac{1}{L-1}\sum_{i=1}^{L}(\boldsymbol{\theta}_{i,n}^{+} - \bar{\boldsymbol{\theta}}_{n}^{+})}, \\
\boldsymbol{\theta}_{i,n}^{+} &\leftarrow \boldsymbol{\theta}_{i,n}^{+} + c\frac{\boldsymbol{\sigma}_{\theta,n}^{-} - \boldsymbol{\sigma}_{\theta,n}^{+}}{\boldsymbol{\sigma}_{\theta,n}^{+}}(\boldsymbol{\theta}_{i,n}^{+} - \bar{\boldsymbol{\theta}}_{n}^{+}).
\end{aligned} \tag{4.32}$$

7. State forecast with analyzed parameters:

$$\begin{aligned}
\boldsymbol{x}_{i,n}^{-} &= M(\boldsymbol{x}_{i,n-1}^{+}, \boldsymbol{\theta}_{i,n}^{+}), \\
\boldsymbol{y}_{i,n} &= h(\boldsymbol{x}_{i,n}^{-}, \boldsymbol{\theta}_{i,n}^{+}),
\end{aligned} \qquad \text{for } i = 1, 2, \ldots, L. \tag{4.33}$$

Breaking down the set of procedures above, we see that steps 2 through 5 are the EnKF process for the parameters. Additionally, step 4 shows that the parameter/state covariance matrices are not necessary for computing the Kalman gain, as is the case with the traditional Kalman filter (though they can still be computed to derive uncertainty bounds). Finally, though we do not need the parameter/state covariance matrices in the filtering process, we still include covariance inflation to avoid $\mathbf{Q},\ \boldsymbol{K} \to 0$.

4.5 A simple EnKF example implementation

4.5.1 Model formulation

To illustrate the EnKF's operation in a parameter estimation context, we consider the example of a purely resistive flow splitter, as in Fig. 4.1. Referencing the figure, the model equations for this example are

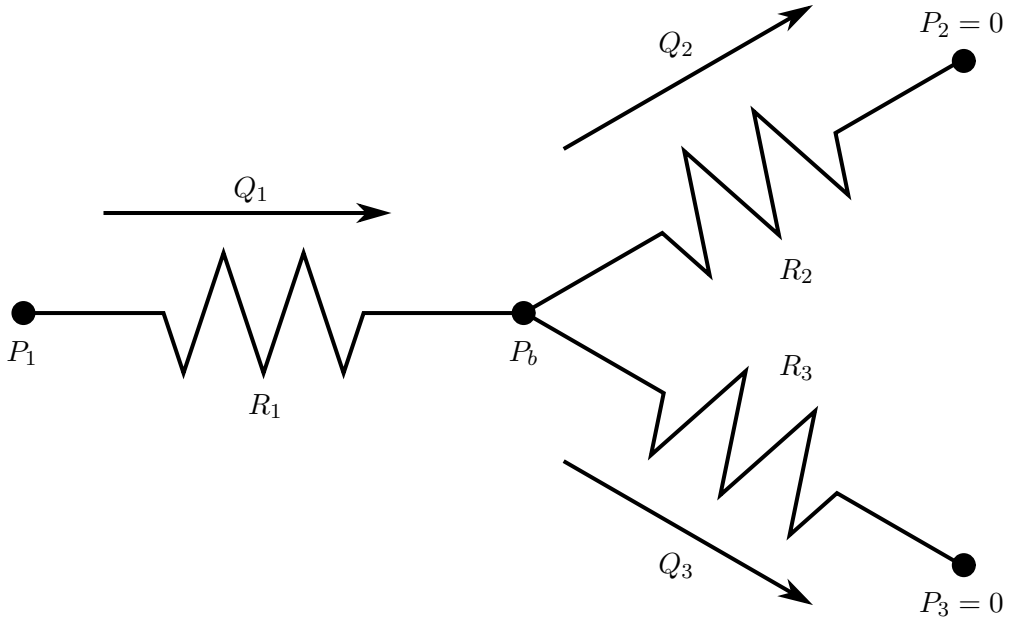

Figure 4.1: Schematic of a resistive flow splitter used for EnKF demonstration. Note that both outlets are connected to ground pressure.

$$\begin{aligned} Q_1 &= Q_2 + Q_3, \\ Q_1 &= \frac{P_1 - P_b}{R_1}, \\ Q_2 &= \frac{P_b}{R_2}, \\ Q_3 &= \frac{P_b}{R_3}. \end{aligned} \tag{4.34}$$

From these equations, it is apparent that this model has no derivative terms; this characteristic allows us to isolate the EnKF's behavior, as no error can be introduced through our choice of discretization. Also, these equations can be combined to produce the following relationship between upstream and junction pressure:

$$P_b = \frac{P_1}{R_1}\left(\frac{1}{R_1} + \frac{1}{R_2} + \frac{1}{R_3}\right)^{-1}. \tag{4.35}$$

Thus, in the event that P_1 is specified and the resistances are known, this system is completely determined. We will use such a model to produce our reference measurements $\boldsymbol{y}_n$ for the

EnKF, with the following values for upstream pressure and resistance:

$$\begin{aligned} P_1 &= \sin(2\pi t), \\ R_1 &= 1, \\ R_2 &= 1, \\ R_3 &= 2, \end{aligned} \tag{4.36}$$

where all quantities are dimensionless for simplicity. With these values, our reference system's solution is

$$\begin{aligned} P_{b,\text{ref}} &= \frac{2}{5}\sin(2\pi t), \\ Q_{1,\text{ref}} &= \frac{3}{5}\sin(2\pi t), \\ Q_{2,\text{ref}} &= \frac{2}{5}\sin(2\pi t), \\ Q_{3,\text{ref}} &= \frac{1}{5}\sin(2\pi t). \end{aligned} \tag{4.37}$$

Now, in the case that the resistances are unknown, we need four state variables for the system to be completely determined: P_1, P_b, and any two of the flowrates. P_1 will be taken as a known input forcing, so our measurement vector becomes

$$\boldsymbol{y}_{n,\text{complete}} = [P_{b,\text{ref}}\ Q_{2,\text{ref}}\ Q_{3,\text{ref}}]^T, \tag{4.38}$$

where Q_2 and Q_3 have been chosen over Q_1 arbitrarily. In most realistic scenarios, the measurement vector will not contain enough information for us to completely specify the system. Consequently, we will also consider cases in which our system is increasingly underdetermined:

$$\boldsymbol{y}_{n,\text{incomplete}} = [P_{b,\text{ref}}\ Q_{2,\text{ref}}]^T,$$
$$\boldsymbol{y}_{n,\text{sparse}} = P_{b,\text{ref}}. \tag{4.39}$$

For each of L ensemble members, these measurements will be perturbed independently by an equal magnitude:

$$\boldsymbol{\epsilon}_i \sim \begin{bmatrix} \mathcal{N}(0, 0.1) \\ \mathcal{N}(0, 0.1) \\ \mathcal{N}(0, 0.1) \end{bmatrix} \quad \text{for } i = 1, 2, \ldots, L. \tag{4.40}$$

Finally, there will be 1000 measurement assimilations per P_1 cycle, and the initial parameter distributions for the resistors are given in Table 4.1.

Table 4.1: Normal distribution characteristics for flow splitter resistances.

Parameter	Initial mean	Std. dev.	Lower bound
R_1	1.00	0.30	1×10^{-3}
R_2	1.00	0.30	1×10^{-3}
R_3	2.00	0.60	1×10^{-3}

4.5.2 Results

Fig. 4.2 illustrates the converged ensemble mean predictions for each unknown dynamical variable. From the figure, we see that the EnKF is able to generate highly accurate predictions for all variables of interest. While such agreement is expected for the case with a complete measurement set, the EnKF's advantage is that the accuracy is only slightly degraded in the underdetermined cases. To quantify this degradation, the $\boldsymbol{L}^2$-norm of the error for each dynamical variable is presented in Table 4.2. Since P_b is present in each measurement set, it is unsurprising that its error remains relatively constant across cases. By contrast, the sparse case results in an increase of error across one and two orders of magnitude, respectively, for Q_2 and Q_3 relative to the complete case. These two increases are

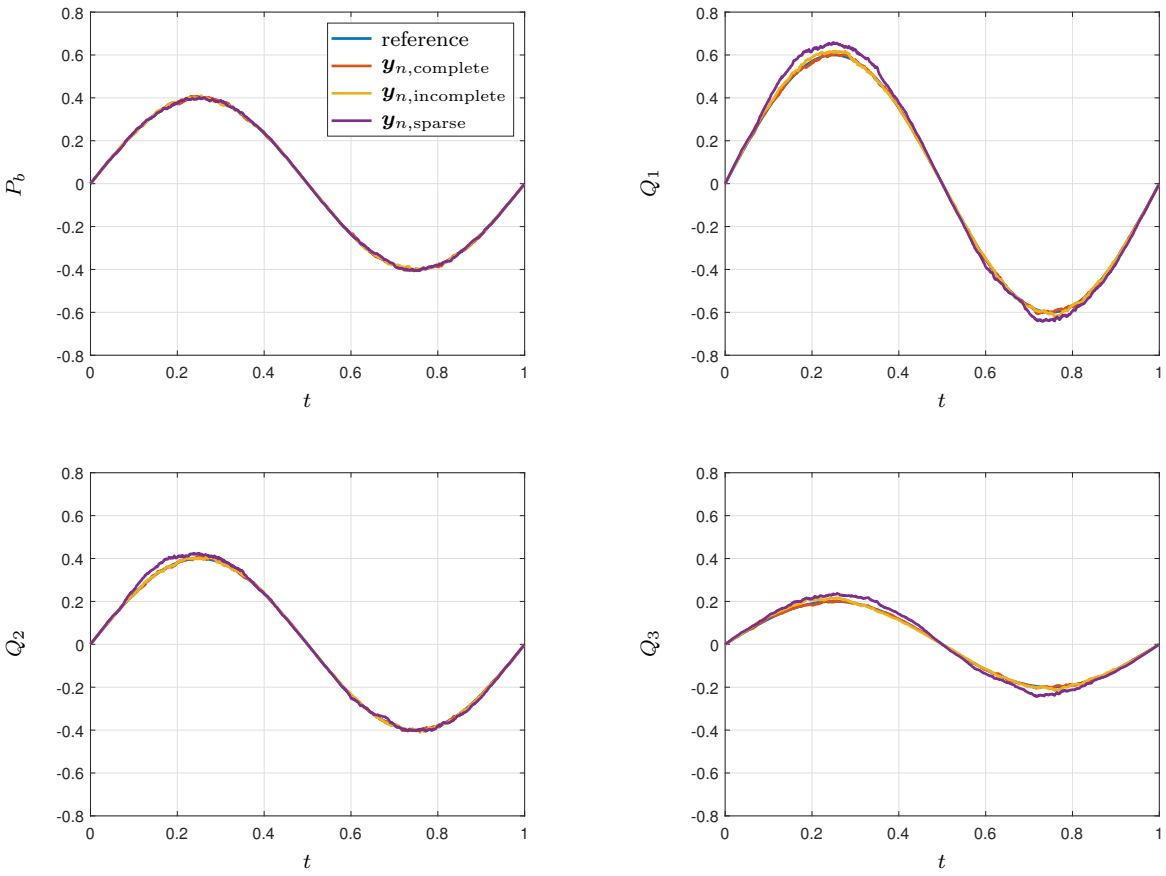

Figure 4.2: Comparison of ensemble mean predictions for varying levels of measurement availability. Note that all quantities are dimensionless.

somewhat expected, since we do not have measurements that directly constrain them. However, the concomitant increase of Q_1's error by two orders of magnitude illustrates upstream propagation of error (i.e., error in the outflow locations produces error in Q_1 due to their linkage in $Q_1 = Q_2 + Q_3$). Still, the absolute magnitude of these errors in all cases is quite small relative to the $\mathcal{O}(1)$ scale of the data. Thus, this example demonstrates that although the EnKF can benefit from additional measurement data, it can also give well-optimized parameters in spite of significantly limited measurement sets.

Table 4.2: $\boldsymbol{L}^2$ norm of error for ensemble mean predictions across varying levels of measurement availability.

	P_b	Q_1	Q_2	Q_3

complete	1.45×10^{-5}	1.93×10^{-5}	1.02×10^{-5}	7.55×10^{-6}
incomplete	1.16×10^{-5}	7.39×10^{-5}	1.24×10^{-5}	5.51×10^{-5}
sparse	1.21×10^{-5}	1.10×10^{-3}	2.07×10^{-4}	4.80×10^{-4}

CHAPTER 5

EnKF Estimation of Submodel Parameters

5.1 EnKF implementation for a 0D cardiovascular model

5.1.1 Model formulation

As a proof of concept, a dual-state parameter EnKF estimator was implemented for a simplified, fully compartmental cardiovascular model. A schematic of the model is shown in Fig. 5.1. The complete circulatory model is comprised of the following ODEs:

$$\begin{aligned}
\frac{dV_v}{dt} &= -Q, \\
\frac{dQ}{dt} &= \frac{1}{R_{va}+Z_c}\left[-E_vQ + \frac{dE_v}{dt}(V_v - V_0) - \left(1+\frac{Z_c}{R}\right)\frac{Q}{C} + \frac{P_a}{RC}\right], \\
\frac{dP_a}{dt} &= \left[\left(1+\frac{Z_c}{R}\right)C\right]^{-1}\left\{\left(1+\frac{Z_c}{R}\right)Q + \frac{CZ_c}{R}\left[-E_vQ + \frac{dE_v}{dt}(V_v - V_0)\right] - \frac{P_a}{R}\right\},
\end{aligned} \tag{5.1}$$

with an elastance model for the heart identical to the one presented in Sec. 2.2:

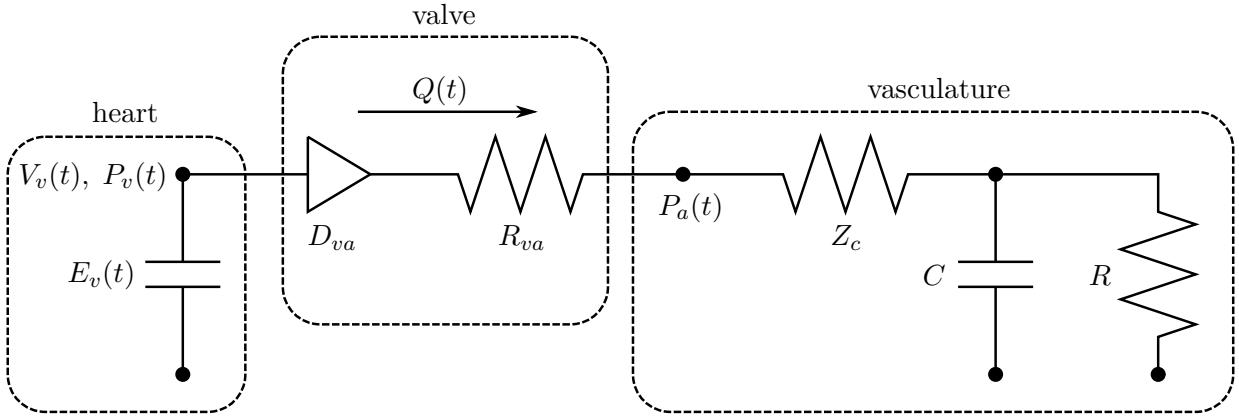

Figure 5.1: Schematic of the compartmental cardiovascular model used for EnKF testing.

$$
\begin{aligned}
E_v(\hat{t}) &= k\left(\frac{g_1}{1+g_1}\right)\left(\frac{1}{1+g_2}\right) + E_{\min}, \\
g_1 &= \left(\frac{\hat{t}}{\tau_1}\right)^{m_1}, \quad g_2 = \left(\frac{\hat{t}}{\tau_2}\right)^{m_2}, \\
k &= \frac{E_{\max} - E_{\min}}{\max\left[\left(\frac{g_1}{1+g_1}\right)\left(\frac{1}{1+g_2}\right)\right]}.
\end{aligned} \tag{5.2}
$$

Since E_v only depends on $\hat{t}$, the state vector has three elements:

$$
\boldsymbol{x} = [V_v \; Q \; P_a]^T. \tag{5.3}
$$

To determine the valve state, ventricular pressure first is computed as

$$
P_v = E_v(\hat{t})(V_v - V_0), \tag{5.4}
$$

then the valve is considered to be a perfect diode:

$$
D_{va} = \begin{cases} \text{open}, & P_v > P_a \\ \text{closed}, & P_a > P_v. \end{cases} \tag{5.5}
$$

Collecting the parameters presented in Eqs. (5.1) and (5.2) yields $\boldsymbol{\theta}_i$ for each ensemble member:

$$
\boldsymbol{\theta}_i = [Z_c \; R \; C \; E_{\max} \; \tau_1 \; \tau_2 \; m_1 \; m_2]^T. \tag{5.6}
$$

The measurements used to optimize these parameters are ventricular volume and pulmonary arterial flowrate during systole:

$$
\boldsymbol{y}_i = [V_v(\hat{t}) \; Q(\hat{t})]^T \quad \text{for } 0 \le \hat{t} \le t_s, \tag{5.7}
$$

where t_s is the time of pulmonary valve closure. Data assimilation ends with systole because the heart and vasculature are effectively decoupled during diastole; thus, continuing

assimilation could introduce spurious correlations between ventricular measurements and vascular parameters and vice-versa. The measurement vector was predicated upon clinical availability of measurements: equivalent MRI data was taken from two volunteers, one normotensive and one exhibiting pulmonary arterial hypertension. Based on knowledge of the MRI measurement system, the perturbations ϵ_i added to the clinical measurement $\boldsymbol{y}_n$ are drawn from

$$\boldsymbol{\epsilon}_i \sim \begin{bmatrix} \mathcal{N}(0\ \mathrm{cm}^3, 2.5\ \mathrm{cm}^3) \\ \mathcal{N}(0\ \mathrm{cm}^3/\mathrm{s}, 2.5\ \mathrm{cm}^3/\mathrm{s}) \end{bmatrix} \quad \text{for } i = 1, 2, \ldots, L. \tag{5.8}$$

Each ensemble member is integrated forward in time using the 4th/5th-order adaptive Runge-Kutta Cash Karp method, with clinical measurements sampled for assimilation at approximately 80 Hz. Finally, since the model is an open-loop circulation (i.e., blood does not return to the ventricle during diastole), each ensemble member is randomly re-initialzed at the start of each cardiac cycle:

$$V_{v,i}(\hat{t} = 0) \sim \mathcal{N}(135\ \mathrm{mL}, 10\ \mathrm{mL}) \quad \text{for } i = 1, 2, \ldots, L. \tag{5.9}$$

The parameters for this submodel are tabulated with their descriptions, distribution properties, and converged values in Tables 5.2 through 5.4. Due to the availability of clinical measurements, these parameters were chosen to be characteristic of the right ventricle and pulmonary circulation. However, if measurement data were available for the systemic circulation, the model could also be used there (with appropriately altered parameters).

5.1.2 Results

As a check on the stability of the estimation procedure, Fig. 5.2 shows the evolution of the variance for a representative selection of model parameters in both the healthy and hypertensive cases. The Hill function parameters m_2 and τ_2 have been omitted from this subset, but their respective behaviors follow m_1 and τ_1. All variances have been normalized by the initial ensemble mean for comparison, and indicate that the ensemble parameter

spread remains well-bounded from above at 3% or less of the initial value, with most variances falling below 1%. Referring to $\mathbf{Q}_n$ in Eq. (4.8), having this upper bound on parameter spread is a necessary condition for $\boldsymbol{K}_n$ to remain stable.

Turning to quantities of medical relevance, Fig. 5.3 compares clinically-measured flow rates during systole to those obtained from the ensemble using parameter values at the end of the optimization procedure. We see that for both the healthy and hypertensive cases, the flow rates largely fall within the middle 95% quantile of the ensemble predictions. Interestingly, a "secondary hump" observed in the clinical data for the hypertensive case is captured by the ensemble. In the literature, this behavior has been attributed to a strong vortex in the pulmonary artery evident in MR imaging of patients with manifest pulmonary hypertension [RRK08, RRK15]. Of course, it is not possible to simulate such vortices in a zero-dimensional model; however, this result shows that the EnKF optimization procedure allows emulation of their effect on flow rate in a reduced-order model.

As an indication of predicted cardiac loading, Fig. 5.4 displays pressure-volume traces during systole in the healthy and hypertensive cases. Importantly, although ventricular pressure is not directly constrained by clinical measurements, the pressures fall within physiological ranges [NS01, KCG08] for both the healthy and hypertensive cases. This matching suggests that the EnKF's estimate for elastance model parameters, together with non-invasive measurements of ventricular volume, can give a reasonable estimate of ventricular pressure. Also, we see that for similar ejection fractions, the hypertensive ventricle operates at considerably higher pressure, and therefore performs more mechanical work to achieve similar pulmonary perfusion.

To place the clinical results in the context of the two ensembles' parameter sets, Fig. 5.5 displays their mean input impedance magnitudes and elastance functions. For reference, input impedance is calculated as

$$Z_{\text{in}} = \frac{R + Z_c + j\omega R Z_c C}{1 + j\omega RC} \tag{5.10}$$

and provides a measure of the vascular load placed on the heart. It is worth mentioning that

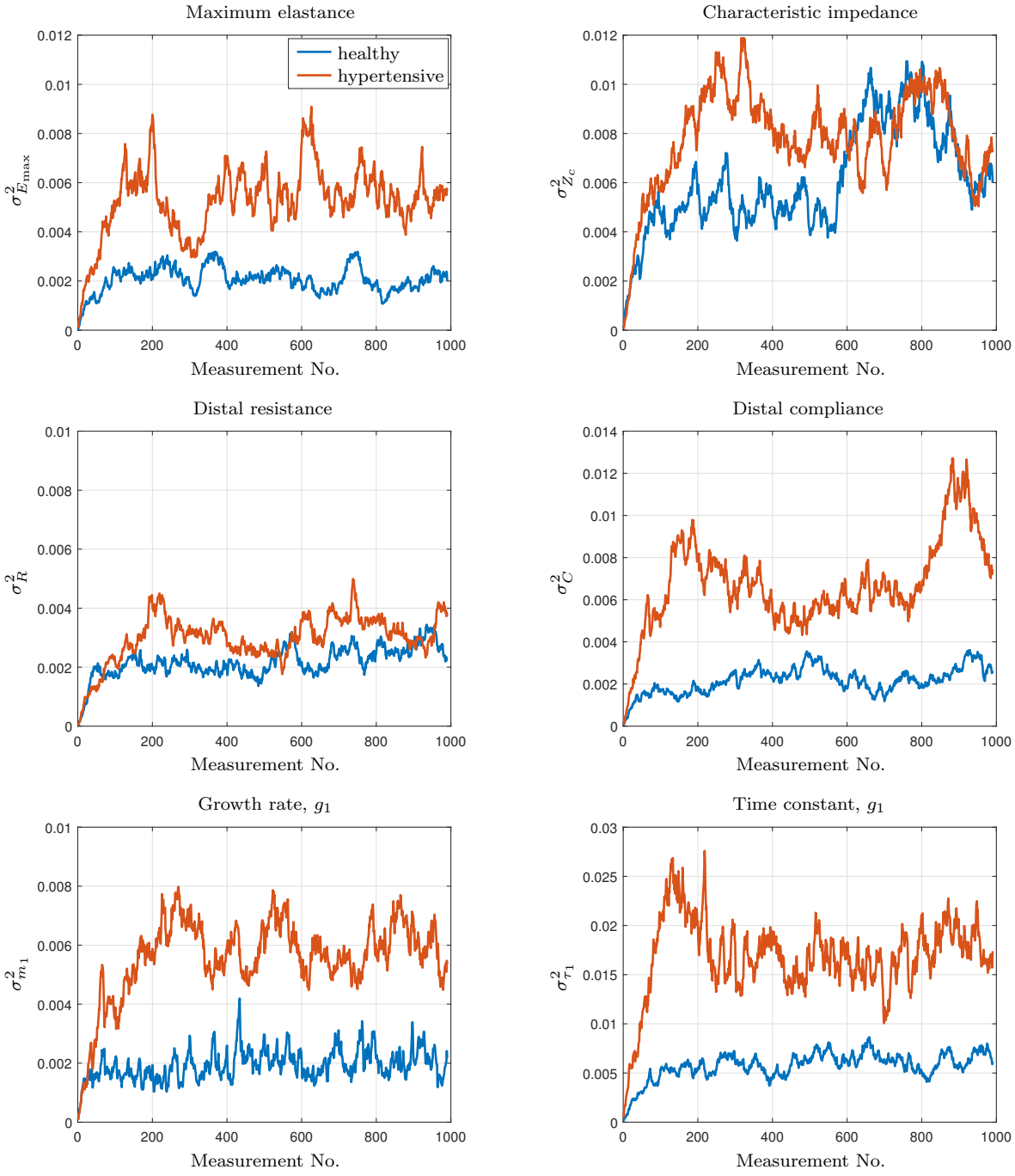

Figure 5.2: Evolution of selected parameter variances (normalized by initial ensemble mean values) during optimization for the 0D pulmonary model.

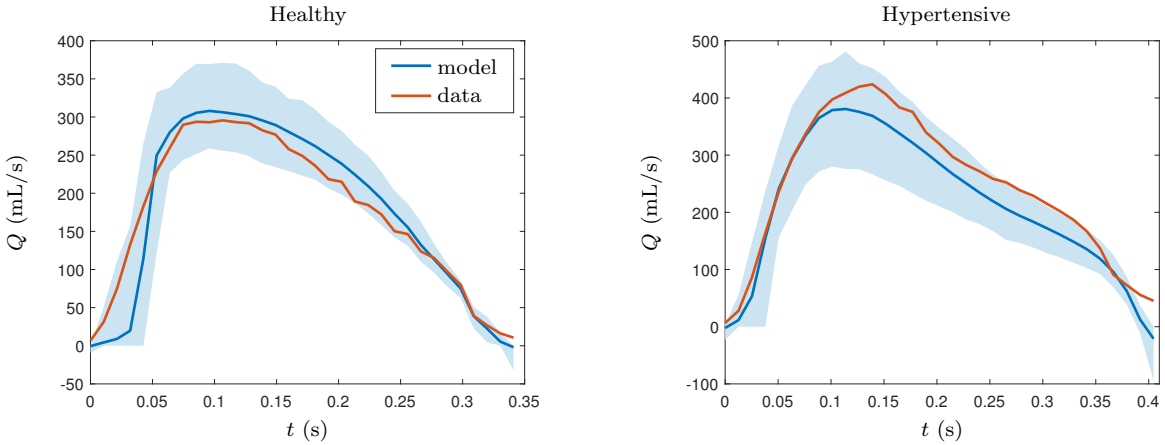

Figure 5.3: Converged ensemble flow rate comparison against patient MRI data during systole. Shaded blue area is the middle 95% quantile of the ensembles.

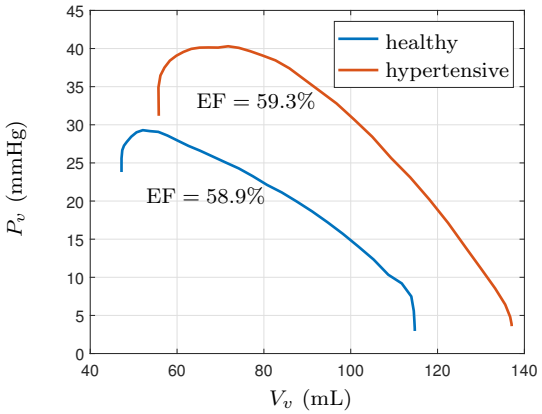

Figure 5.4: Comparison of pressure-volume traces during systole for the converged healthy and hypertensive cases. EF: ejection fraction.

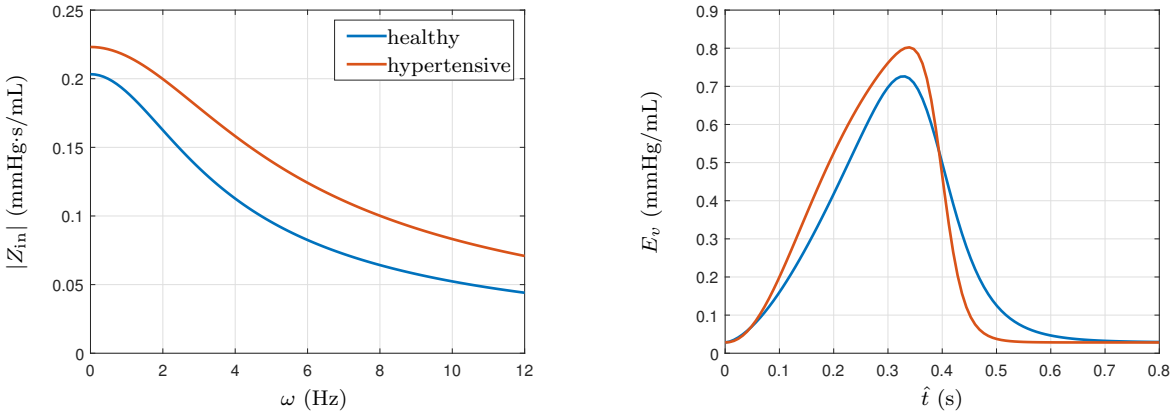

Figure 5.5: Input impedance and ventricular elastance comparisons for healthy and hypertensive cases.

the shape of these impedance curves matches those observed in the literature for systemic Windkessel models validated against clinical data [WLW09]. As expected, for all input frequencies, the hypertensive case has a greater impedance modulus, and therefore a larger afterload. In response, the cardiac elastance during systole ($\hat{t} \lesssim 0.4\ s$) is larger for the hypertensive case. This increased elastance is a proxy for the right ventricular hypertrophy observed in patients with hypertension [AIH14]. Taken together, the impedance and elastance results demonstrate that the EnKF yields parameter sets for this model that not only enable realistic predictions, but also possess straightforward physical interpretations.

5.2 EnKF implementation for a coupled 0D-1D cardiovascular model

5.2.1 Model formulation

To further test the EnKF estimator, it is also applied to a coupled 0D-1D model of the lower leg. The model is outlined schematically in Fig. 5.6. The 1D representation of an artery, as well as the handling of bifurcations, are the same as developed in Chapter 2. However, the boundary treatments have been modified to account for known inflow data and the use of three-element Windkessel models at each terminal outlet. For convenience in discussing

these treatments, we repeat the characteristic form [Ala06, SFP03] of the 1D equatons:

$$\frac{\partial \mathbf{W}}{\partial t} + \mathbf{\Lambda}\frac{\partial \mathbf{W}}{\partial x} = \mathbf{LS},$$

$$\mathbf{L} = \begin{bmatrix} c/A & 1 \\ -c/A & 1 \end{bmatrix}, \quad \mathbf{W} = \begin{bmatrix} W_1 \\ W_2 \end{bmatrix} = \begin{bmatrix} u + 4\sqrt{\frac{\beta}{2\rho}}(A^{1/4} - A_0^{1/4}) \\ u - 4\sqrt{\frac{\beta}{2\rho}}(A^{1/4} - A_0^{1/4}) \end{bmatrix} = \begin{bmatrix} u + 4(c - c_0) \\ u - 4(c - c_0) \end{bmatrix}, \tag{5.11}$$

$$\mathbf{\Lambda} = \begin{bmatrix} u + c & 0 \\ 0 & u - c \end{bmatrix}, \quad \mathbf{S} = \begin{bmatrix} 0 \\ -22\pi\nu u/A \end{bmatrix},$$

where all symbols have the same definitions as in their original presentation. We also recall that the expressions for W_1 and W_2 in Eqs. (5.11) can be combined to express area and average velocity as

$$\begin{aligned} A &= \left(\frac{2\rho}{\beta}\right)^2 \left(\frac{W_1 - W_2}{8} + c_o\right)^4, \\ u &= \frac{W_1 + W_2}{2}. \end{aligned} \tag{5.12}$$

As shown in the following two sections, the 1D boundaries are treated through use of Eqs. (5.12), which show that $W_{1,2}$ completely specify A and u at a node.

5.2.1.1 Proximal boundary

At the proximal boundary of the 1D network (i.e., the popliteal artery's inlet), we specify u from volunteer MRI data. Then, since Eq. (5.11) shows that W_2 can be extrapolated from interior nodes by following characteristic lines [LTH09a, Ala06, SFP03], the time-advancement scheme is:

1. Update W_2 at boundary by extrapolating from interior nodes:

$$W_{2,\text{pop}}^{(n)}(x = 0) = W_{2,\text{pop}}^{(n-1)}(x = -\lambda_2^{(n-1)}\Delta t) - 22\pi\nu \frac{u_{\text{pop}}^{(n-1)}(x = -\lambda_2^{(n-1)}\Delta t)}{A_{\text{pop}}^{(n-1)}(x = -\lambda_2^{(n-1)}\Delta t)}. \tag{5.13}$$

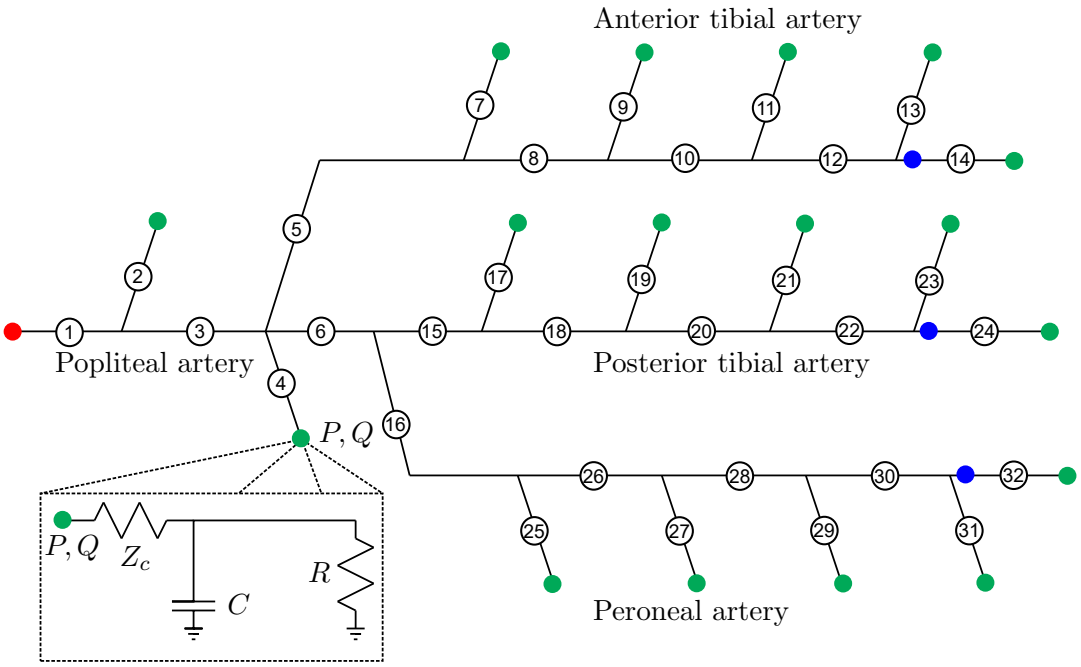

Figure 5.6: Connectivity diagram of complete one-dimensional arterial network. Inset shows a representative 0D terminal outlet, present at all green nodes. The red node is the inflow boundary, while blue nodes represent velocity measurement locations for the EnKF parameter estimator. Artery ID numbers match Table 5.5.

2. Set W_1 and update A at the proximal boundary according to Eqs. (5.12):

$$\begin{aligned} W_{1,\text{pop}}^{(n)}(x=0) &= 2u_{\text{pop}}^{(n)} - W_{2,\text{pop}}^{(n)}(x=0), \\ A_{\text{pop}}^{(n)}(x=0) &= \left(\frac{2\rho}{\beta_{\text{pop}}}\right)^2 \left(\frac{W_{1,\text{pop}}^{(n)}(x=0) - W_{2,\text{pop}}^{(n)}(x=0)}{8} + c_{0,\text{pop}}\right)^4. \end{aligned} \tag{5.14}$$

5.2.1.2 Distal boundary

At the distal end of the 1D network, we couple terminal arteries to three-element Windkessel models, as sketched in Fig. 5.6. To do so, we begin with an implicit Euler discretization for the governing ODE of a three-element Windkessel (all notation follows Fig. 5.6):

$$P^{(n)} + Z_c C \frac{P^{(n)} - P^{(n-1)}}{\Delta t} = (Z_c + R)Q^{(n)} + Z_c RC \frac{Q^{(n)} - Q^{(n-1)}}{\Delta t}. \tag{5.15}$$

Coupling between the 0D and 1D domains occurs through the following substitutions into Eq. (5.15), based on the characteristic relations in Eqs. (5.12) alongside the arterial pressure-area relationship presented in Chapter 2:

$$\begin{aligned} P^{(n)} &= \beta(\sqrt{A^{(n)}} - \sqrt{A_0}), \\ A^{(n)} &= \left(\frac{2\rho}{\beta}\right)^2 \left(\frac{W_1^{(n)} - W_2^{(n)}}{8} + c_o\right)^4, \\ Q^{(n)} &= A^{(n)} u^{(n)} = A^{(n)} \frac{W_1^{(n)} + W_2^{(n)}}{2}. \end{aligned} \tag{5.16}$$

Since $W_1^{(n)}$ can be extrapolated from interior nodes, Eqs. (5.15) and (5.16) form a single nonlinear equation for $W_2^{(n)}$:

$$2\rho\left(1+\frac{RC}{\Delta t}\right)\left(\frac{W_1^{(n)}-W_2^{(n)}}{8}+c_o\right)^2 -$$

$$\left(\frac{2\rho}{\beta}\right)^2\left(Z_c+R+\frac{Z_cRC}{\Delta t}\right)\left(\frac{W_1^{(n)}-W_2^{(n)}}{8}+c_o\right)^4\left(\frac{W_1^{(n)}+W_2^{(n)}}{2}\right)+\tilde{P}^{(n-1)}=0, \quad (5.17)$$

$$\tilde{P}^{(n-1)}=\frac{Z_cRC}{\Delta t}Q^{(n-1)}-\frac{RC}{\Delta t}P^{(n-1)}-\left(1+\frac{RC}{\Delta t}\right)\beta\sqrt{A_0}.$$

The above equation is solved with Newton-Raphson iteration, using values at the previous time step as an initial guess.

5.2.1.3 0D-1D parameter estimation

Compared to the 0D pulmonary model, the coupled 0D-1D leg model has a considerably larger parameter space for optimization. Specifically, there are 17 total terminal Windkessel models whose R and C require estimation (Z_c is fixed to the artery's characteristic impedance $\rho c_0/A_0$ to avoid spurious reflections [APP08]), plus 32 1D segments whose stiffness parameter β needs estimation. However, the measurement set is of comparable size to the pure 0D test, consisting of simultaneous planar MRI blood velocity measurements along the anterior tibial, posterior tibial, and peroneal arteries:

$$\boldsymbol{y}=[\bar{u}_{\text{ant}}\ \bar{u}_{\text{post}}\ \bar{u}_{\text{per}}]^T. \quad (5.18)$$

For the data perturbations ϵ_i, the distributions were given a standard deviation of 2.5 cm/s:

$$\boldsymbol{\epsilon}_i \sim \begin{bmatrix}\mathcal{N}(0\text{ cm}^3, 2.5\text{ cm}^3/\text{s})\\ \mathcal{N}(0\text{ cm}^3, 2.5\text{ cm}^3/\text{s})\\ \mathcal{N}(0\text{ cm}^3, 2.5\text{ cm}^3/\text{s})\end{bmatrix} \quad \text{for } i=1,2,\ldots,L. \quad (5.19)$$

The clinical measurements above are mapped onto the 1D arterial network at the inlet nodes to segments 14, 24, and 32 (the blue nodes in Fig. 5.6), i.e.

$$\boldsymbol{y}_i = [\bar{u}_{14,i}(x=0)\ \bar{u}_{24,i}(x=0)\ \bar{u}_{32,i}(x=0)]^T \quad \text{for } i = 1, 2, \ldots, L. \tag{5.20}$$

To make the optimization procedure tractable, initial values are first manually assigned for R, C, and β so that 1) mean arterial pressure falls in a realistic range between 90 and 95 mmHg, and 2) the minimum arterial wave speed c_0 is well-matched near 8 m/s [KKJ07]. To proceed, we recall that the LH-OAT sensitivity analysis in Sec. 3.4 indicated that Windkessel compliance and arterial stiffness strongly influence arterial measurements of pressure and peak flow (A_0 is excluded to simplify the tuning procedure, as its impact could not be distinguished from that of β). We also note that the time-mean of a three-element Windkessel yields

$$\bar{Q} = \frac{\bar{P}}{Z_c + R}. \tag{5.21}$$

However, since Z_c is fixed to avoid spurious reflections, the mean component of flow in this case can only be adjusted through changes to R. Therefore, in each of the segments onto which the velocity measurements are mapped, we will directly tune C, R, and β, such that a portion of the parameter vector is

$$\boldsymbol{\theta}_a = [R_{14}\ C_{14}\ R_{24}\ C_{24}\ R_{32}\ C_{32}\ \beta_{14}\ \beta_{24}\ \beta_{32}]^T. \tag{5.22}$$

Note the ensemble index i has been dropped for brevity. For the remaining terminals, a scaling parameter is introduced for all R and C values within a given artery:

$$\boldsymbol{\theta}_b = [\alpha_{R,\text{ant}}\ \alpha_{C,\text{ant}}, \alpha_{R,\text{post}}\ \alpha_{C,\text{post}}, \alpha_{R,\text{per}}\ \alpha_{C,\text{per}}]^T. \tag{5.23}$$

These parameters are used to uniformly scale all terminals upstream of a measurement site. For example, the anterior tibial scalings are applied as

$$\left.\begin{aligned} R_j &\leftarrow \alpha_{R,\text{ant}} R_j \\ C_j &\leftarrow \alpha_{C,\text{ant}} C_j \end{aligned}\right\} \quad \text{for } j = 7, 9, 11, 13. \tag{5.24}$$

The posterior tibial, peroneal, and popliteal arteries follow the same procedure, with the popliteal scalings given by the average value in the remaining three arteries. The complete parameter vector thus contains only 15 parameters, given by the concatenation of $\boldsymbol{\theta}_a$ and $\boldsymbol{\theta}_b$:

$$\boldsymbol{\theta} = [\boldsymbol{\theta}_a \ \boldsymbol{\theta_b}]^T. \tag{5.25}$$

Finally, to ensure the arterial wave speed remains well-matched, β for upstream segments is scaled by the fractional change in the corresponding measured segment. Again using the anterior tibial artery for illustration:

$$\beta_j \leftarrow \frac{\beta_{14}^+ - \beta_{14}^-}{\beta_{14}^-}\beta_j \quad \text{for } j = 7, 9, 11, 13. \tag{5.26}$$

The posterior tibial and peroneal stiffness parameters are changed similarly, and the popliteal segments are then altered according to the average fractional change across the three downstream arteries.

5.2.2 Results

To demonstrate the converged ensemble's predictive utility, Fig. 5.7 compares model velocities at the measurement locations against patient MRI data. For all measurement locations, it can be seen that the model does reasonably well at capturing waveform shape and peak velocities. Though some overshoot exists in terms of systolic pulse duration and maximum backflow rate, Table 5.1 shows that the time-averaged velocity (and hence mean perfusion) is well-matched, especially for the anterior tibial and peroneal arteries. It is also worth emphasizing that these results were produced with an extremely limited measurement set: the measurement vector dimension is $\mathcal{O}(1)$, while the overall parameter space dimension is $\mathcal{O}(100)$. Thus, these predictions could likely be improved through additional measurements with which to constrain the parameter estimation procedure.

As in the fully 0D problem, the ensemble generated for this case is able to output estimates of patient pressure. The pressure waveforms are given in Fig. 5.8, and fall within

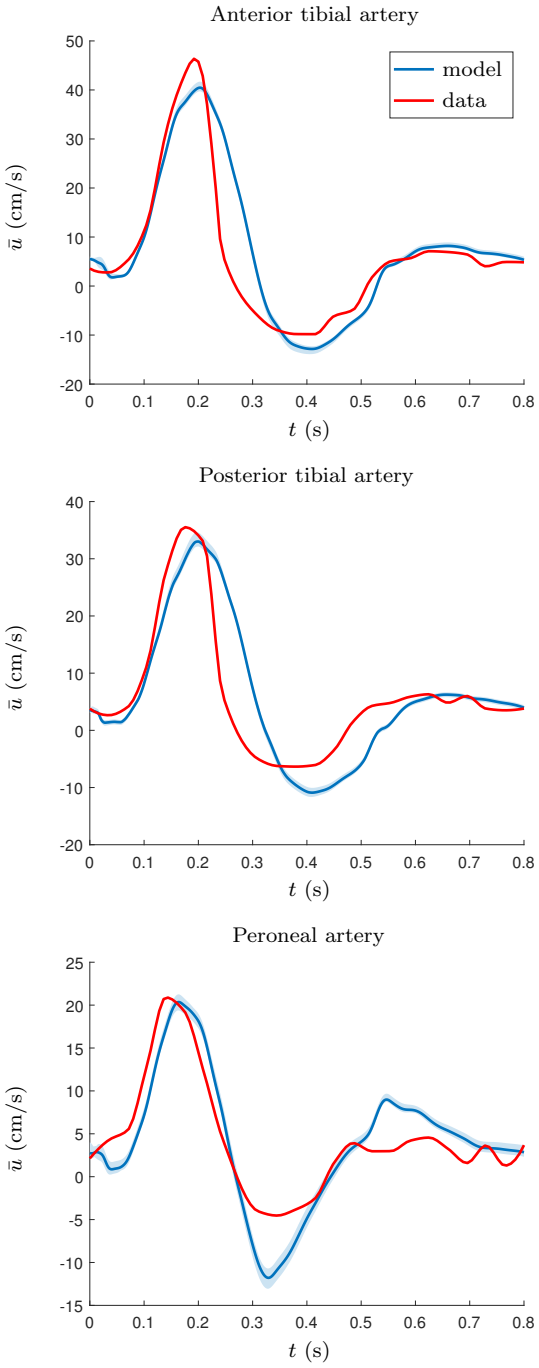

Figure 5.7: Converged ensemble velocity prediction compared against patient measurements for the coupled 0D-1D lower leg case. Shaded blue region is the middle 95% quantile.

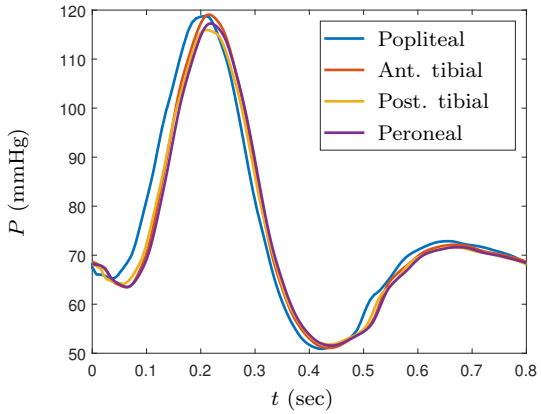

Figure 5.8: Ensemble mean pressure traces at inflow (popliteal) and outflow (all other) arteries for the coupled 0D-1D lower leg case.

a physiogical range for the lower leg of a healthy adult [Goh07]. Furthermore, they show appropriate time delays between the input waveform (the popliteal artery) and the outputs (all others). While actual patient pressure readings would be useful to validate these predictions, their placement within a realistic range again demonstrates that EnKF-optimized parameter sets can produce adequate first-order estimates of non-measured quantities for particular patients.

Finally, to confirm estimator stability and ensemble parameter convergence, Fig. 5.9 displays selected parameter variances: the scaling factors are omitted for resistances in non-measured terminal branches, but follow patterns similar to that shown for the compliance scalings. Akin to Fig. 5.2, we see that the parameter variances remain well-bounded under increased model complexity and parameter space dimension for all parameters except the

Table 5.1: Time-averaged velocity comparisons between model predictions and clinicial data for the coupled 0D-1D lower leg case.

Location	Data $\bar{u}$ (cm/s)	Model $\bar{u}$ (cm/s)	Relative diff. (%)
Ant. tibial	6.27	7.55	20.5
Post. tibial	5.97	5.96	−0.54
Peroneal	4.21	4.06	−3.69

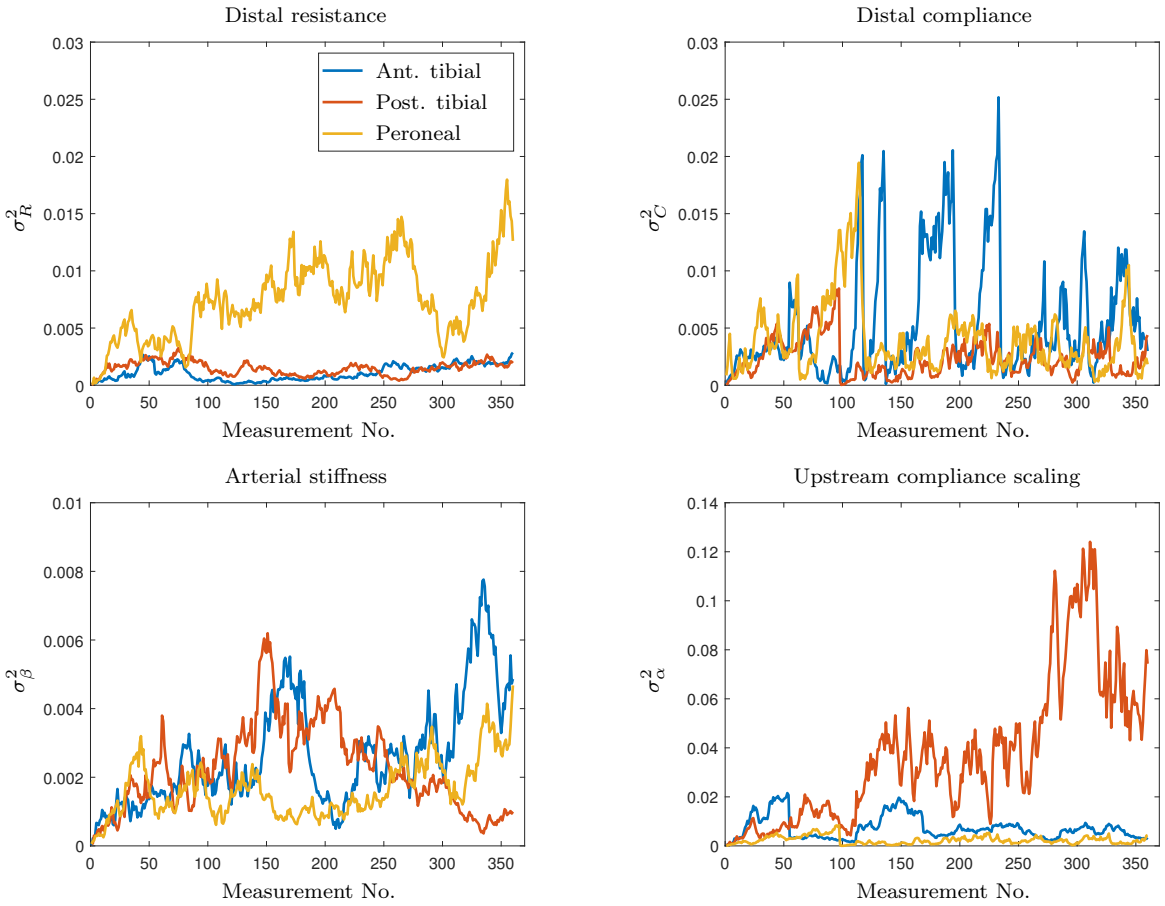

Figure 5.9: Evolution of selected parameter variances (normalized by initial ensemble mean values) during optimization for the coupled 0D-1D lower leg model.

compliance scaling. However, as displayed in Fig. 5.7, the converged ensemble's velocity predictions are tightly clustered around the mean, suggesting that the variability in upstream Windkessel submodels does not strongly influence overall model accuracy in this case.

5.3 Tables of parameter values, distribution characteristics, and model geometry

Table 5.2: Normal distribution characteristics for 0D pulmonary model parameters.

Parameter	Initial mean	Std. dev.	Lower bound	Upper bound	Units
Z_c	2.00×10^5	2×10^4	1×10^3	—	Pa·s/m^3

R	3×10^7	3×10^6	1×10^5	—	Pa·s/m^3
C	1×10^{-8}	1×10^{-9}	5×10^{-9}	—	m^3/Pa
$E_{\max}$	1.4×10^8	7×10^6	1×10^6	2×10^8	Pa/m^3
τ_1	0.25	0.10	0.01	—	s
τ_2	0.30	0.02	0.01	—	s
m_1	2.00	0.2	1	—	—
m_2	20.0	2.0	1	—	—

Table 5.3: Converged parameter values for the 0D model in the healthy case.

Parameter	Value	Units
Z_c	2.37×10^5	Pa·s/m^3
R	2.82×10^7	Pa·s/m^3
C	1.35×10^{-8}	m^3/Pa
$E_{\max}$	9.68×10^7	Pa/m^3
τ_1	0.913	s
τ_2	0.392	s
m_1	1.642	—
m_2	10.66	—

Table 5.4: Converged parameter values for the 0D model in the hypertensive case.

Parameter	Value	Units
Z_c	2.01×10^5	Pa·s/m^3
R	2.89×10^7	Pa·s/m^3
C	8.64×10^{-9}	m^3/Pa
$E_{\max}$	1.07×10^8	Pa/m^3
τ_1	0.224	s
τ_2	0.400	s
m_1	2.132	—

m_2	20.74	—

Table 5.5: Geometric data for the one-dimensional arterial network.

ID	Length (mm)	Radius (mm)	Thickness (mm)
1	23.5	3.25	0.50
2	20.4	0.88	0.15
3	32.2	2.95	0.50
4	11.5	0.65	0.10
5	13.4	2.35	0.39
6	34.2	2.93	0.50
7	7.04	0.72	0.12
8	68.9	2.35	0.39
9	27.6	0.76	0.12
10	28.8	2.10	0.35
11	23.5	0.58	0.10
12	120	2.10	0.35
13	19.1	0.48	0.08
14	164	1.13	0.19
15	54.2	2.10	0.35
16	35.6	2.03	0.35
17	15.6	0.75	0.12
18	19.0	1.90	0.35
19	24.5	0.45	0.07
20	26.7	1.90	0.35
21	13.1	0.56	0.07
22	44.9	1.78	0.30
23	11.7	0.63	0.10
24	146	1.18	0.20
25	28.0	1.06	0.15

26	41.2	1.99	0.35
27	10.5	0.63	0.10
28	121	1.99	0.35
29	5.14	0.48	0.07
30	36.4	1.55	0.25
31	31.3	0.78	0.12
32	40.7	0.97	0.20

Table 5.6: Normal distribution characteristics for coupled 0D-1D lower leg model parameters.

Parameter	Initial mean	Std. dev.	Lower bound	Upper bound	Units
R_{14}	1.17×10^{10}	1×10^{9}	1×10^{10}	1×10^{11}	Pa·s/m^3
R_{24}	2.48×10^{10}	2×10^{9}	1×10^{10}	1×10^{11}	Pa·s/m^3
R_{32}	6.79×10^{10}	1×10^{10}	1×10^{10}	1×10^{11}	Pa·s/m^3
C_{14}	3.97×10^{-10}	4×10^{-11}	1×10^{-10}	1×10^{-9}	m^3/Pa
C_{24}	1.96×10^{-10}	2×10^{-11}	1×10^{-10}	1×10^{-9}	m^3/Pa
C_{32}	7.24×10^{-12}	2×10^{-12}	7×10^{-12}	2×10^{-11}	m^3/Pa
β_{14}	7.79×10^{7}	8×10^{6}	2×10^{7}	2×10^{8}	Pa/m
β_{24}	7.60×10^{7}	8×10^{6}	2×10^{7}	2×10^{8}	Pa/m
β_{32}	1.12×10^{8}	1×10^{7}	2×10^{7}	2×10^{8}	Pa/m
$\alpha_{R,\text{ant}}$	1.00	0.2	0.1	—	—
$\alpha_{R,\text{post}}$	1.00	0.2	0.1	—	—
$\alpha_{R,\text{per}}$	1.00	0.2	0.1	—	—
$\alpha_{C,\text{ant}}$	1.00	0.2	0.1	—	—
$\alpha_{C,\text{post}}$	1.00	0.2	0.1	—	—
$\alpha_{C,\text{per}}$	1.00	0.2	0.1	—	—

Table 5.7: Converged ensemble mean parameter values for the coupled 0D-1D lower leg model.

ID	β (Pa/m $\times 10^{8}$)	R (Pa·s/m^3 $\times 10^{10}$)	C (m^3/Pa $\times 10^{-10}$)
1	0.32	—	—
2	1.32	2.91	1.79
3	0.39	—	—
4	1.60	5.31	0.99
5	0.34	—	—
6	0.53	—	—
7	1.11	4.30	1.21
8	0.34	—	—
9	0.99	3.85	1.36
10	0.38	—	—
11	1.42	6.63	0.79
12	0.38	—	—
13	1.65	9.66	0.54
14	0.71	2.36	1.10
15	0.72	—	—
16	0.53	—	—
17	1.97	4.03	0.37
18	0.88	—	—
19	3.11	10.9	0.14
20	0.88	—	—
21	2.05	7.20	0.21
22	0.86	—	—
23	2.28	5.60	0.27
24	1.31	2.90	1.13
25	0.84	1.99	2.63
26	0.56	—	—
27	1.58	5.63	0.93
28	0.56	—	—

29	1.92	9.75	0.54
30	0.66	—	—
31	1.24	5.35	0.97
32	1.35	7.17	7.73×10^{-2}

CHAPTER 6

Conclusion

6.1 Summary and Future Work

With reference to the research objectives outlined in Sec. 1.3, the work presented here has demonstrated significant progress. Specifically, we have achieved the following goals:

- Coupled a one-dimensional submodel of the major arteries to zero-dimensional submodels of the peripheral vasculature, heart, and lungs to create a closed-loop cardiovascular model capable of providing organ-level fluid dynamical data
- Employed a reduced-order baroreflex model to predict cardiovascular behavior due to neurogenic hypertension and acute hemorrhage
- Implemented the ensemble Kalman filter (EnKF) to enable data-driven parameter tuning for patient-specific models of the pulmonary vasculature and lower leg

Furthermore, validation of the closed-loop model against literature data showed that it is capable of reasonably reproducing both global and local (at the spatial resolution of the major arteries) cardiovascular dynamics measured *in vivo*. Demonstration of the latter capability is especially important, as it indicates that this model is suitable for embedding within a three-dimensional organ model (i.e., it will be able to predict the perfusion of the organ's tissue, and react appropriately if the tissue is damaged). No available literature to date has achieved this type of coupling, making it an important direction for future effort.

In addition to coupling with a higher-order organ model, the current cardiovascular model could be improved or extended by:

- Implementation of a model for cerebral autoregulation to enable the cerebral vasculature to act independently of the baroreflex, as expected from *in vivo* measurements [MKF79]

- Usage of machine learning methods (e.g., evolutionary algorithms or artificial neural networks) as computationally-efficient function approximators [DBN16] to replace the nonlinear physical models used in the one-dimensional arterial network

The achievement of these additional objectives would allow the model to be more physically accurate and less costly to compute. These improvements would allow rapid application to a broad variety of clinical contexts, making it possible to assist medical practicioners in performing diagnoses and planning treatments.

6.2 Publications and Presentations

The publications and presentations associated with this work are listed below.

1. Canuto, D., Chong, K., Bowles, C., Dutson, E. P., Eldredge, J. D., and Benharash, P., "A regulated multiscale closed-loop cardiovascular model, with applications to hemorrhage and hypertension, *International Journal of Biomedical Engineering*, 2018

2. Canuto, D., Pantoja, J. L., Han, J., Dutson, E. P., and Eldredge, J. D., An ensemble Kalman filter approach to parameter optimization for patient-specific cardiovascular modeling, 2019, in prep.

3. Canuto, D., Chang, Y., Eldredge, J., Dutson, E. P., and Benharash, P., A Parameter Ensemble Kalman Filter for Patient-Specific Cardiovascular Modeling, *71st Annual Meeting of the APS Division of Fluid Dynamics*, Atlanta, GA, November 25-27, 2018. Presentation.

4. Canuto, D., Chong, K., Bowles, C., Dutson, E. P., Eldredge, J. D., and Benharash, P., A Multiscale Closed-Loop Cardiovascular Model, with Applications to Hemorrhage and

Hypertension, *70th Annual Meeting of the APS Division of Fluid Dynamics*, Denver, CO, November 19-21, 2017. Presentation.

[AA99] J. L. Anderson and S. L. Anderson. "A Monte Carlo implementation of the nonlinear filtering problem to produce ensemble assimilations and forecasts." *Mon. Wea. Rev.*, **127**:2741–2758, 1999.

[AHM76] F. M. Abboud, D. D. Heistad, A. L. Mark, and P. G. Schmid. "Reflex control of the peripheral circulation." *Prog. Cardio. Diseases*, **18**(5):371–403, 1976.

[AIH14] J. Aguero, K. Ishikawa, L. Hadri, C. Santos-Gallego, K. Fish, N. Hammoudi, A. Chaanine, S. Torquato, C. Naim, B. Ibanez, D. Pereda, A. Garcia-Alvarez, V. Fuster, P. P. Sengupta, J. A. Leopold, and R. J. Hajjar. "Characterization of right ventricular remodeling and failure in a chronic pulmonary hypertension model." *Am. J. Physiol. Heart Circ. Physiol.*, **307**(8):H1204–H1215, 2014.

[Ala06] J. Alastruey. *Numerical modelling of pulse wave propagation in the cardiovascular system: development, validation, and clinical applications.* PhD thesis, Imperial College London, 2006.

[APP08] J. Alastruey, K. H. Parker, J. Peiró, and S. J. Sherwin. "Lumped parameter outflow models for 1-D blood flow simulations: effect on pulse waves and parameter estimation." *Commun. Comp. Phys.*, **4**(2):317–336, 2008.

[AT84] F. M. Abboud and M. D. Thames. *Handbook of Physiology: Peripheral Circulation and Organ Blood Flow*, volume 3, chapter 19, pp. 675–753. Americal Physiological Society, 1984.

[Avo80] A. P. Avolio. "Multi-branched model of the human arterial system." *Med. Biol. Eng. Comp.*, **18**:709–718, 1980.

[BAP01] P. Boscan, A. M. Allen, and J. F. R. Paton. "Baroreflex inhibition of cardiac sympathetic outflow is attenuated by angiotensin II in the nucleus of the solitary tract." *Neuroscience*, **103**(1):153–160, 2001.

[BGC84] S. M. Barman, G. L. Gebber, and F. R. Calaresu. "Differential control of sympathetic nerve discharge by the brain stem." *Am. J. Physiol.*, **247**, 1984.

[BHP69] J. D. Bristow, A. J. Honour, G. W. Pickering, P. Sleight, and H. S. Smyth. "Diminished baroreflex sensitivity in high blood pressure." *Circulation*, **39**:48–54, 1969.

[BKS07] J. J. Batzel, F. Kappel, D. Schneditz, and H. T. Tran. *Cardiovascular and Respiratory Systems: Modeling, Analysis, and Control.* SIAM, 2007.

[BLE98] G. Burgers, P. Jan van Leeuwen, and G. Evensen. "Analysis scheme in the ensemble Kalman filter." *Mon. Wea. Rev.*, **126**:1719–1724, 1998.

[BR80] R. L. Bras and P. Restrepo-Posada. "Real time automatic parameter calibration in conceptual runoff forecasting models." In *Proceedings of the Third International Symposium on Stochastic Hydraulics*, pp. 61–70, 1980.

[BTD05] M. Banaji, A. Tachtsidis, D. Delpy, and S. Baigent. "A physiological model of cerebral blood flow control." *Mathematical Biosciences*, **194**:125–173, 2005.

[BTF12] P. J. Blanco, P. R. Trenhago, L. G. Fernandes, and R. A. Feijóo. "On the integration of the baroreflex control mechanism in a heterogeneous model of the cardiovascular system." *Int. J. Num. Meth. Biomed. Eng.*, **28**:412–433, 2012.

[CAA00] H. L. Collins, R. A. Augustyniak, E. J. Ansorge, and D. S. O'Leary. "Carotid baroreflex pressor responses at rest and during exercise: cardiac output vs. regional vasoconstriction." *Am. J. Physiol.*, **280**, 2000.

[CAH09] P. A. Cain, R. Ahl, E. Hedstrom, M. Ugander, A. Allansdotter-Johnsson, P. Friberg, and H. Arheden. "Age and gender specific normal values of left ventricular mass, volume and function for gradient echo magnetic resonance imaging: a cross sectional study." *BMC Med. Imag.*, **9**(2), 2009.

[CBB03] A. V. Chobanian, G. L. Bakris, H. R. Black, W. C. Cushman, L. A. Green, J. L. Izzo Jr., D. W. Jones, B. J. Materson, S. Oparil, J. T. Wright Jr., E. J. Roccella, and the National High Blood Pressure Education Program Coordinating Committee. "Seventh report of the joint national committee on prevention, detection, evaluation, and treatment of high blood pressure." *Hypertension*, **42**:1206–1252, 2003.

[CST87] J. Christie, L. M. Sheldahl, F. E. Tristani, K. B. Sagar, M. J. Ptacin, and S. Wann. "Determination of stroke volume and cardiac output during exercise: comparison of two-dimensional and Doppler echocardiography, Fick oximetry, and thermodilution." *Circulation*, **76**(3):539–547, 1987.

[Dam94] R. A. L. Dampney. "Functional organization of central pathways regulating the cardiovascular system." *Physio. Rev.*, **74**(2):323–364, 1994.

[Dan98] M. Danielsen. *Modeling of feedback mechanisms which control the heart function in view to an implementation in cardiovascular models.* PhD thesis, Roskilde University, 1998.

[DBN16] T. Duriez, S. L. Brunton, and B. R. Noack. *Machine Learning Control - Taming Nonlinear Dynamics and Turbulence.* Springer, 2016.

[DM08] T. David and S. Moore. "Modeling perfusion in the cerebral vasculature." *Med. Eng. Phys.*, **30**:1227–1245, 2008.

[DMG87] A. Dabestani, G. Mahan, J M. Gardin, K. Takenaka, C. Burn, A. Allfie, and W. L. Henry. "Evaluation of pulmonary artery pressure and resistance by pulsed Doppler echocardiography." *Am. J. Cardio.*, **59**:662–668, 1987.

[DNP03] A. Di Carlo, P. Nardinocchi, G. Pontrelli, and L. Teresi. "A heterogeneous approach for modelling blood flow in an arterial segment." *Trans. Biomed. Health*, **6**:69–78, 2003.

[Eve03] G. Evensen. "The Ensemble Kalman Filter: theoretical formulation and practical implementation." *Ocean Dyn.*, **53**:343–367, 2003.

[FLT06] L. Formaggia, D. Lamponi, M. Tuveri, and A. Veneziani. "Numerical modeling of 1D arterial networks coupled with a lumped parameters description of the heart." *Comp. Meth. Biomech. and Biomed. Eng.*, **9**(5):273–288, 2006.

[Fra99] O. Frank. "Die grundform des arterielen pulses erste abhandlung: mathematische analyse." *Z. Biol.*, **37**:483–526, 1899.

[FRH11] R. Frithiof, R. Ramchandra, S. G. Hood, and C. N. May. "Hypertonic sodium resuscitation after hemorrhage improves hemodynamic function by stimulating cardiac, but not renal, sympathetic nerve activity." *Am. J. Physiol.*, **300**, 2011.

[FTD69] E. D. Frohlich, R. C. Tarazi, and H. P. Dustan. "Re-examination of the hemodynamics of hypertension." *Am. J. Med. Sci.*, **257**:9–23, 1969.

[Gan75] W. Ganong. *Review of Medical Physiology.* LANGE Medical Publications, Los Altos, California, 7th edition, 1975.

[GJP95] P. J. Gatti, T. A. Johnson, P. Phan, I. King Jordan III, W. Coleman, and V. John Massari. "The physiological and anatomical demonstration of functionally selective parasympathetic ganglia located in discrete fat pads on the feline myocardium." *J. Auto. Nerv. Sys.*, **51**:255–259, 1995.

[Goh07] J. R. Gohean. *"A closed-loop multi-scale model of the cardiovascular system for evaluation of ventricule assist devices."*. Master's thesis, The University of Texas at Austin, 2007.

[Gre86] H. D. Greene. "Changes in canine cardiac function and venous return curves by the carotid sinus baroreflex." *Am. J. Physio.*, **251**:288–296, 1986.

[GTA82] G. B. Guo, M. D. Thames, and F. M. Abboud. "Differential baroreflex control of heart rate and vascular resistance in rabbits." *Circ. Res.*, **50**:554–565, 1982.

[Guy91] A. C. Guyton. *Textbook of Medical Physiology.* W.B. Saunders Company, 8th edition, 1991.

[HES70] L. Hermansen, B. Ekblom, and B. Saltin. "Cardiac output during submaximal and maximal treadmill and bicycle exercise." *J. Appl. Physio.*, **29**(1):82–86, 1970.

[JM92] W. Jänig and E. M. McLachlan. "Specialized functional pathways are the building blocks of the autonomic nervous system." *J. Auto. Nerv. Sys.*, **41**:3–14, 1992.

[JUD95] S. J. Julier, J. K. Uhlmann, and H. F. Durrant-Whyte. "A new approach for filtering nonlinear systems." In *Proceedings of the 1995 American Control Conference*, 1995.

[Kal60] R. E. Kalman. "A new approach to linear filtering and prediction problems." *Trans. ASME-J. Basic Eng.*, **82**:35–45, 1960.

[KCG08] M. E. Klingensmith, L. E. Chen, S. C. Glasgow, T. A. Goers, and S. J. Melby, editors. *The Washington Manual of Surgery.* Wolters Kluwer/Lippincott Williams & Wilkins, 5th edition, 2008.

[Ker17] D. R. Kerner. "Solving windkessel models with MLAB." Civilized Software, Inc., 2017.

[KKJ07] T. Koivistoinen, T. Kööbi, A. Jula, N. Hutri-Kähönen, O. T. Raitakari, S. Majahalme, K. Kukkonen-Harjula, T. Lehtimäki, A. Reunanen, J. Viikari, V. Turjanmaa, T. Nieminen, and M. Kähönen. "Pulse wave velocity reference values in healthy adults aged 26-75 years." *Clin. Physiol. Funct. Imaging*, **27**(3):191–196, 2007.

[Kor78] D. J. Korteweg. "Uber die fortpflanzungesgechwindigkeit des schalles in elastischen röhern." *Ann. Phys. Chem.*, **5**:525–527, 1878.

[Kor71] P. Korner. "Integrative neural cardiovascular control." *Physio. Rev.*, **51**:312–355, 1971.

[KSS70] M. Kumada, R. M. Schmidt, K. Sagawa, and K. S. Tan. "Carotid sinus reflex in response to hemorrhage." *Am. J. Physiol.*, **219**(5):1373–1379, 1970.

[Ku97] D. N. Ku. "Blood flow in arteries." *Annu. Rev. Fluid Mech.*, **29**:399–434, 1997.

[KVF09] H. J. Kim, I. E. Vignon-Clementel, C. A. Figueroa, J. F. LaDisa, K. E. Jansen, J. A. Feinstein, and C. A. Taylor. "On coupling a lumped parameter heart model and a three-dimensional finite element aorta model." *Annal. Biomed. Eng.*, **37**(11):2153–2169, 2009.

[LBB11] J. S. Leiva, P. J. Blanco, and G. C. Buscaglia. "Partitioned analysis for dimensionally-heterogenous hydraulic networks." *Multiscale Model. Simul.*, **9**(2):872–903, 2011.

[LCG03] K. Lu, J. W. Clark, Jr., F. H. Ghorbel, C. S. Robertson, D. L. Ware, J. B. Zwischenberger, and A. Bidani. "Cerebral autoregulation and gas exchange studied using a human cardiopulmonary model." *Am. J. Physiol. Heart Circ. Physiol.*, **286**:H584–H601, 2003.

[LE04] M. J. Loe and W. D. Edwards. "A light-hearted look at a lion-hearted organ (or, a perspective from three standard deviations beyond the norm) Part 1 (of two parts)." *Cardiovascular Pathology*, **13**:282–292, 2004.

[Liu00] F. Liu. *Bayesian time series: analysis methods using simulation based computations*. PhD thesis, Institutes of Statistics and Decision Sciences, Duke University, 2000.

[LTH09a] F. Liang, S. Takagi, R. Himeno, and H. Liu. "Multi-scale modeling of the human cardiovascular system with applications to aortic valvular and arterial stenoses." *Med. Biol. Eng. Comp.*, **47**:743–755, 2009.

[LTH09b] F. Y. Liang, S. Takagi, R. Himeno, and H. Liu. "Biomechanical characterization of ventricular-arterial coupling during aging: a multi-scale model study." *J. Biomech.*, **42**:692–704, 2009.

[Man03] S. J. Mann. "Neurogenic essential hypertension revisited: the case for increased clinical and research attention." *Am. J. Hypertension*, 2003.

[MDP12] J. P. Mynard, M. R. Davidson, D. J. Penny, and J. J. Smolich. "A simple, versatile valve model for use in lumped parameter and one-dimensional cardiovascular models." *Int. J. Numer. Meth. Biomed. Engng.*, **28**:626–641, 2012.

[MDR82] J. Melbin, D. K. Detweiler, R. A. Riffle, and A. Noordergraaf. "Coherence of cardiac output with rate changes." *Am. J. Physiol.*, **243**, 1982.

[MFH10] C. N. May, R. Frithiof, S. G. Hood, R. M. McAllen, M. J. McKinley, and R. Ramchandra. "Specific control of sympathetic nerve activity to the mammalian heart and kidney." *Exp. Physiol.*, **95**(1):34–40, 2010.

[MH00] H. L. Mitchell and P. L. Houtekamer. "An adaptive ensemble Kalman filter." *Mon. Wea. Rev.*, **128**:416–433, 2000.

[MH03] J. Mayet and A. Hughes. "Cardiac and vascular pathophysiology in hypertension." *Heart*, **89**:1104–1109, 2003.

[MKF79] E. T. MacKenzie, J. Keith Farrar, W. Fitch, D. I. Graham, P. C. Gregory, and A. Murray Harper. "Effects of hemorrhagic hypotension on the cerebral circulation. I. Cerebral blood flow and pial arteriolar caliber." *Stroke*, **10**(6):711–718, 1979.

[Moe77] A. I. Moens. "Over de voortplantingssnelheid von den pols (On the speed of propagation of the pulse)." Technical report, Leiden University, 1877.

[Mor01] S. F. Morrison. "Differential control of sympathetic outflow." *Am. J. Physiol.*, **281**, 2001.

[MPK06] A. Maceira, S. K. Prasad, M. Khan, and D. J. Pennell. "Reference right ventricular systolic and diastolic function normalized to age, gender and body surface area from steady-state free precession cardiovascular magnetic resonance." *Eur. Heart J.*, **27**:2879–2888, 2006.

[MSG05] H. Moradkhani, S. Sorooshian, H. V. Gupta, and P. R. Houser. "Dual state-parameter estimation of hydrological models using ensemble Kalman filter." *Adv. Wat. Res.*, 2005.

[MT14] L. Müller and E. Toro. "A global multiscale mathematical model for the human circulation with emphasis on the venous system." *Int. J. Num. Meth. Biomed. Eng.*, **30**:681–725, 2014.

[MVF13] M. E. Moghadam, I. E. Vignon-Clementel, R. Figliola, and A. L. Marsden. "A modular numerical method for implicit 0D/3D coupling in cardiovascular finite element simulations." *J. Comp. Phys.*, **244**:63–79, 2013.

[NKS17] A. Naumann, O. Kolb, and M. Semplice. "On a third order CWENO boundary treatment with application to networks of hyperbolic conservation laws." *Appl. Math. Comput.*, **325**:252–270, 2017.

[NS01] T. D. Nauser and S. W. Sittes. "Diagnosis and treatment of pulmonary hypertension." *Am. Fam. Physician*, **63**:1789–1798, 2001.

[OD03] J. T. Ottesen and M. Danielsen. "Modeling ventricule contraction with heart rate changes." *J. Theo. Biol.*, **222**:337–346, 2003.

[OOC86] I. A. D. O'Brien, P. O'Hare, and R. J. M. Corrall. "Heart rate variability in healthy subjects: effect of age and the derivation of normal ranges for tests of autonomic function." *Br. Heart J.*, **55**:348–354, 1986.

[OOT05] M. S. Olufsen, J. T. Ottesen, H. T. Tran, L. M. Ellwein, L. A. Lipsitz, and V. Novak. "Blood pressure and blood flow variation during postural change from sitting to standing: model development and validation." *J. Appl. Physiol.*, **99**:1523–1537, 2005.

[OSK96] T. Obata, F. Shishido, M. Koga, H. Ikehira, F. Kimura, and K. Yoshida. "Three-vessel study of cerebral blood flow using phase-contrast magnetic resonance imaging: effect of physical characteristics." *Mag. Res. Imag.*, **14**(10):1143–1148, 1996.

[Pie06] E. Pierce. "Diagram of the human heart." Wikimedia Commons, 2006. Published under the GNU Free Documentation License.

[QV03] A. Quarteroni and A. Veneziani. "Analysis of a geometerial multiscale model based on the coupling of ODEs and PDEs for blood flow simulations." *Multiscale Model. Simul.*, **1**(2):173–195, 2003.

[RGB84] R. J. Rodeheffer, G. Gerstenblith, L. C. Becker, J. L. Fleg, M. L. Weisfeldt, and E. G. Lakatta. "Exercise cardiac output is maintained with advancing age in healthy human subjects: cardiac dilatation and increased stroke volume compensate for a diminished heart rate." *Circulation*, **69**(2):203–213, 1984.

[RJS74] J. K. Raines, M. Y. Jaffrin, and A. H. Shapiro. "A computer simulation of arterial dynamics in the human leg." *J. Biomech.*, **7**:77–91, 1974.

[RMP09] P. Reymond, F. Merenda, F. Perren, D. Rüfenacht, and N. Stergiopulos. "Validation of a one-dimensional model of the systemic arterial tree." *Am. J. Physiol. Heart Circ.*, **297**:208–222, 2009.

[RRK08] G. Reiter, U. Reiter, G. Kovacs, B. Kainz, K. Schmidt, R. Maier, H. Olschewski, and R. Rienmueller. "Magnetic resonance-derived 3-dimensional blood flow patterns in the main pulmonary artery as a marker of pulmonary hypertension and a measure of elevated mean pulmonary arterial pressure." *Circ. Cardiovasc. Imaging*, **1**:23–30, 2008.

[RRK15] G. Reiter, U. Reiter, G. Kovacs, H. Olschewski, and M. Fuchsjäger. "Blood flow vortices along the main pulmonary artery measured with MR imaging for diagnosis of pulmonary hypertension." *Radiology*, **275**(1):71–79, 2015.

[SA72] B. Schaaf and P. Abbrecht. "Digital computer simulation of human systemic arterial pulse wave transmission: a nonlinear model." *J. Biomech.*, **5**:345–364, 1972.

[SB80] A. A. Shoukas and M. C. Brunner. "Epinephrine and the carotid sinus baroreceptor reflex." *Circ. Res.*, **37**:809–818, 1980.

[SDM01] A. W. Sheel, P. A. Derchak, B. J. Morgan, D. F. Pegelow, A. J. Jacques, and J. A. Dempsey. "Fatiguing inspiratory muscle work causes reflex reduction in resting leg blood flow in humans." *J. Physiol.*, **537**:277–289, 2001.

[SFP03] S. J. Sherwin, V. Franke, J. Peiró, and K. Parker. "One-dimensional modelling of a vascular network in space-time variables." *J. Eng. Math.*, **47**:217–250, 2003.

[SMW96] N. Stergiopulos, J. J. Meister, and N. Westerhof. "Determinants of stroke volume and systolic and diastolic pressure." *Am. J. Physiol. Heart Circ.*, **270**:H2050–H2059, 1996.

[SO88] C. W. Shu and S. Osher. "Efficient implementation of essentially non-oscillatory shock-capturing schemes." *J. Comp. Phys.*, **77**:439–471, 1988.

[SSS73] H. Suga, H. Sagawa, and A. Shoukas. "Load independence of the instantaneous pressure-volume ratio of the canine left ventricle and effects of epinephrine and heart rate on the ratio." *Circ. Res.*, **32**:314–322, 1973.

[STL69] D. L. Schultz, D. S. Tunstall-Pedoe, G. J. Lee, A. J. Gunning, and B. J. Belhouse. *CIBA Foundation Symposium - Circulatory and Respiratory Mass Transport*, chapter 11. CIBA Foundation, London, 1969.

[SYR92] N. Stergiopulos, D. F. Young, and T. R. Rogge. "Computer simulation of arterial flow with applications to arterial and aortic stenoses." *J. Biomech.*, **25**:1477–1488, 1992.

[TA90] G. Tortora and N. Anagnostakos. *Principles of Anatomy and Physiology.* Harper and Row Publishers, 6th edition, 1990.

[TAC14] Y. Tang, J. Ambandan, and D. Chen. "Nonlinear measurement function in the ensemble Kalman Filter." *Adv. Atmos. Sci.*, **31**:1–8, 2014.

[TD09] G. J. Tortora and B. Derrickson. *Principles of Anatomy and Physiology.* John Wiley & Sons, Inc., 12th edition, 2009.

[TF09] C. A. Taylor and C. A. Figueroa. "Patient-specific modeling of cardiovascular mechanics." *Annu. Rev. Biomed. Eng.*, 2009.

[TOK06] R. Torii, M. Oshima, T. Kobayashi, K. Takagi, and T. E. Tezduyar. "Computer modeling of cardiovascular fluid-structure interactions with the deforming-spatial-domain/stabilized space-time formulation." *Comput. Methods Appl. Mech. Engrg.*, **195**:1885–1895, 2006.

[UD91] M. Ursino and P. Digiammarco. "A mathematical model of the relationship between cerebral blood volume and intracranial pressure changes—the generation of plateau waves." *Annal. Biomed. Eng.*, **19**:15–42, 1991.

[vMG06] A. van Griensven, T. Meixner, S. Grunwald, T. Bishop, M. Diluzio, and R. Srinivasan. "A global sensitivity analysis tool for the parameters of mutli-variable catchment models." *J. Hydrol.*, **324**:10–23, 2006.

[VS02] S. Volianitis and N. H. Secher. "Arm blood flow and metabolism during arm and combined arm and leg exercise in humans." *J. Physiol.*, **544**:977–984, 2002.

[VT04] I. E. Vignon and C. A. Taylor. "Outflow boundary conditions for one-dimensional finite element modeling of blood flow and pressure waves in arteries." *Wave Motion*, **39**:361–374, 2004.

[WBD69] N. Westerhof, F. Bosman, C. J. De Vries, and A. Noordergraaf. "Analog studies of the human systemic arterial tree." *J. Biomech.*, **2**:121–143, 1969.

[Wes93] M. West. "Mixture models, Monte Carlo, Bayesian updating and dynamic models." *Comput. Sci. Statist.*, **24**:325–333, 1993.

[WH12] J. S. Whitaker and T. M. Hamill. "Evaluating methods to account for system errors in ensemble data assimilation." *Mon. Wea. Rev.*, **140**:3078–3089, 2012.

[WLW09] N. Westerhof, J. W. Lankhaar, and B. E. Westerhof. "The arterial Windkessel." *Med. Biol. Eng. Comput.*, **47**:131–141, 2009.

[WN97] E. A. Wan and T. A. Nelson. "Dual Kalman filtering methods for nonlinear prediction, estimation and smoothing." *Adv. Neural Info. Process Sys.*, **9**, 1997.

[Wom57] J. R. Womersley. "Oscillatory flow in arteries: the constrained elastic tube as a model of arterial flow and pulse transmission." *Phys. Med. Biol.*, **2**:178–187, 1957.

[WP04] J. J. Wang and K. H. Parker. "Wave propagation in a model of the arterial circulation." *J. Biomech.*, 2004.

[YML84] K. A. Yamada, R. M. McAllen, and A. D. Loewy. "GABA antagonists applied to the ventral surface of the medulla oblongata block the baroreceptor reflex." *Brain Res.*, **297**:175–180, 1984.

[YTT02] A. Yamashina, H. Tomiyama, K. Takeda, H. Tsuda, T. Arai, K. Hirose, Y. Koji, S. Hori, and Y. Yamamoto. "Validity, reproducibility, and clinical significance of noninvasive brachial-ankle pulse wave velocity measurement." *Hypertens. Res.*, **25**:359–364, 2002.

[ZM86] M. Zagzoule and J. Marc-Vergnes. "A global mathematical model of the cerebral circulation in man." *J. Biomech.*, **19**(12):1015–1022, 1986.